# $SnO_2$/CdS NANOCOMPOSITES: SYNTHESIS, PROPERTIES AND APPLICATIONS

**A DISSERTATION**

***Submitted in partial fulfillment of the requirements for the award of the degree***
**of**
**MASTER OF TECHNOLOGY**
**in**
**ADVANCED CHEMICAL ANALYSIS**

**by**
**ROQUAIYA KHALIQUE**


**DEPARTMENT OF CHEMISTRY**
**INDIAN INSTITUTE OF TECHNOLOGY ROORKEE**
**ROORKEE-247667 (INDIA)**
**MAY, 2019**

**INDIAN INSTITUTE OF TECHNOLOGY ROORKEE**
**ROORKEE**

# CANDIDATE'S DECLARATION

I hereby certify that the work which is being presented in the thesis entitled "**$SnO_2$/CdS NANOCOMPOSITES: SYNTHESIS, PROPERTIES AND APPLICATIONS"** in partial fulfillment of the requirements for the award of the degree of Master of Technology in Advanced Chemical Analysis and submitted in the Department of Chemistry of the Indian Institute of Technology Roorkee, Roorkee is an authentic record of my own work carried out during the period May, 2018 to May, 2019 under the supervision of Prof. P. Jeevanandam, Professor, Department of Chemistry, Indian Institute of Technology Roorkee, Roorkee.

The matter presented in this report has not been submitted by me for the award of any other degree of this or any other Institute.

(Signature and Enrollment no. of the candidate)

This is to certify that the above statement made by the candidate is correct to the best of my knowledge.

(Signature and name of the supervisor)

Dated:

# ACKNOWLEDGMENT

I would like to express my sincere gratitude to my supervisor **Prof. P. Jeevanandam** for his encouragement, support and valuable suggestions during the project work.

I would like to thank **Prof. M. R. Maurya**, former Head of Department of Chemistry and **Prof. K. R. Justin Thomas**, the current Head of the Department of Chemistry, IIT Roorkee, for providing the necessary facilities in the department. I also want to thank **Dr. Tapas Kumar Mandal**, project coordinator of M.Tech. program, and all the faculty members for their contribution during my project work.

I am highly grateful to Institute Instrumentation Center (IIC), IIT Roorkee for providing the instrument facilities for characterizing my samples.

I would like to mention my sincere thanks to the senior Ph.D. scholars, Ms. Vanita Sharma, Mr. Jatin Mahajan, Ms. Dimpal Tomar for their generous support and continuous guidance. I am also very thankful to Mr. Pankaj Rana, Ms. Reena Lather, Mr. Rahul Goyal, Ms. Kumkum Gangwar and Mrs. Monika Grewal and also my friends, Ms. Shelly Garg, Ms. Kriti and Mr. Mohit Agarwal for their immense support, love, and understanding during my project work.

At last, I would like to thank almighty God, my parents and family for their continuous support and love throughout my whole life.

# Abstract

In the present study $SnO_2$/CdS nanocomposites were synthesized using different concentrations of precursors through thermal decomposition method. The nanocomposites were synthesized by two ways: (i) using multiple precursors for CdS i.e. cadmium acetate and thiourea, and (ii) using bis(thiourea) cadmium acetate complex as a single molecular precursor for CdS. The $SnO_2$/CdS nanocomposites were then characterized by P-XRD, FT-IR spectroscopy, thermogravimetric analysis, scanning electron microscopy (SEM) coupled with energy dispersive X-ray analysis (EDXA), BET-surface area measurements, diffuse reflectance spectroscopy and transmission electron microscopic analysis (TEM). Congo red dye, a water pollutant and is hazardous to human life was successfully adsorbed by $SnO_2$/CdS nanocomposites synthesized using multiple precursors. The adsorption efficiency of the nanocomposites is better as compared to pure $SnO_2$ and CdS nanoparticles. Also, these nanocomposites were used for the photocatalytic degradation of rhodamine B and the performance of the nanocomposites synthesized using multiple precursors and single molecular precursor, was compared.

# List of Figures

# List of Tables

# CONTENTS

# 1. INTRODUCTION

## 1.1 History

In the ancient period, there were craftsmen who created some artefacts. Later on when they were studied, it proved that they show the properties of nanoparticles. Unknowingly, they created unique things which show great effects, for example- Lycurgus cup which is made of glass that contains gold and silver alloyed nanoparticles such that when light passes through it, shines like red colour but it shows green colour when the light is reflected through it. Maya blue is a pigment which has a property of corrosion resistance, made of clay having nanopores containing indigo dye and they are chemically combined with each other. Damascus steel swords are known for their strength, shatter resistance and very sharp edge. Their properties get enhanced due to the presence of nanowires and nanotubes [1].

According to Peter Paufler who did research on the Damascus sword said that "They developed materials by trial and error similar to evolution in biology. They didn't know the processes going inside the solids". Another archaeologist known as Ian Freestone who studied the Lycurgus cup agreed that, "They were highly skilled but they are not nanotechnologists. They did not know that they are working on the nanoscale" [2].

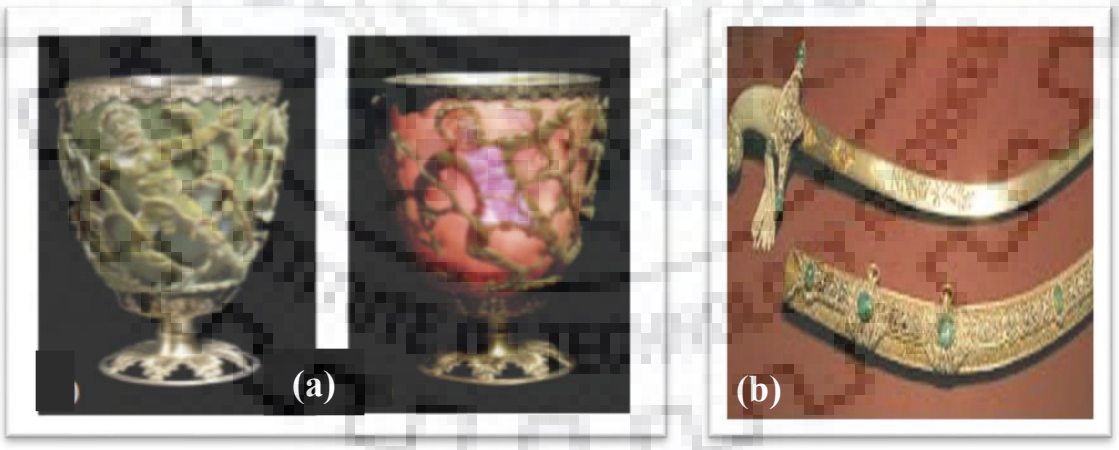


**Fig1.1: (a) Ancient Rome-Lycurgus cup [3] and (b) Damascus sword [4]**

Technically, it all started by Richard P. Feynman-the man who is responsible for introducing the concept of "Nanotechnology" through his famous lecture entitled as "*There is plenty of room at the bottom*" on 26$^{th}$ December 1959, in the annual meeting of American Physical Society at California Institute of Technology [5]. This lecture inspired many scientists across the world like in 1986 K. Eric Drexler, an American engineer, wrote a book entitled as "Engines of Creation: Coming Era of Nanotechnology" where he visualizes that the nano-scale robot assemblers will bring nano-revolution and it is going to change the whole world [6]. Later on, in 1974, the term "Nanotechnology" was proposed by a Japanese physicist Norio Taniguchi in Tokyo Science University and defined it as "*Nanotechnology mainly consists of the process of separation, consolidation, and deformation of materials by one atom or one molecule*" [7].

The invention of two instruments in the field of nanotechnology led the development to another level, i.e., Scanning Tunneling Microscope (STM) and Atomic Force Microscope (AFM) in 1981 and 1986, respectively. These instruments help in the imaging and manipulation of nanoparticles, developed in the IBM-Zurich by researchers Gerd Binnig and Heinrich Rohrer (STM) and the researchers who were responsible for the invention of AFM are Gerd Binnig, Calvin Quate and Christoph Gerber [8].

### 1.2 Nanoscience and Nanotechnology

Nanoscience is the study and analysis of materials at the nanoscale. It integrates various fields of science like physics, chemistry and biology, and it also covers various engineering fields.

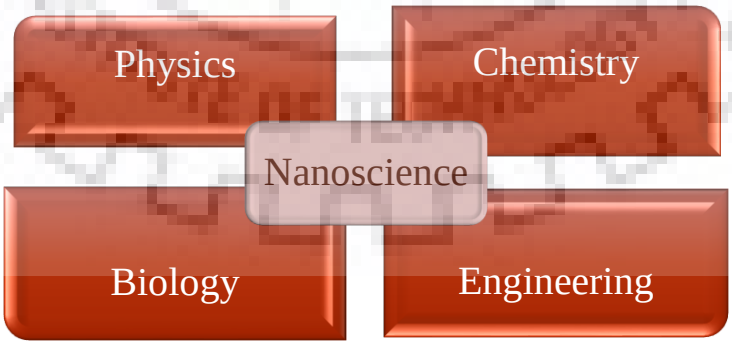


**Fig. 1.2: Integration of various fields of science and engineering to nanoscience**

Nanotechnology deals with the manipulation of particles at the nanoscale. It employs nanoscience to make new particles, materials, devices in the nano size. Nano-revolution, a term given by K. E. Drexler is about to come or almost started, and it enters in our life in the name of cosmetics, smart watches, phones, cars, etc. People have given many definitions for nanotechnology as it is still evolving, and there are more to come. In the IBM Watson Research Center, Thomas Theis - Director of Physical Sciences defined it as "Nanotechnology is an upcoming economic, business and social phenomenon. Nano advocates argue it will revolutionize the way we live, work and communicate" [9].

### 1.3 Nanoparticles

Nano is a Greek word which means "dwarf" and it means very small. Nano is one billionth of a meter. It's really hard to imagine how much it is. Nanoparticles are the particles, having one of its dimensions in the range of 1-100 nm [10].

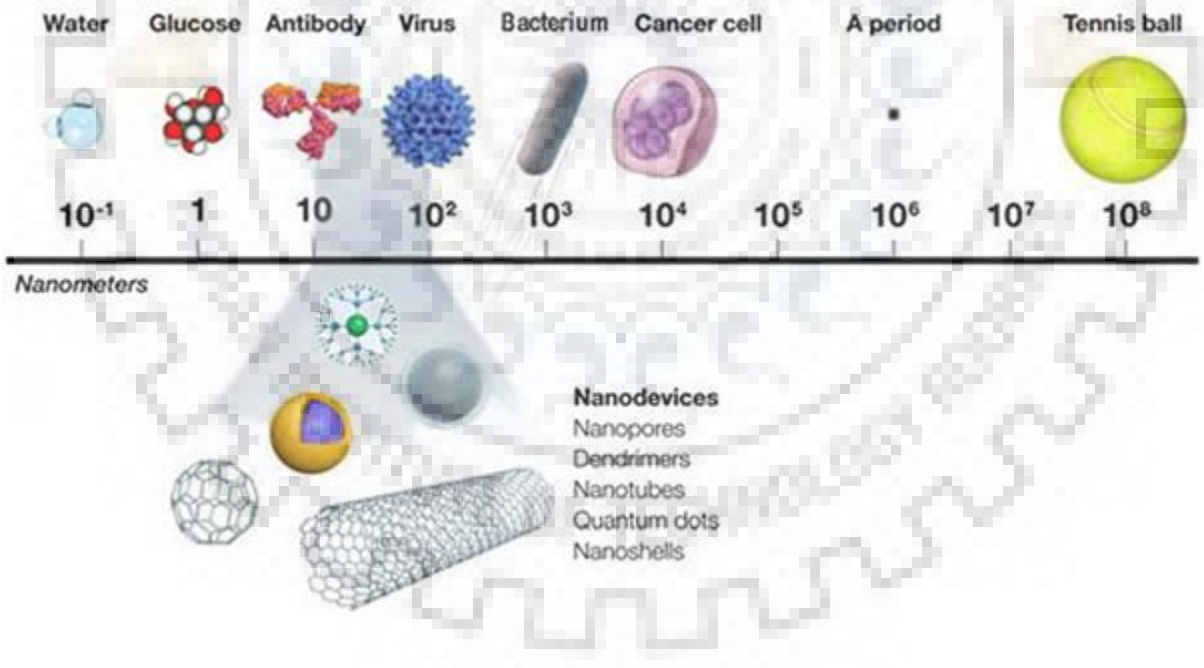


**Fig. 1.3: Comparison of the size of various things with the nanoscale [11]**

### 1.3.1 Properties of nanoparticles

On changing the size of materials or particles, they show tremendous changes in their properties.

1. Thermal Properties – Melting point decreases with decrease in the size of the material due to increase in surface to volume ratio or surface area of the particles. As melting point is a surface phenomenon, on decreasing the size, number of atoms on the surface increases and hence it causes melting point depression [12].

   For example, melting point of gold changes with change in size. It changes from 1000 $^{o}$C to 500 $^{o}$C on decresing the size up to 5 nm as shown in the Figure 1.5.

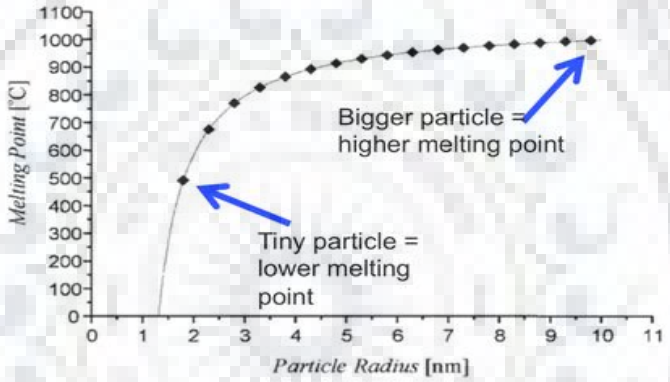


**Fig 1.4: Change in melting point of Au NPs with respect to size [13]**

2. Electrical and Optical Properties – On moving from bulk to nano range, the particles behave differently in terms of their colour and transparency. Gold in the nano size does not reflect yellow shiny colour. Even in the nano range at different sizes, they show different colours as shown in the Figure 1.6. When the size of the particle changes, the energy levels changes from continous to discrete causing the band gap to increase. The change in band gap with size is known as " Quantum Confinement Effect" [14].

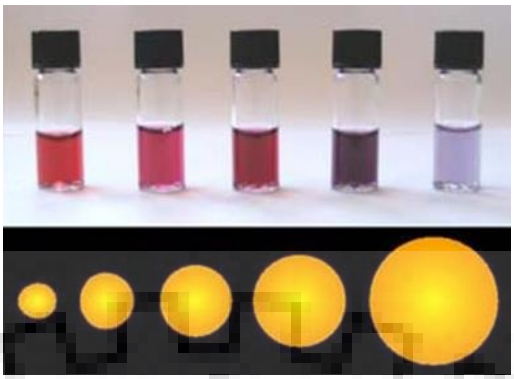

**Fig 1.5: Change in colour of Au NPs with change in particle size[15]**

3. Magnetic Properties – Materials in the nano range exhibt a unique kind of magnetism known as superparamagnetism. On decreasing the size of ferromagnetic and ferrimagnetic materials in the nano range, they show the properties of superparamagnetism. Superparamagnetic nanoparticles consist of single domain and have saturation magnetisation equal to ferromagnetic materials but on removing the magnetic field, they are completely demagnetized and their response to magnetic field is very fast [16].

4. Mechanical Properties – Mechanical properties change on decreasing the size of a particle and it allows their use in nanomanufacturing, nanofabrication and surface engineering. In order to know the exact mechanical nature of the nanoparticles, properties such as elastic modulus (decreases by 30 - 50% on decreasing the size), hardness, strength (enhanced 2 – 7 times than that of larger particles), stress and strain should be estimated [17].

### 1.3.2 Classification of nanoparticles

On the basis of their dimensions, morphology, chemical and physical properties, they are divided into various groups.

On the basis of dimensions, they are classified as- [18]

1. Zero dimension – it includes quantum dots
2. One dimension – it includes nanowires, nanotubes, nanorods
3. Two dimension – it includes nanosheets, nanowalls, nanodisks

4. Three dimension – it includes nanoballs, nanocores, nanoflowers

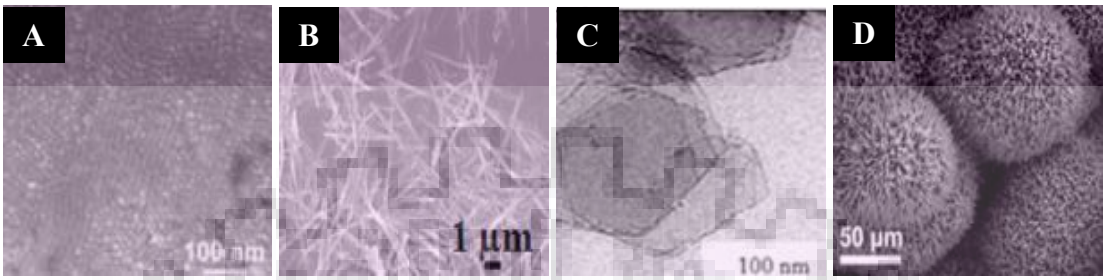


**Fig 1.6: Images of (A) Quantum dots, (B) Nanowires, (C) Nanosheets, and (D) Nanoflowers[19]**

Also, on the basis of their physical and chemical properties, they are divided as – [20]

1. Carbon based nanoparticles – Examples are carbon nanotubes and fullerenes
2. Metal based nanoparticles – Examples are Fe, Ag, Au, Co, Cd, etc.
3. Ceramic nanoparticles – Examples are zirconia, silica, alumina,etc.
4. Semiconductor nanoparticles – Examples are ZnO, $SnO_2$, CdS, etc
5. Polymeric nanoparticles
6. Lipid based nanoparticles

### 1.3.3 Synthesis of nanoparticles

Nanoparticles can be synthsized by two methods – [21]

A. Top-down method
B. Bottom-up method

In top-down method, bulk materials are broken down to form small nanoparticles and it is known as destructive method. The synthetic methods that fall under this category are mechanical milling, laser ablation, nanolithography and sputtering.

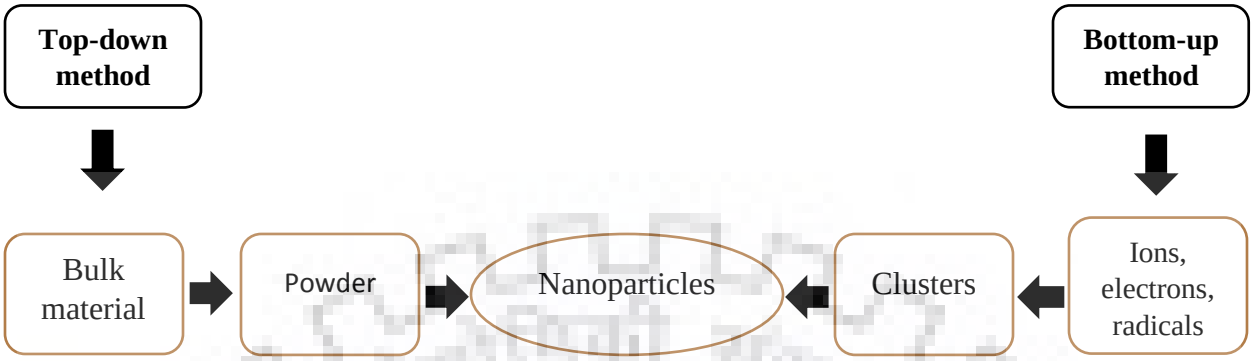


**Fig 1.7: Synthesis of nanoparticles by top-down and bottom-up method [22]**

In bottom-up method, ions, electrons and radicals are formed from the precursors and then they integrate to form nanoparticles. Synthetic methods such as sol-gel synthesis, micro-emulsion method, co-precipitation, reverse micelle method, hydrothermal method, etc. are used to form nanoparticles by bottom-up method.

### 1.4 Nanocomposites

Nanocomposites consists of multiple phases in which at least one of the phases is in nanorange, i.e., 1 – 100 nm. They are the particles of 21$^{st}$ century because of their unique properties [23].

#### 1.4.1 Types of nanocomposites

Based on the types of matrix used, nanocomposites are classified as-

1. Metal matrix nanocomposites

   They consists of a metal matrix in which the nanoparticles are introduced in order to improve their properties like strength and temperature bearing capacity [24].

   Examples of metal matrix nanocomposites are – Fe/MgO, Pb/Cu, Nb/Fe, etc.
2. Ceramic matrix nanocomposites

   Besides having properties like high thermal and chemical stability, ceramics have the problem of brittleness. In ceramic matrix nanocomposites, nanofillers are uniformly dispersed in order to enhance their fracture resistance [25].

Examples of ceramic matrix nanocomposites are – $Al_2O_3$/SiC, $Al_2O_3$/$TiO_2$, $Al_2O_3$/CNT, etc.

3. Polymer matrix nanocomposites

   Polymers have advantages of light weight, simplicity in their production and ductile nature. Along with these advantages, they have problems of low modulus and strength. In order to avoid these limitations, nanoscale reinforcements are added. It improves biodegradability of the polymers, making them ecofriendly [26].

   Examples of polymer matrix nanocomposites are – polyester/$TiO_2$, polymer/CNT, etc.

### 1.4.2 Different methods for the synthesis of nanocomposites

1. Thermal decomposition method
2. Sol-gel method
3. Co-precipitation method
4. Precipitation method
5. Solvothermal method
6. Sonochemical method
7. Microwave assisted method
8. Laser ablation method
9. Chemical vapor deposition method

**Thermal decomposition method**

It is a simple and reliable chemical process, in which a metal precursor is decomposed above its decomposition temperature in a solvent having high boiling point. Thermal decomposition method is commonly used to get highly crystalline nanoparticles. This method doesn't usually require any thermal treatment after the synthesis of the nanocomposites. Thermal decomposition approach gives a very good control over shape and particle size by varying the reaction conditions [27].

**Solvothermal method**

In this synthetic route, the reactions are carried out at high temperature and pressure inside a closed vessel known as autoclave. The autoclaves are generally operated in temperature range of 100 °C to 1000 °C and very high pressure. These extreme conditions like high temperature and pressure inside the autoclave facilitate molecular interactions between different reactants, giving highly crystalline products. The method provides reproducible results in terms of morphology and purity. In this synthetic approach, if water is used as a solvent then it is called as hydrothermal synthesis. The limitation of this method is that one cannot understand the transient changes in the material structure due to conditions like high temperature and pressure [28].

**Microwave-assisted synthesis**

It is a soft chemical method used to synthesize metal oxide nanoparticles, metal sulfide nanoparticles and their nanocomposites by irradiating the reaction mixture by microwave radiation. Microwave synthesis is gaining much attention in the last few decades because of the advantage of high reaction rate and low reaction time. In this method, solvents with high dielectric constants are used as they absorb microwave radiation very efficiently due to which they produce heat. Microwave irradiation removes the problem of heat gradient because of the dipole- dipole interaction between the solvent and the alternate electric field created by the microwave. This is one of the best methods to synthesize nanoparticles by consuming less time and energy as compared to other conventional methods [29].

### 1.4.3 Applications of nanocomposites

1. Gas sensors: Gas sensors are very important in every place in order to detect hazardous gases in order to avoid accidents. Nanocomposites are used in gas sensors because they are very sensitive, i.e. their response time is very fast. When any gas is oxidized or reduced on the nanocomposites embedded in the sensor, it reduces the flow of current and increases the resistance, and this reduction in the current or increase in the resistance act as the signal [30]. Nanocomposites such as CdS/PAAm (Polyacrylamide) are highly sensitive for the detection of LPG gas [31], Ag/α-$Fe_2O_3$ for the detection of ethanol in the air [32] and $SnO_2$/graphene oxide for the detection of ammonia [33].

2. Photocatalyst: The properties required for a photocatalyst are photo stability, chemical stability, absorption of solar radiation and effective charge separation. Nanocomposites are blessed with all these properties by the suitable combination of nanoparticles. Nanocomposites such as AgBr/g-$C_3N_4$ inactivate E.coli in the visible light [34], γ-$Fe_2O_3$/CdS degrades congo red under the visible light irradiation [35] and ZnO/CdS degrades Rhodamine-B under visible light [36].

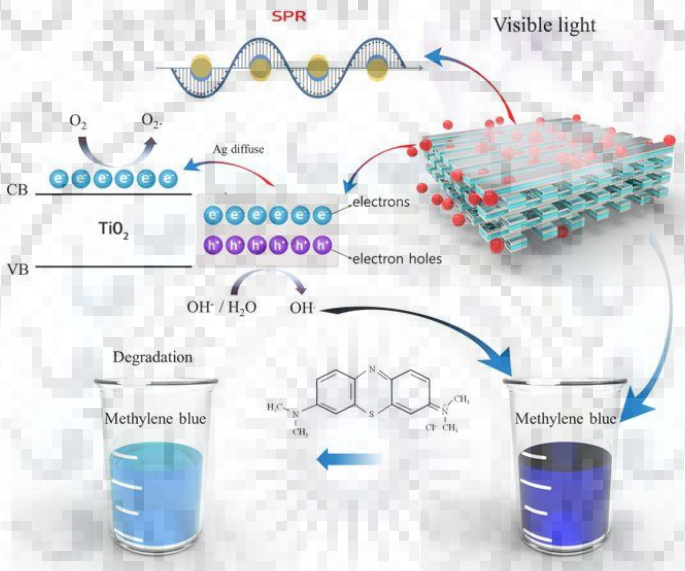


**Fig 1.8: Photodegradation of methylene blue using Ag/$TiO_2$ nanocomposites under visible light irradiataion [37]**

3. Adsorbents: Nanocomposites have high surface area and mechanical and chemical stability. These properties make them good adsorbent and can be employed for the adsorption. Sulfhydryl-lignocellulose/montmorillonite (SLT) nanocomposite adsorbs Ni(II) [38], polypyrrole/$Fe_3O_4$ is used for the adsorption of Cr(VI) [39] and polyaniline/$TiO_2$ nanocomposites adsorb congo red [40].

4. Energy storage: Nanocomposites are studied for their use in energy storage devices. In lithium ion rechargeable batteries, electrodes are made of nanocomposites like $Fe_2O_3$/$SnO_2$

[41]. Ceramic and polymeric materials can't be used for the energy storage due to high dielectric properties such as dielectric constant and breakdown field [42]. But on forming the nanocomposites of ceramics and polymers, these drawbacks are eliminated, for example, $BaTiO_3$/polyvinylidene fluoride [43].

## 2. Research gap and motivation of the work

Nanocomposites have combination of the properties of individual phases as the interaction at the interface in the nano range gets improved as compared to conventional composites. Individual properties of the materials such as their strength, reactivity, surface area, optical and electronic properties change on going from pure phase to the composite phase. They remove the flaws of the individual phases, as they become multifunctional [23].

Semiconductor nanoparticles have great applications in solar cells, gas sensors, and photocatalysis due to their unique optical, magnetic and electrical properties. Due to increase of organic pollutants in water by various chemical, textile and dye industries, the water quality is affected which ultimately affects the ecosystem. CdS NPs having narrow band gap energy of about 2.3 eV [44] is a very efficient photocatalyst in the visible region but being prone to problems of photo-corrosion and easy charge recombination, it is not good for environmental remediation [45]. $SnO_2$ having wide band gap energy of about 3.6 eV [46] enhances the photocatalytic efficiency by increasing photo activity range and leads to charge separation of the other photocatalyst by forming a heterojunction. According to literature, there have been a few reports on $SnO_2$/CdS nanocomposites –

Lei Zhang et al. [45] have prepared CdS/$SnO_2$ nanocomposites by a simple hydrothermal method which were used for the reduction of Cr(VI) and the degradation of tetracycline.

Arik Kar et al. [47] have prepared $SnO_2$/CdS heterostructure by hydrothermal method and they prove high catalytic activity for the degradation of congo red under UV light.

Shancheng Yan et al. [48] have prepared CdS/$SnO_2$ heterostructure by a facile two-step chemical solution method and they have used as gas sensors.

Ch.Venkata Reddy et al. [49] have prepared a hybrid of CdS/$SnO_2$ by a two-step co-precipitation method and the products show improved photocatalytic degradation of methyl orange.

Jingang Zhao et al. [50] have prepared $SnO_2$/CdS heterostructure by solvothermal method.

In the reported literature, $SnO_2$/CdS nanocomposites were synthesized by methods which are very complex and require large amount of time for the synthesis of the nanocomposites.

## 3. EXPERIMENTAL DETAILS

### 3.1 Synthesis of $SnO_2$ nanoparticles by sol-gel method

#### 3.1.1 Chemicals used

Tin (IV) chloride pentahydrate (Sigma-Aldrich, 98%), ethanol (99.9%, Changshu Yang Yuan Chemical) and ammonia solution (Rankem, 25%).

#### 3.1.2 Synthesis

About 1.5 g of $SnCl_4.5H_2O$ was dissolved in 100 mL of ethanol. $NH_4OH$ solution (3.5 mL) was added dropwise and the contents were kept for stirring for 5 hours under room temperature. Sol was formed which was centrifuged, washed with ethanol, and the product obtained was kept for drying at 80 ℃ overnight. The dried product was then ground and calcined at 500 ℃ for 3 hours [51].

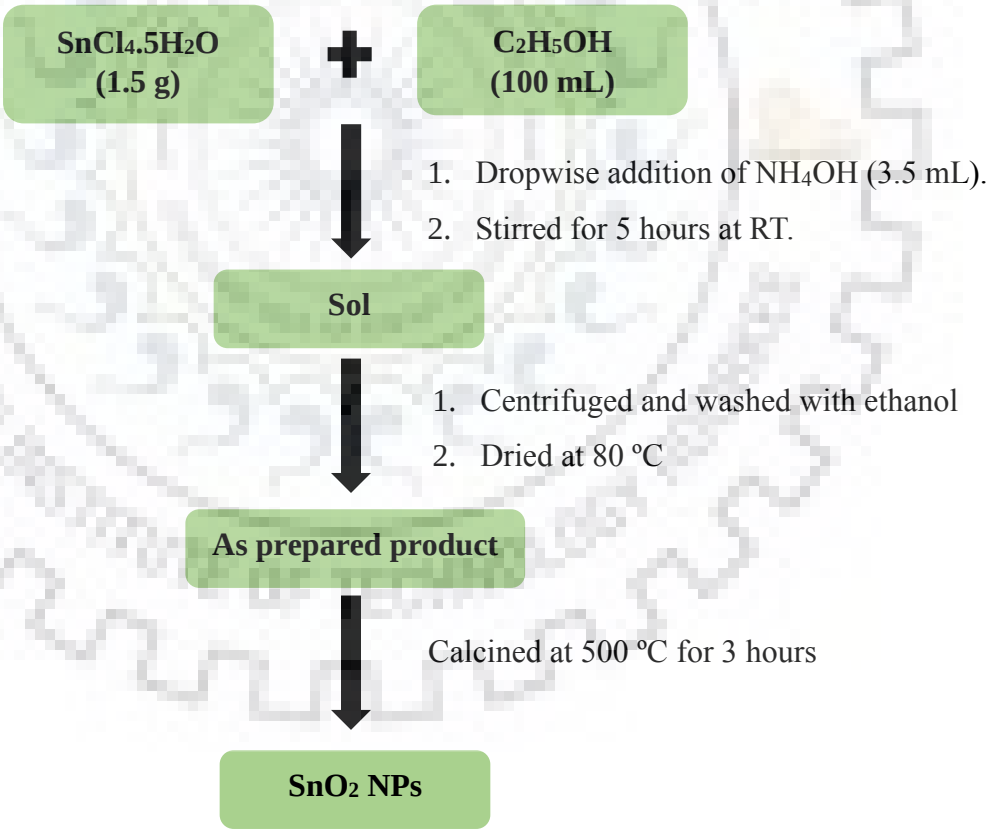


**Fig 3.1: Synthetic procedure for tin oxide nanoparticles**

### 3.2 Synthesis of $SnO_2$/CdS nanocomposites using multiple precursors

#### 3.2.1 Chemicals used

Thiourea (Rankem, 99%), cadmium acetate dihydrate (Merck, 98%), diphenyl ether (Sigma-Aldrich, 99%) and $SnO_2$ nanoparticles (calcined).

#### 3.2.2 Synthesis

The $SnO_2$/CdS nanocomposites were synthesized through thermal decomposition method using cadmium acetate and thiourea. By keeping the amount of tin oxide nanoparticles constant at 100 mg and varying the concentration of cadmium acetate and thiourea as 0.25:0.25, 0.5:0.5 and 1.0:1.0 mmol, the nanocomposites were prepared.

More details are as follows-

Tin oxide nanoparticles were dispersed in 10 mL of diphenyl ether and then equal amount of thiourea and cadmium acetate were added and refluxed at 200 ºC for 35 minutes. After 35 minutes a slurry was formed to which 25 mL of methanol was added for precipitation. The precipitate is then centrifuged and washed with methanol. The product was kept for drying in vacuum at 40 ºC overnight.

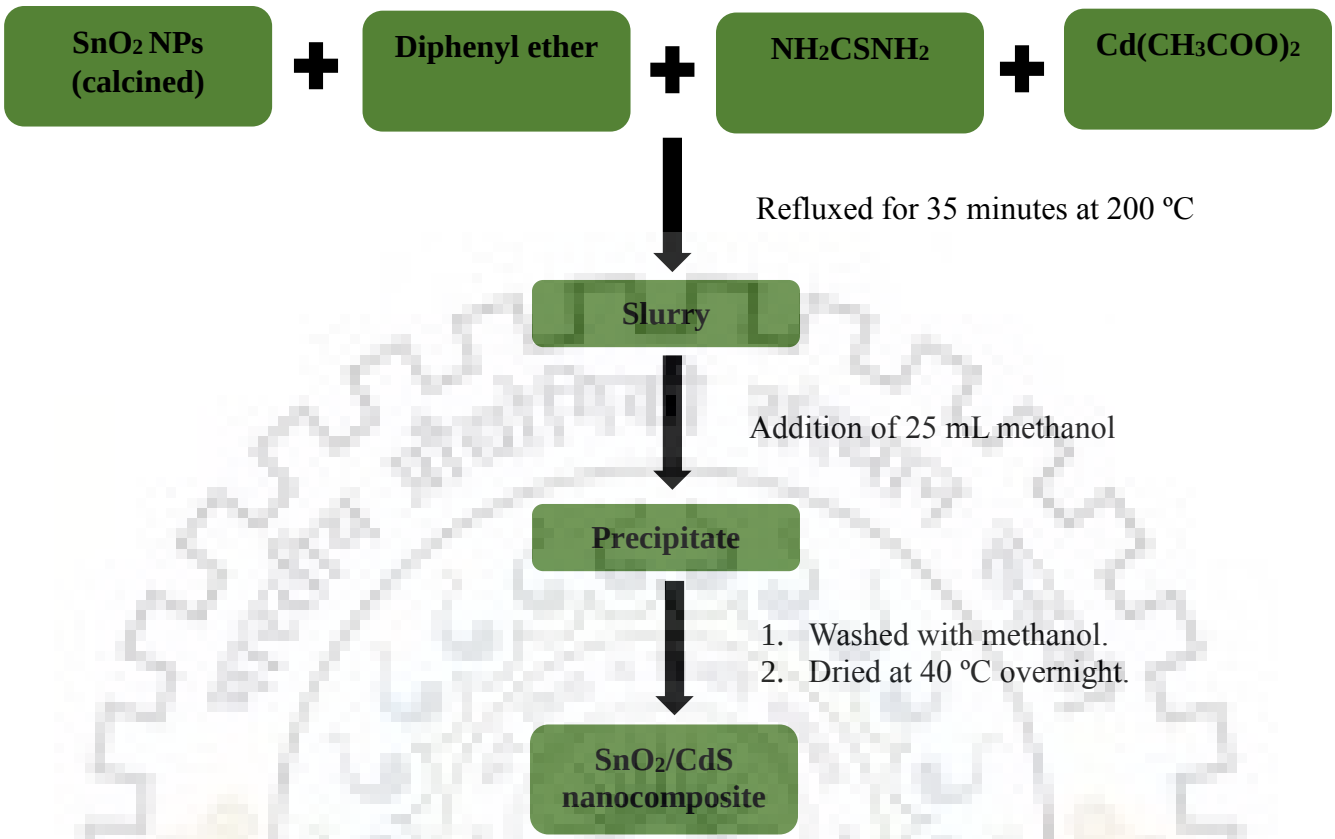


**Fig 3.2: Synthetic procedure for preparing tin oxide/cadmium sulphide nanocomposites**

**Table 3.1** Concentration of precursors and the nomenclature of the $SnO_2$/CdS nanocomposites synthesized using multiple precursors

| Sample ID | Cadmium acetate (mmol) | Thiourea (mmol) | Tin oxide nanoparticles (mg) |
|---|---|---|---|
| SC-1 | 0.25 | 0.25 | 100 |
| SC-2 | 0.50 | 0.50 | 100 |
| SC-3 | 1.00 | 1.00 | 100 |
| CdS | 1.00 | 1.00 | - |

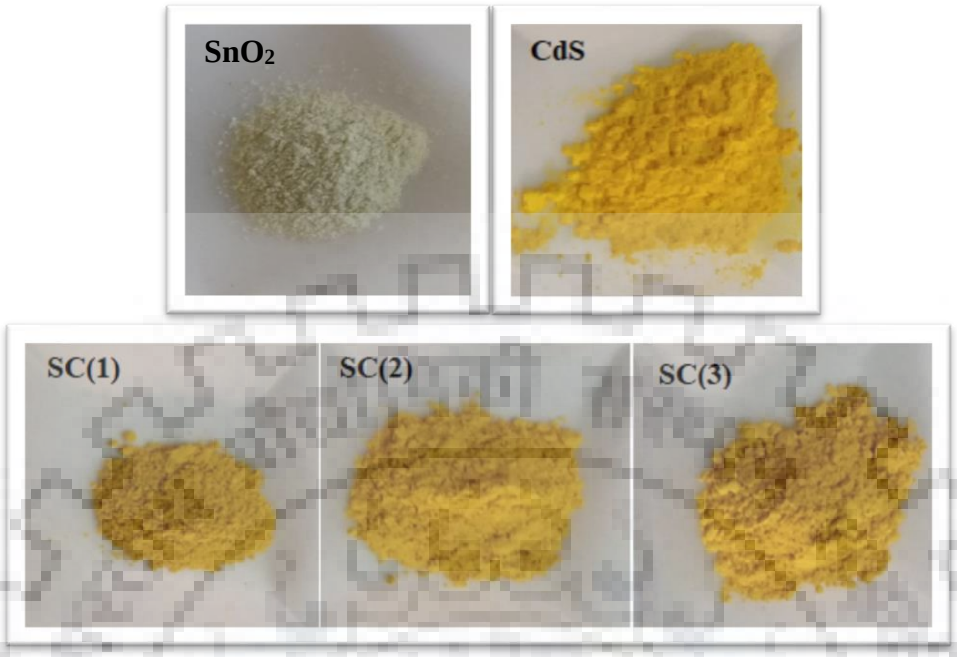


**Fig 3.3 Images of pure $SnO_2$, CdS nanoparticles and $SnO_2$/CdS nanocomposites (SC-1, SC-2 and SC-3)**

### 3.3 Synthesis of bis(thiourea) cadmium acetate complex

In order to synthesize $SnO_2$/CdS nanocomposites using a single molecular precursor, a cadmium complex (bis(thiourea) cadmium acetate) was synthesized first.

#### 3.3.1 Chemicals used

Thiourea (Rankem, 99%), cadmium acetate dihydrate (Merck, 98%) and distilled water.

#### 3.3.2 Synthesis

The complex was synthesized using cadmium acetate dihydrate and thiourea at 1:2 molar ratio in distilled water (40 mL) [52]. The reaction mixture was kept for stirring at 80 ºC for 2 hours and then the water was vaporized at 90 ºC to get a concentrated solution of about10 mL. This solution was then kept for drying in the oven at 65 ºC overnight and yellow colour crystals were obtained.

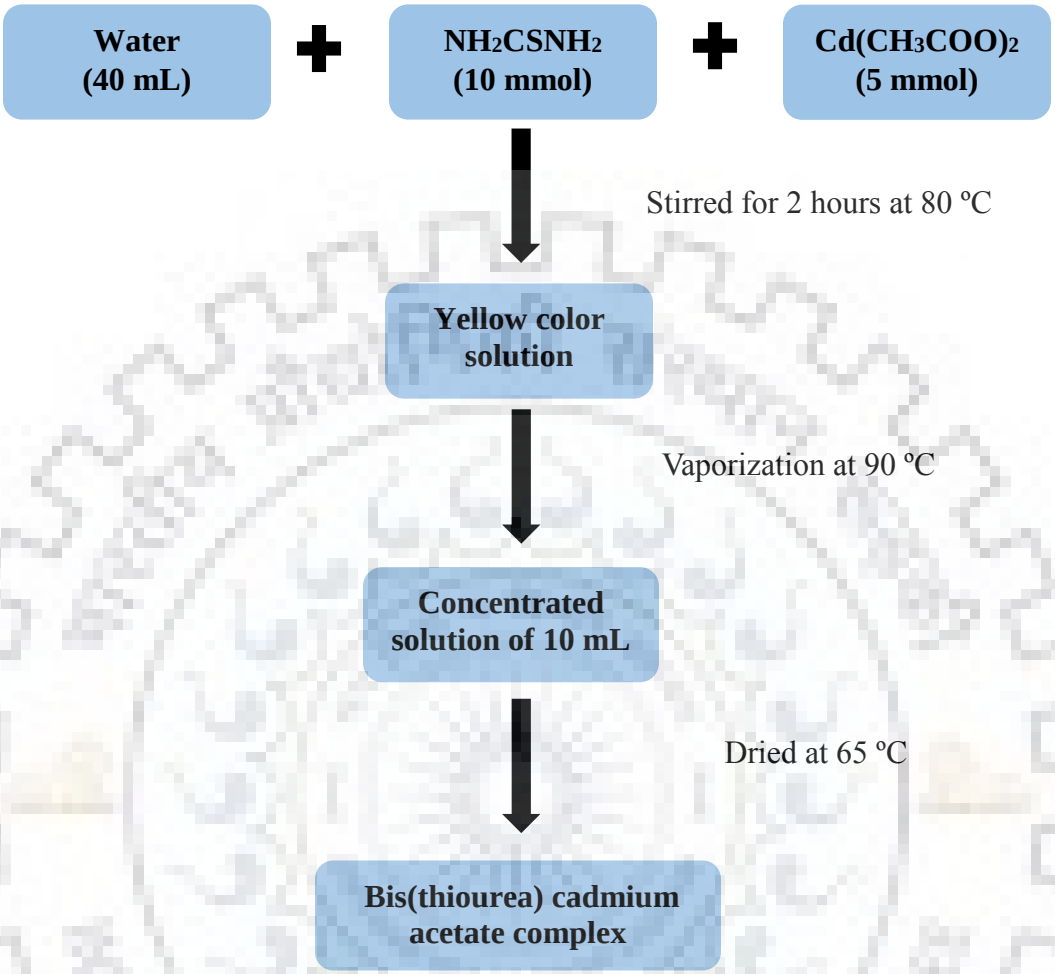


**Fig 3.4: Synthesis of Bis(thiourea) cadmium acetate complex**

## 3.4 Synthesis of $SnO_2$/CdS nanocomposites using single molecular precursor

### 3.4.1 Materials used

Calcined tin oxide nanoparticles, bis(thiourea) cadmium acetate and diphenyl ether (Sigma-Aldrich, 99%)

### 3.4.2 Synthesis of $SnO_2$/CdS nanocomposites

Three different $SnO_2$/CdS nanocomposites were prepared using different amounts of precursor complex- 0.25 mmol, 0.5 mmol and 1.0 mmol. 100 mg of $SnO_2$ was dispersed in 10 mL of diphenyl ether and then the complex was added. The reaction mixture was refluxed at 200 ºC for 35 minutes. 25 mL of methanol was added to the slurry for precipitation. The precipitate was centrifuged and washed with methanol. The product was then kept for drying in the oven at 65 ºC overnight.

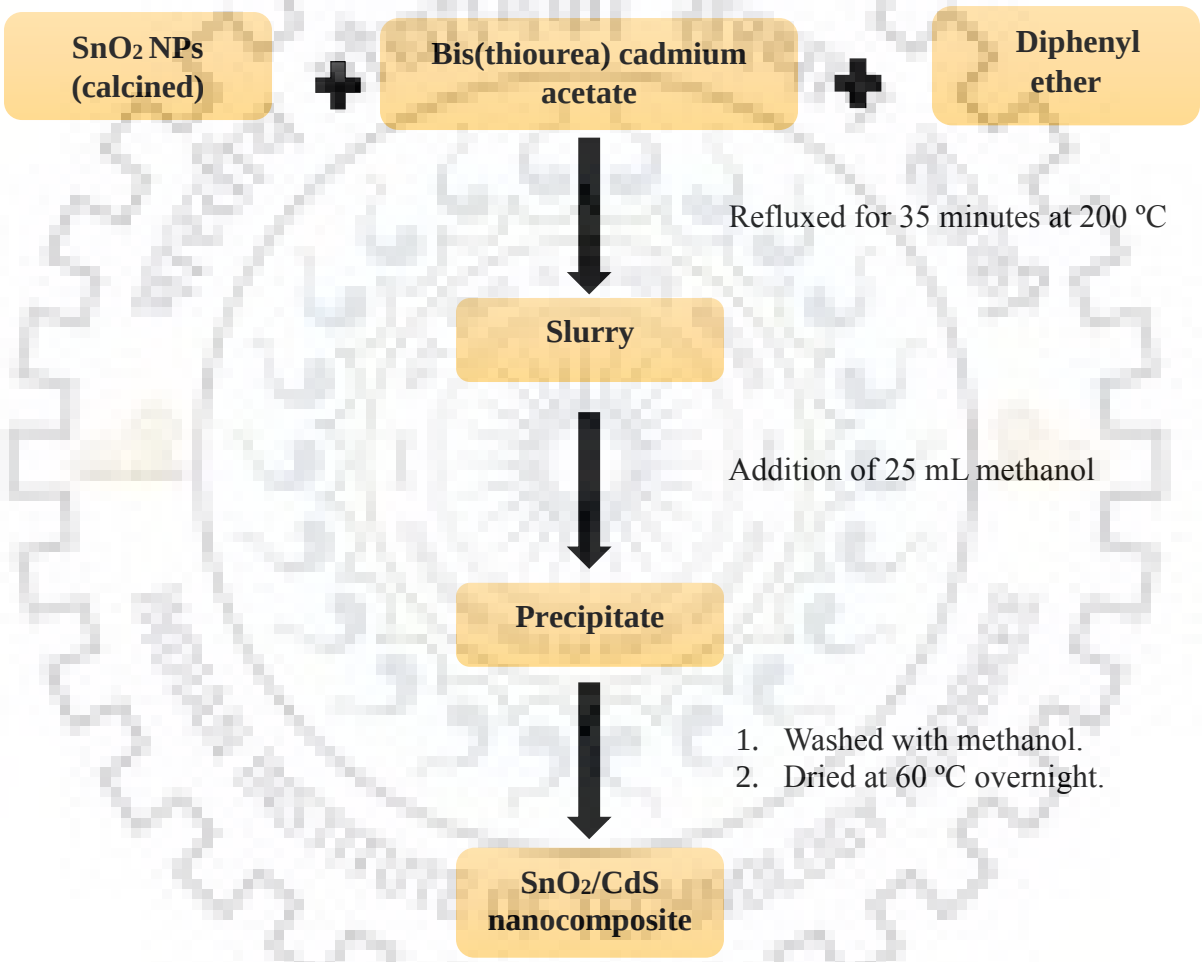


**Fig 3.5: Synthesis of $SnO_2$/CdS nanocomposites using single molecular precursor**

**Table 3.2** Concentration of precursor complex and nomenclature of the $SnO_2$/CdS nanocomposites synthesized using single precursor

| Sample ID | Bis(thiourea) cadmium acetate (mmol) | Tin oxide nanoparticles (mg) |
|---|---|---|
| SCC-1 | 0.25 | 100 |
| SCC-2 | 0.50 | 100 |
| SCC-3 | 1.00 | 100 |
| CdS | 1.00 | - |

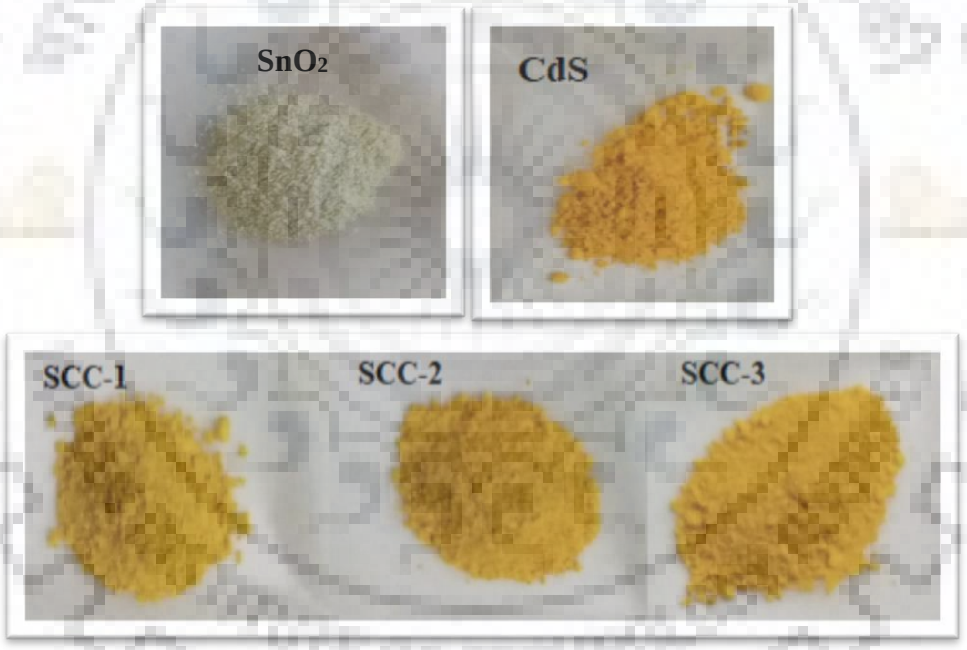


**Fig 3.6 Images of pure $SnO_2$, CdS nanoparticles and $SnO_2$/CdS nanocomposites (SCC-1, SCC-2 and SCC-3)**

## 4. Characterization tools

$SnO_2$/CdS nanocomposites, synthesized by the thermal decomposition method, were characterized by various characterization techniques. P-XRD technique was used for phase identification, TGA and DTA were done in order to check the thermal stability and purity of the samples, FT-IR spectroscopy proves various functional groups present in the samples, FE-SEM combined with EDX analysis are used to check the shape, size and composition, TEM analysis for understanding size and shape and BET-surface area measurements were done to determine surface area. Diffuse Reflectance spectroscopy (DRS) was used for the study of optical properties.

### 4.1 Powder X-ray Diffraction technique

This technique is based upon the Bragg's law where monochromatic X-rays interact with a sample to produce constructive interference and form a diffraction pattern.

$$n\lambda = 2d\sin\theta \quad (1)$$

where n is the order of diffraction, $\lambda$ is the wavelength of the X-rays, d is the interplanar spacing and $\theta$ is the angle of diffraction [53]. It is a non-destructive technique and determines the phase, crystallite size, stress and strain of the sample. Crystallite size is calculated by using Debye-Scherrer equation which is given as

$$k\lambda = B\beta\cos\theta \quad (2)$$

k is the shape factor, $\lambda$ is the X-ray wavelength, B is the crystallite size, $\beta$ is the full width at half maxima and $\theta$ is the Bragg's diffraction angle [54]. For the analysis of pure $SnO_2$, CdS nanoparticles and $SnO_2$/CdS nanocomposites, a Bruker AXS D8 diffractometer was used using Cu-K$\alpha$ radiation of wavelength 1.5406 Å and a scanning rate of 1 $^o$/minute. The identification of the phases is then obtained by matching them with the corresponding JCPDS files.

### 4.2 Thermogravimetric analysis and differential thermal analysis (TGA/DTA)

Thermogravimetric method measures change in weight with respect to temperature while differential thermal analysis measures heat flow with respect to time or temperature. Thermal stability and purity of samples were analyzed by these techniques. In the present

study, TGA/DTA analysis was done by heating the samples from 30-1000 $^{o}$C at a rate of 10 $^{o}$/ min in air, using a Perkin–Elmer Pyris Diamond instrument.

### 4.3 Fourier Transform Infrared Spectroscopy (FT-IR)

FT-IR technique is used for the determination of functional groups present in the samples. Samples were prepared in the form of pellets by mixing the samples with potassium bromide (KBr) in the ratio of 1:100. For recording the IR spectra, a Thermo Nicolet Nexus IR spectrometer was used in the range 450-4000 $cm^{-1}$.

### 4.4 FE-SEM and EDX Analyses

When an electron beam interacts with a sample, it produces three types of signals – (1) characteristic X-rays which are due to elements present in the sample, (2) secondary electrons which give the topographical details of the sample and (3) back scattered electrons which give compositional distribution of elements in the sample.

The morphology, composition and distribution of the elements in $SnO_2$, CdS nanoparticles and $SnO_2$/CdS nanocomposites were characterized by two field emission scanning electron microscopes, FEI Quanta 200F and Carl Zeiss Ultra Plus, at 20 kV coupled with an energy dispersive X-ray analysis unit.

### 4.5 TEM and SAED Analyses

Transmission Electron Microscopy is a technique which uses transmitted electrons to provide morphological and crystallographic information of samples. Selected Area Electron Diffraction pattern gives information about whether the samples are amorphous (diffuse rings) or crystalline (bright spots) or polycrystalline (presence of rings along with the bright spots).

The samples for the TEM measurements were prepared by dispersing the nano powders weighing 1-2 mg in 5 ml of ethanol. The dispersion was then placed on the Cu grid with the help of a micropipette and dried and the images were obtained by using a FEI TECNAI $G^{12}$ Transmission Electron Microscope, operated at 200 kV.

### 4.6 Brunauer-Emmett-Teller Surface area measurement

For measuring surface area of the samples, a Nova 2200e Quantachrome instrument was used. About 100 mg of sample was weighed and taken in a bulb cell, it was then degassed under vacuum conditions at 120 $^{o}$C. At 77 K, surface area was measured by the adsorption of nitrogen. The BET equation for the surface area analysis

$$\frac{1}{w\left(\left(\frac{Po}{P}\right)-1\right)} = \frac{1}{CW_m} + \frac{C-1}{CW_m}\left(\frac{P}{P_o}\right) \qquad (3)$$

Where C is the BET constant, $W_m$ is the weight of adsorbate, w is the weight of gas adsorbed and $P/P_o$ is the relative pressure. The plot of

$$\frac{1}{w\left(\left(\frac{Po}{P}\right)-1\right)} \text{ versus } \left(\frac{P}{P_o}\right)$$

follows a straight line with a slope of ($C-1/CW_m$) and intercept equals to ($1/CW_m$). The summation of intercept and slope gives the weight of monolayer adsorbate. Total surface area $S_t$ is derived by using the relation

$$S_t = \frac{W_m \times N \times Acs}{M} \qquad (4)$$

Where N is the Avogadro's number, Acs is cross-sectional area of adsorbate and M is the molecular weight of adsorbate. Finally, the specific surface area (S) is obtained by dividing the total surface area with the weight of the sample [55].

$$S = \frac{St}{W} \qquad (5)$$

### 4.7 Diffuse Reflectance Spectroscopy (DRS)

Optical studies were done with the help of Diffuse Reflectance Spectroscopy (DRS). In diffuse reflectance, relative change in the intensity of reflected light from the surface is measured. It is used for the estimation of band gap of the sample. Samples were prepared by mixing them thoroughly with $BaSO_4$ in the ratio of 1:100. Band gap was measured using Tauc plots, using the equation

$$(\alpha h\upsilon) = A\,(h\upsilon - E_g)^n \qquad (6)$$

Where, α is the absorbance, A is constant and $E_g$ is the band gap and the value of n defines the type of transition. The value of n = 2 for indirect allowed transition, n = ½ for direct allowed transition, n = 3 for forbidden indirect transitions and n = 3/2 for direct forbidden transition [56]. In this case a Shimadzu UV-2450 UV-Visible spectrometer attached with a diffuse reflectance accessory, was used for the estimation of band gap.

## 5. Results and Discussion

The $SnO_2$/CdS nanocomposites were characterized using different analytical methods, such as XRD, IR spectroscopy, TGA, SEM, TEM and UV-Visible DRS.

### 5.1 Nanocomposites synthesized using multiple precursors

#### 5.1.1 XRD Results

Fig. 5.1 shows the XRD patterns of as-prepared and calcined tin oxide nanoparticles. These patterns match with the JCPDS File No. 41-1445 and it confirms the formation of tetragonal tin oxide nanoparticles. Peaks at 2θ value of 26.5º, 33.79º, 37.9º, 51.9º, 54.7º, 57.8º and 61.8º correspond to (110), (101), (200), (211), (220), (002) and (310) planes of $SnO_2$. As prepared $SnO_2$ nanoparticles shows three broad peaks at 26.5º, 33.9º and 51.9º. On calcination at 500 ºC, the crystallinity of the tin oxide nanoparticles gets enhanced. The crystallite size (estimated using (101) reflection) of as-prepared and calcined $SnO_2$ nanoparticles are 3.8 nm and 9.9 nm respectively.

Fig. 5.2 shows the XRD patterns of cadmium sulphide nanoparticles, calcined tin oxide nanoparticles and nanocomposites synthesized using three different concentrations of cadmium acetate dihydrate and thiourea (SC-1, SC-2 and SC-3). The XRD pattern of pure CdS nanoparticles match with JCPDS File NO. 47-1179 corresponding to CdS. Nanocomposites show peaks at 26.5º, 33.79º, 37.95º, 51.9º, 54.57º, 57.96º and 61.9º which correspond to (110), (101), (200), (211), (220) (002) and (310) planes of $SnO_2$. Reflections (110) and (103) at 43.9º and 47.9º are due to the presence of CdS in the composites. With an increase in the concentration of cadmium acetate and thiourea from 0.25 to 1.0 mmol, peaks due to CdS become more prominent as the concentration of CdS in the nanocomposites increases. The crystallite size calculated using (101) plane of $SnO_2$ for SC-1, SC-2 and SC-3 are 11.6, 11.4 and 11.3 nm and the crystallite size of CdS in the nanocomposites (SC-1, SC-2 and SC-3), calculated using (110) plane of CdS, are 7.1 nm, 8.1 nm and 8.3 nm, respectively.

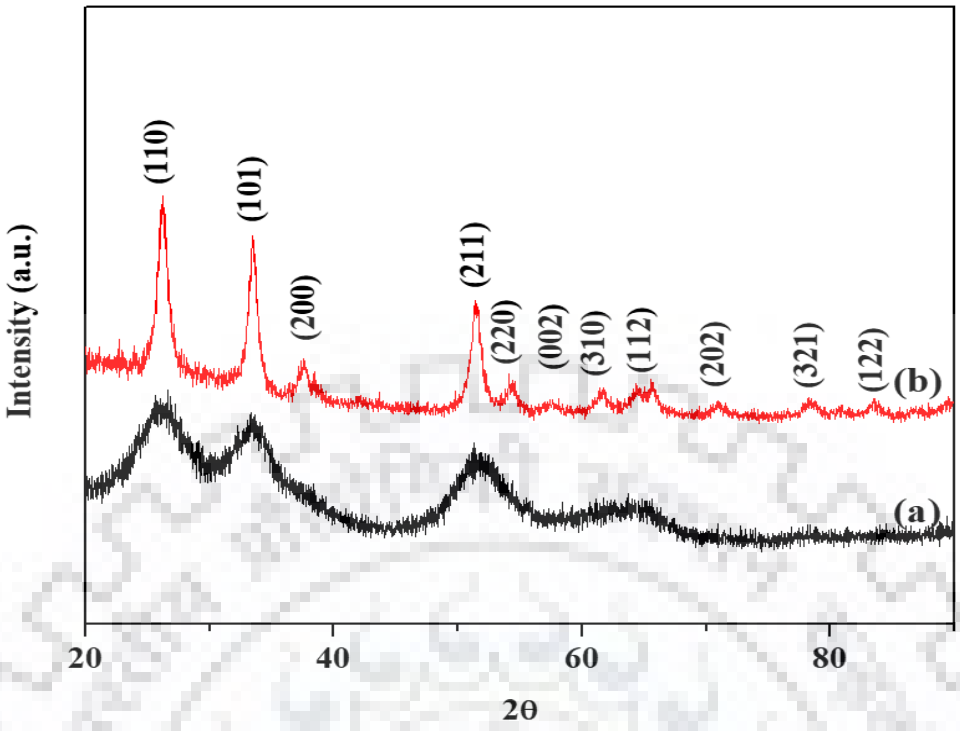


**Fig 5.1: XRD patterns of $SnO_2$ nanoparticles: (a) non-calcined (b) calcined**

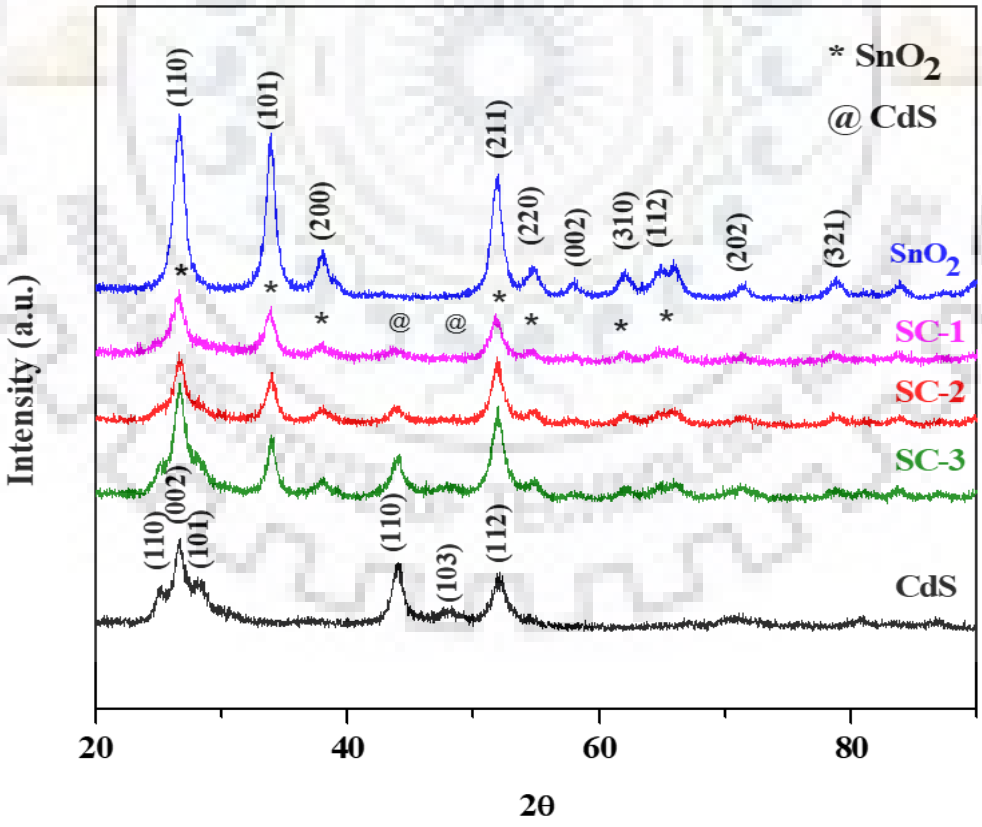


**Fig 5.2: XRD patterns of calcined $SnO_2$, pure CdS nanoparticles and $SnO_2$/CdS nanocomposites**

**Table 5.1** Crystallite size of $SnO_2$ and CdS in $SnO_2$/CdS nanocomposites

| Sample ID | Crystallite size of $SnO_2$ (nm) | Crystallite size of CdS (nm) |
|---|---|---|
| SC-1 | 11.6 | 7.1 |
| SC-2 | 11.3 | 8.1 |
| SC-3 | 11.4 | 8.3 |
| CdS | - | 7.2 |
| Calcined $SnO_2$ | 9.9 | - |
| Non-calcined $SnO_2$ | 3.5 | - |

### 5.1.2 FT- IR Spectroscopy Results

The IR spectra of calcined tin oxide, pure cadmium sulphide nanoparticles and the nanocomposites, synthesized using different concentrations of precursors, are shown in Fig. 5.3. Broad bands observed in the range of 3300 – 3400 $cm^{-1}$ and 1600 $cm^{-1}$ are assigned to the stretching and bending vibrations, respectively, of water molecule adsorbed on the surface of nanoparticles and nanocomposites. Peaks in the range of 1400 $cm^{-1}$ and 1100 $cm^{-1}$ are due to the presence of organic moieties. The characteristic bands observed in the range of 630 – 660 $cm^{-1}$ and 520 – 550 $cm^{-1}$ are due to the stretching vibrations of Sn-O [57] and Cd-S bond [58], respectively, which confirm the presence of both phases in the $SnO_2$/CdS nanocomposites.

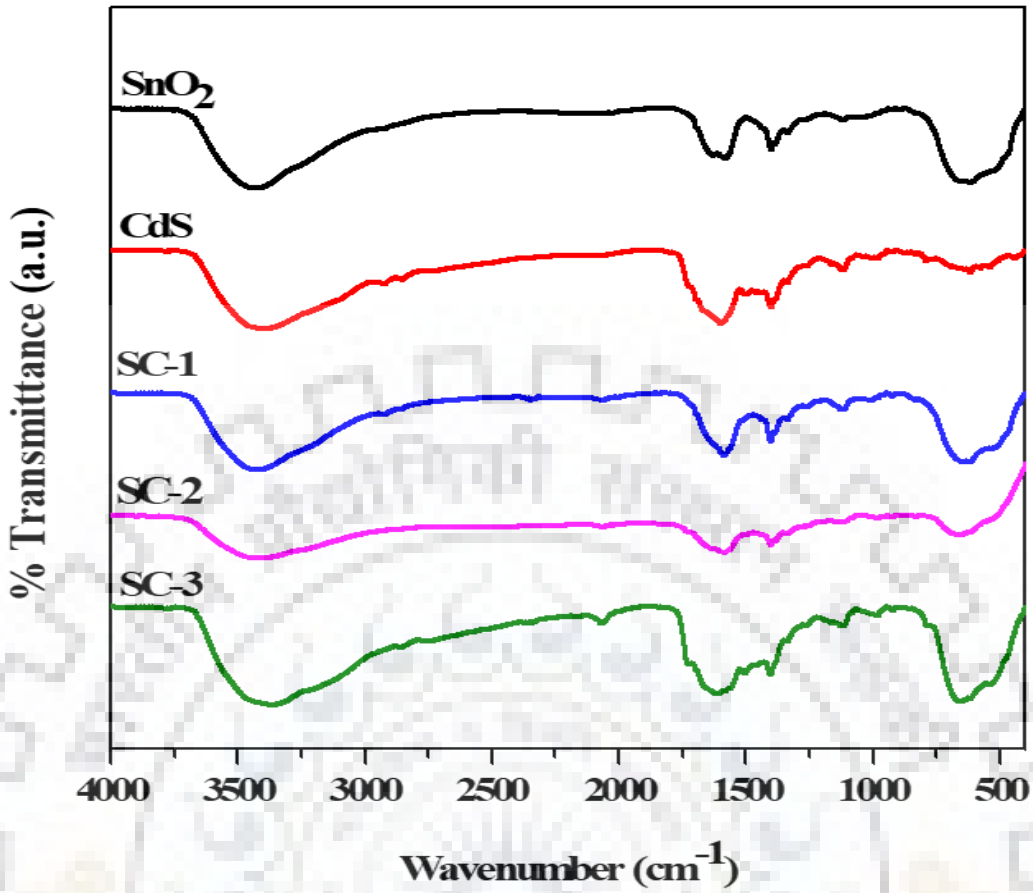


**Fig 5.3: FT–IR spectra of pure $SnO_2$, CdS nanoparticles and nanocomposites (SC-1, SC-2 and SC-3)**

**Table 5.2** IR band positions ($cm^{-1}$) and assignments for the nanocomposites

| $SnO_2$ | CdS | SC-1 | SC-2 | SC-3 | Assignment |
|---|---|---|---|---|---|
| 3430 | 3405 | 3434 | 3425 | 3378 | ν (OH) |
| 2947, 2852 | 2926, 2851 | 2926, 2859 | 2845 | 2855, 2758 | ν (C-H) |
| 1600 | 1605 | 1591 | 1593 | 1612 | δ (OH) |
| 1407 | 1409 | 1404 | 1404 | 1404 | δ (C-H) |
| - | 1113 | 1123 | 1119 | 1124 | ν (C-O) |
| 630 | - | 634 | 657 | 659 | ν (Sn-O) |
| - | 550 | 530 | 528 | 541 | ν (Cd-S) |

### 5.1.3 TGA Results

Thermogravimetric analysis patterns of non-calcined tin oxide, pure cadmium sulphide nanoparticles and the nanocomposites SC-1, SC-2 and SC-3 are shown in Figure 5.4. The TGA results are summarized in Table 5.3. Tin oxide shows a weight loss of about 2.1 % due to removal of moisture and organic moieties. As tin oxide is very stable, weight changes observed in the $SnO_2$/CdS nanocomposites are mainly due to cadmium sulphide. Up to 480 $^oC$ cadmium sulphide shows a weight loss of about 15.24 % while the nanocomposites show about 2.48 – 8.96 % due to the removal of moisture and removal of organic moieties [59]. Then, oxidation of CdS to $CdSO_4$ takes place which is witnessed by the weight gain of nanocomposites in the temperature regime of 490 – 600 $^oC$ [60]. Complete oxidation of cadmium sulphide takes place above 700 $^oC$ forming CdO [61].

DTA plots of CdS, as prepared $SnO_2$ nanoparticles and the $SnO_2$/CdS nanocomposites (SC-1, SC-2 and SC-3) are given in Figure 5.4. Two exothermic peaks are observed in the nanocomposites (SC-1, SC-2 and SC-3). The first exothermic peak is observed at 545 $^oC$, 532 $^oC$ and 550 $^oC$, in SC-1, SC-2 and SC-3 respectively. The second exothermic peak observed in the nanocomposites are in the range of 880 $^oC$ to 900 $^oC$. These peaks are due to the oxidation of CdS or formation of $CdSO_4$ and the second peak is due to the decomposition of $CdSO_4$, i.e. complete oxidation of CdS.

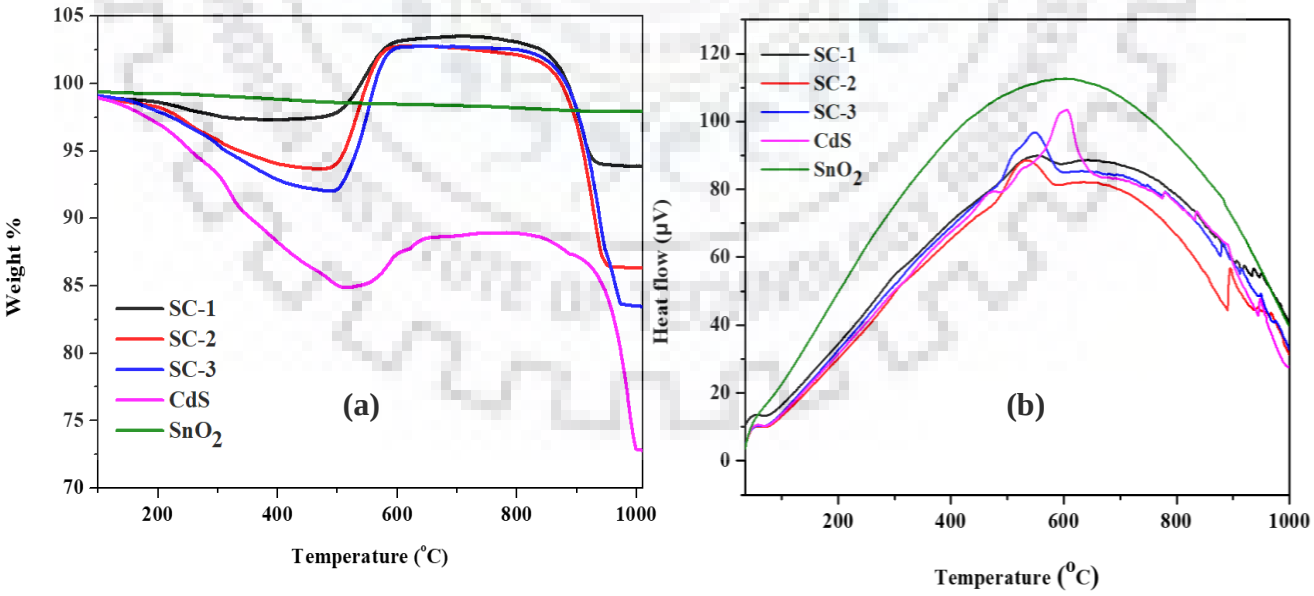


**Fig 5.4: (a) TGA and (b) DTA patterns of non-calcined $SnO_2$, pure CdS nanoparticles and $SnO_2$/CdS nanocomposites – SC-1, SC-2 and SC-3**

**Table 5.3** Thermogravimetric analysis results of $SnO_2$/CdS nanocomposites

| Sample ID | Temperature range (ºC) | DTA peak position (ºC) | % wt. loss or gain | Overall % wt. loss |
|---|---|---|---|---|
| $SnO_2$ | - | - | -2.1 | 2.1 |
| CdS | Up to 480 | 471 | -15.2 | 27.1 |
| | 550 – 650 | 600 | +4.2 | |
| | 830 –1000 | 945 | -16.0 | |
| SC-1 | Up to 365 | - | -2.5 | 5.9 |
| | 490 – 600 | 545 | +6.2 | |
| | 825 – 935 | 930 | -9.6 | |
| SC-2 | Up to 430 | - | -6.2 | 13.6 |
| | 490 – 600 | 532 | +9.1 | |
| | 825 – 950 | 895 | -16.4 | |
| SC-3 | Up to 150 | - | -9.0 | 22.5 |
| | 490 – 600 | 550 | +10.8 | |
| | 825 – 976 | 884 | -20.7 | |

### 5.1.4 FE-SEM and EDX Analysis

FE-SEM images of calcined $SnO_2$, CdS nanoparticles and $SnO_2$/CdS nanocomposites are shown in Figure 5.5. The SEM images show that the particles formed are small in size and have no specific morphology.

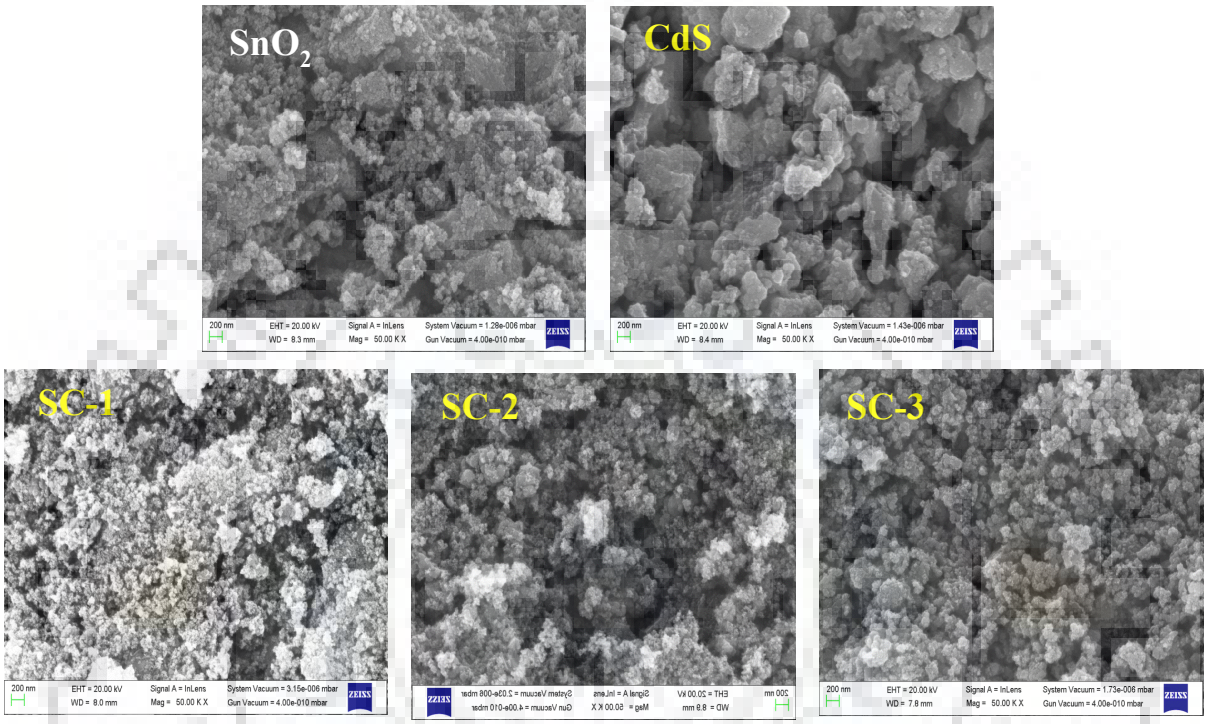


**Fig 5.5: SEM images of pure $SnO_2$, CdS nanoparticles and $SnO_2$/CdS nanocomposites**

Elemental composition analysis was done using EDXA. Pure tin oxide shows no extra peaks other than oxygen and tin. Similarly, EDX pattern of cadmium sulphide does not show any other peak besides that of cadmium and sulphur. Figure 5.6 shows the EDX patterns of the nanocomposites which suggest no other peaks besides that due to tin, oxygen, cadmium and sulphur. Also, it confirms uniform distribution of elements in the nanocomposites SC-2 and SC-3.

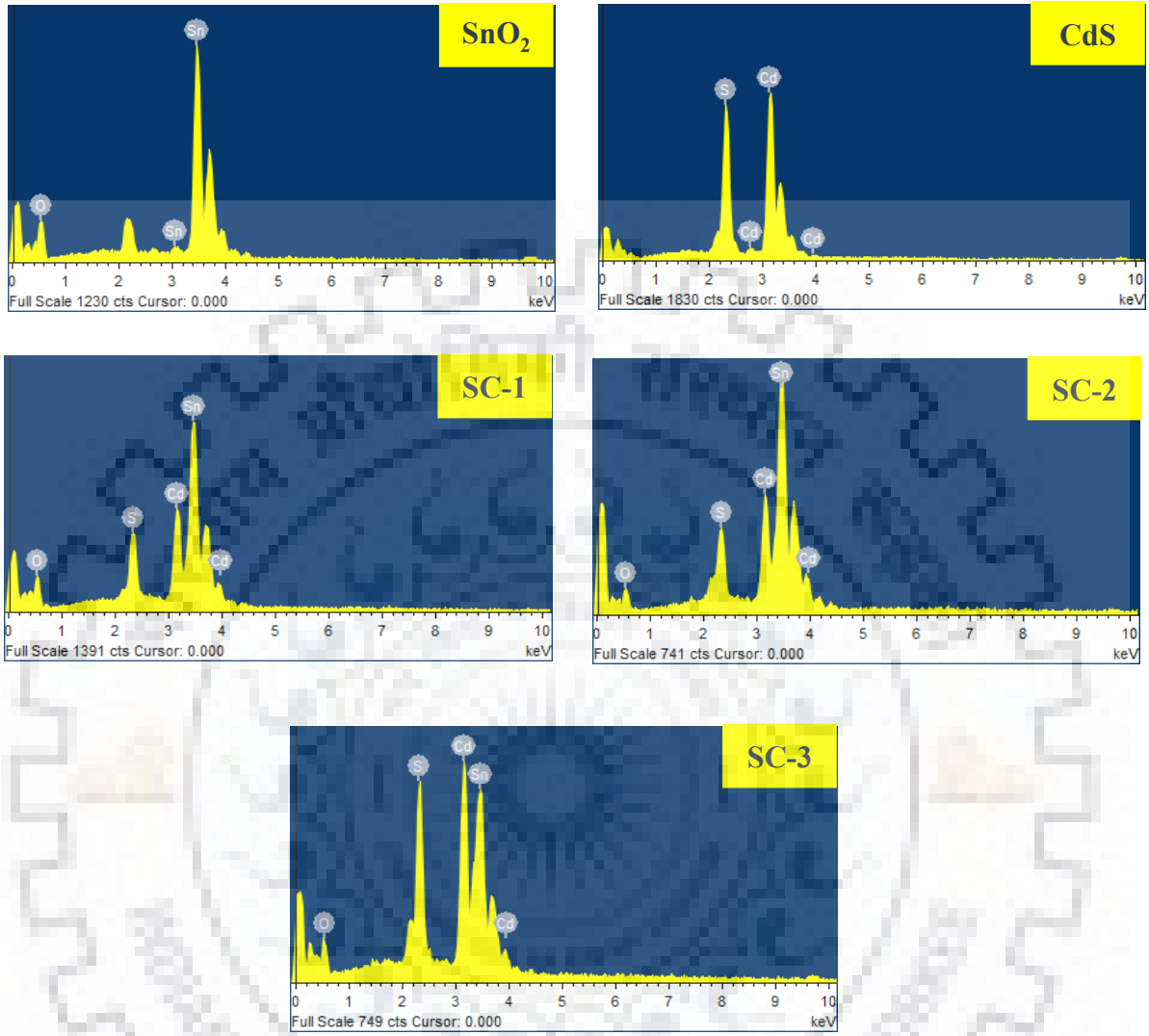


**Fig 5.6: EDX patterns of pure $SnO_2$ (calcined), CdS nanoparticles and $SnO_2$/CdS nanocomposites**

**Table 5.4** EDX analysis results of pure $SnO_2$ (calcined), CdS nanoparticles and $SnO_2$/CdS nanocomposites. The analysis was carried out at three different spots for each sample.

| Sample ID | Tin | | Cadmium | | Sulphur | | Oxygen | | Comment |
|---|---|---|---|---|---|---|---|---|---|
| | Wt% | At% | Wt% | At% | Wt% | At% | Wt% | At% | |
| $SnO_2$ | 59.5 | 16.5 | - | | - | | 40.5 | 83.5 | Uniform |
| | 62.7 | 18.5 | | | | | 37.3 | 81.5 | |
| | 62.6 | 18.4 | | | | | 37.4 | 81.6 | |
| CdS | - | | 79.5 | 52.6 | 20.5 | 47.4 | - | | Uniform |
| | | | 79.2 | 52.1 | 20.8 | 47.9 | | | |
| | | | 79.0 | 51.8 | 21.0 | 48.2 | | | |
| SC-1 | 46.7 | 16.6 | 22.1 | 8.3 | 5.3 | 6.9 | 25.9 | 68.2 | Non-uniform |
| | 47.5 | 13.3 | 10.9 | 3.2 | 2.6 | 2.7 | 39.1 | 80.9 | |
| | 31.3 | 7.7 | 18.3 | 4.8 | 5.1 | 4.6 | 45.4 | 82.9 | |
| SC-2 | 54.1 | 23.2 | 22.6 | 10.2 | 4.9 | 7.7 | 18.5 | 58.9 | Uniform |
| | 50.4 | 22.1 | 26.5 | 12.2 | 5.8 | 9.4 | 17.3 | 56.2 | |
| | 56.3 | 25.1 | 21.9 | 10.3 | 4.6 | 7.6 | 17.2 | 57.0 | |
| SC-3 | 32.5 | 12.5 | 37.5 | 15.3 | 9.6 | 13.7 | 20.4 | 58.5 | Uniform |
| | 33.7 | 12.1 | 33.6 | 12.7 | 8.8 | 11.7 | 23.8 | 63.5 | |
| | 34.6 | 12.4 | 32.9 | 12.4 | 8.0 | 10.5 | 24.5 | 64.8 | |

### 5.1.5 TEM and SAED Results

TEM analysis was done in order to know the morphology and particle size of the nanocomposites. Figure 5.7 shows the TEM images of pure $SnO_2$, CdS nanoparticles and $SnO_2$/CdS nanocomposites - SC-1, SC-2 and SC-3. Particles formed are small in size and have no specific morphology. Figure 5.8 shows particle size histograms of $SnO_2$, CdS nanoparticles and the nanocomposites. The mean particle size of pure $SnO_2$ and CdS are 9.7 nm and 11.1 nm while the mean particle size of the nanocomposites – SC-1, SC-2 and SC-3 are 12.5 nm, 12.1 nm and 10.7 nm, respectively. Selected Area Electron Diffraction (SAED) patterns of pure $SnO_2$, CdS nanoparticles and the nanocomposites (SC-1, SC-2 and SC-3) contain rings along with the spots which confirm polycrystalline nature of the nanocomposites. Rings present in pure $SnO_2$ and CdS nanoparticles are observed in the nanocomposites, confirming the presence of both phases in the nanocomposites.

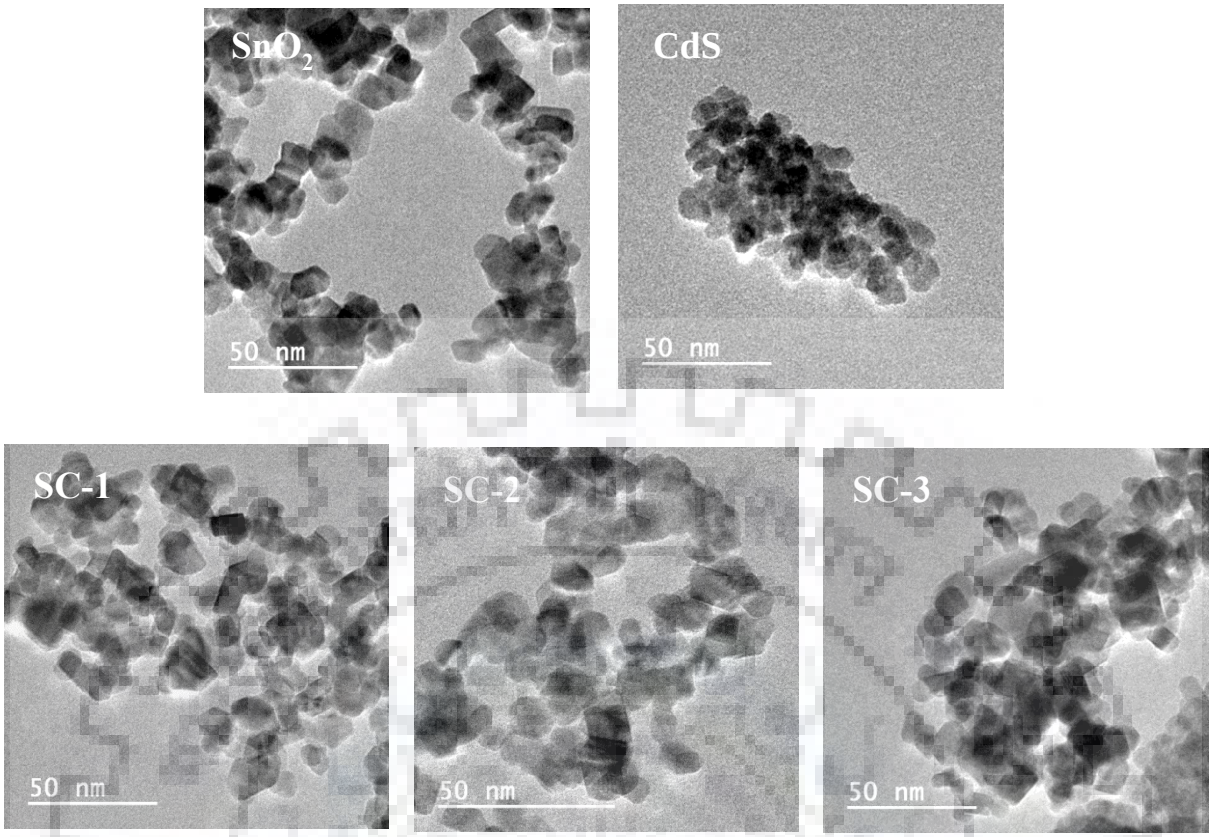


**Fig 5.7: TEM images of pure $SnO_2$ (calcined), CdS nanoparticles and $SnO_2$/CdS nanocomposites – SC-1, SC-2 and SC-3**

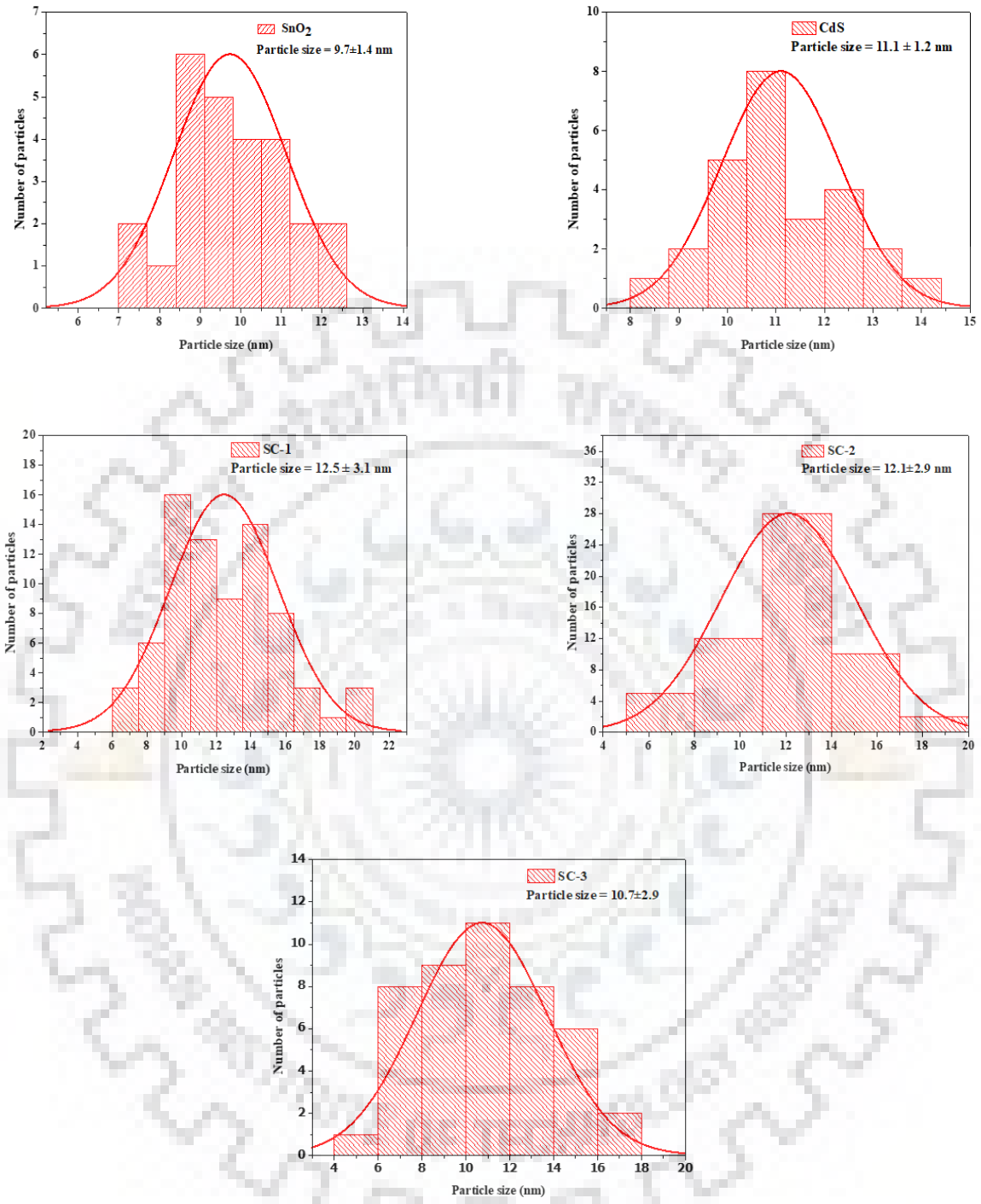


**Fig 5.8: Particle size histogram plots of $SnO_2$, CdS nanoparticles and $SnO_2$/CdS nanocomposites- SC-1, SC-2 and SC-3**

**Table 5.5** Mean particle size observed from TEM analysis

| Sample ID | Mean particle size (nm) |
|---|---|
| $SnO_2$ | 9.7 ± 1.4 |
| CdS | 11.1 ± 1.2 |
| SC-1 | 12.5 ± 3.1 |
| SC-2 | 12.1 ± 2.9 |
| SC-3 | 10.7 ± 2.9 |

Figure 5.9 shows the SAED patterns of $SnO_2$, CdS nanoparticles and $SnO_2$/CdS nanocomposites – SC-1, SC-2 and SC-3. In the nanocomposite SC-1, rings are attributed to (200), (212), (213) planes of tetragonal $SnO_2$ and (213) plane of hexagonal CdS. SC-2 shows ring corresponding to (310) plane of tin oxide and other two rings correspond to (321), (300) planes of CdS. Similarly, SC-3 shows rings which are attributed to (301), (321) planes of $SnO_2$ and other rings due to (313), (321), (220) planes of CdS. Hence, SAED results confirm that both $SnO_2$ and CdS phases are present in the nanocomposites and they all are polycrystalline in nature.

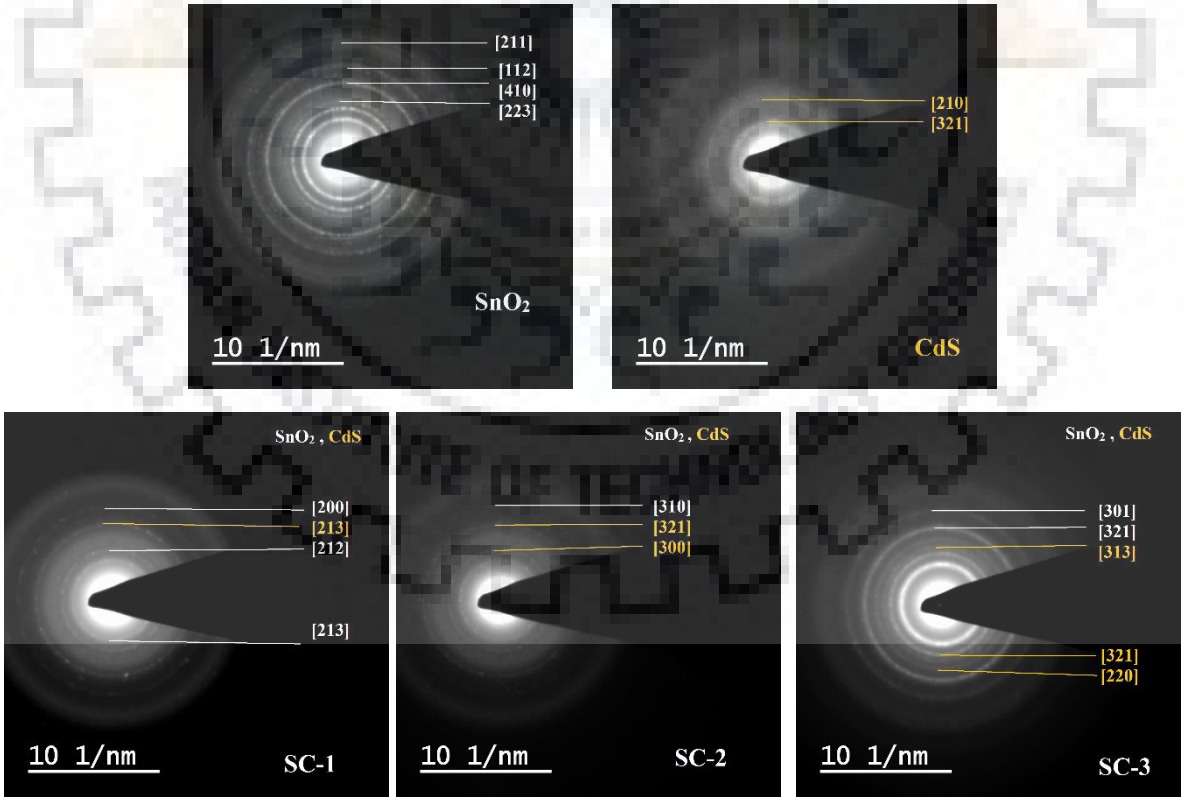


**Fig 5.9: SAED patterns of pure $SnO_2$ (calcined), CdS nanoparticles and $SnO_2$/CdS nanocomposites- SC-1, SC-2 and SC-3**

High resolution TEM images of the $SnO_2$/CdS nanocomposites are shown in Figure 5.10. In the nanocomposites (SC-1, SC-2 and SC-3), the lattice fringe spacing of 0.33 nm is attributed to (110) plane of $SnO_2$ and lattice fringe spacing of 0.35 nm is attributed to (100) plane of CdS nanoparticles.

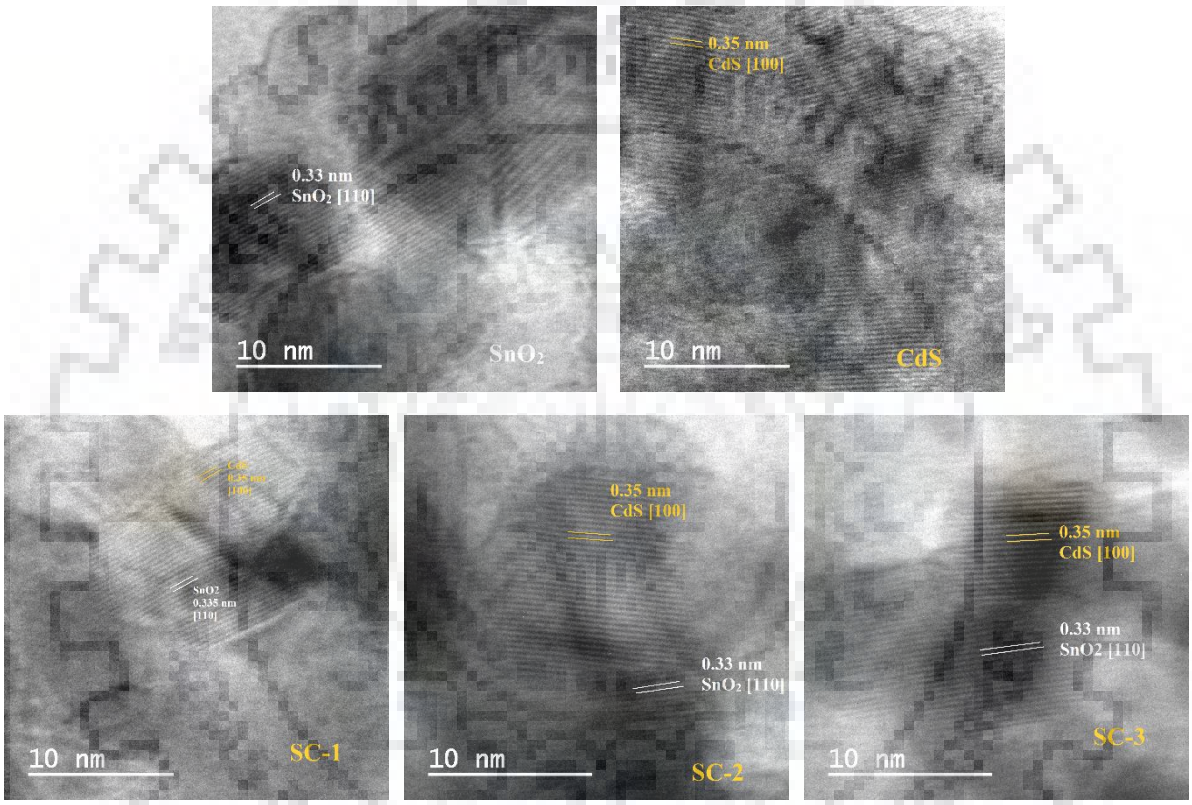


**Fig 5.10: HR-TEM images of pure $SnO_2$, CdS nanoparticles and the $SnO_2$/CdS nanocomposites – SC-1, SC-2 and SC-3**

### 5.1.6 UV-Visible Diffuse Reflectance Spectral Analysis

Optical spectral analysis of the $SnO_2$/CdS nanocomposites was done using UV-Visible Diffuse Reflectance Spectroscopy (UV-Vis DRS). Figure 5.11 shows the DRS spectra and Tauc plots of pure $SnO_2$, CdS nanoparticles and the nanocomposites – SC-1, SC-2 and SC-3.

Band gap values for the $SnO_2$, CdS and the $SnO_2$/CdS nanocomposites were obtained from the Tauc plots. The band gap values estimated for pure tin oxide and cadmium sulphide nanoparticles are 3.9 eV [51] and 2.41 eV [62], respectively. In the case of nanocomposites, two band gaps are observed, due to both tin oxide and cadmium sulphide. Nanocomposites - SC-1, SC-2 and SC-3 exhibit band gap values as 3.43 eV, 3.5 eV and 3.48 eV, respectively, due to $SnO_2$ and due to CdS they exhibit 2.42 eV, 2.36 eV and 2.25 eV, respectively. The change in band gap values on going from pure nanoparticles to the nanocomposites is due to the change in crystallite size. The band gap values and crystallite sizes are summarized in the table 5.6. From the table it is observed clearly that the band gap increases with decrease in the crystallite size, showing quantum confinement effect.

**Table 5.6** Band gap and crystallite size of pure $SnO_2$, CdS nanoparticles and $SnO_2$/CdS nanocomposites – SC-1, SC-2 and SC-3.

| Sample ID | Band gap (eV) | | Crystallite size (nm) | |
|---|---|---|---|---|
| | $SnO_2$ | CdS | $SnO_2$ | CdS |
| $SnO_2$ | 3.9 | - | 9.9 | - |
| CdS | - | 2.41 | - | 7.2 |
| SC-1 | 3.43 | 2.42 | 11.6 | 7.1 |
| SC-2 | 3.5 | 2.36 | 11.3 | 8.1 |
| SC-3 | 3.48 | 2.25 | 11.4 | 8.3 |

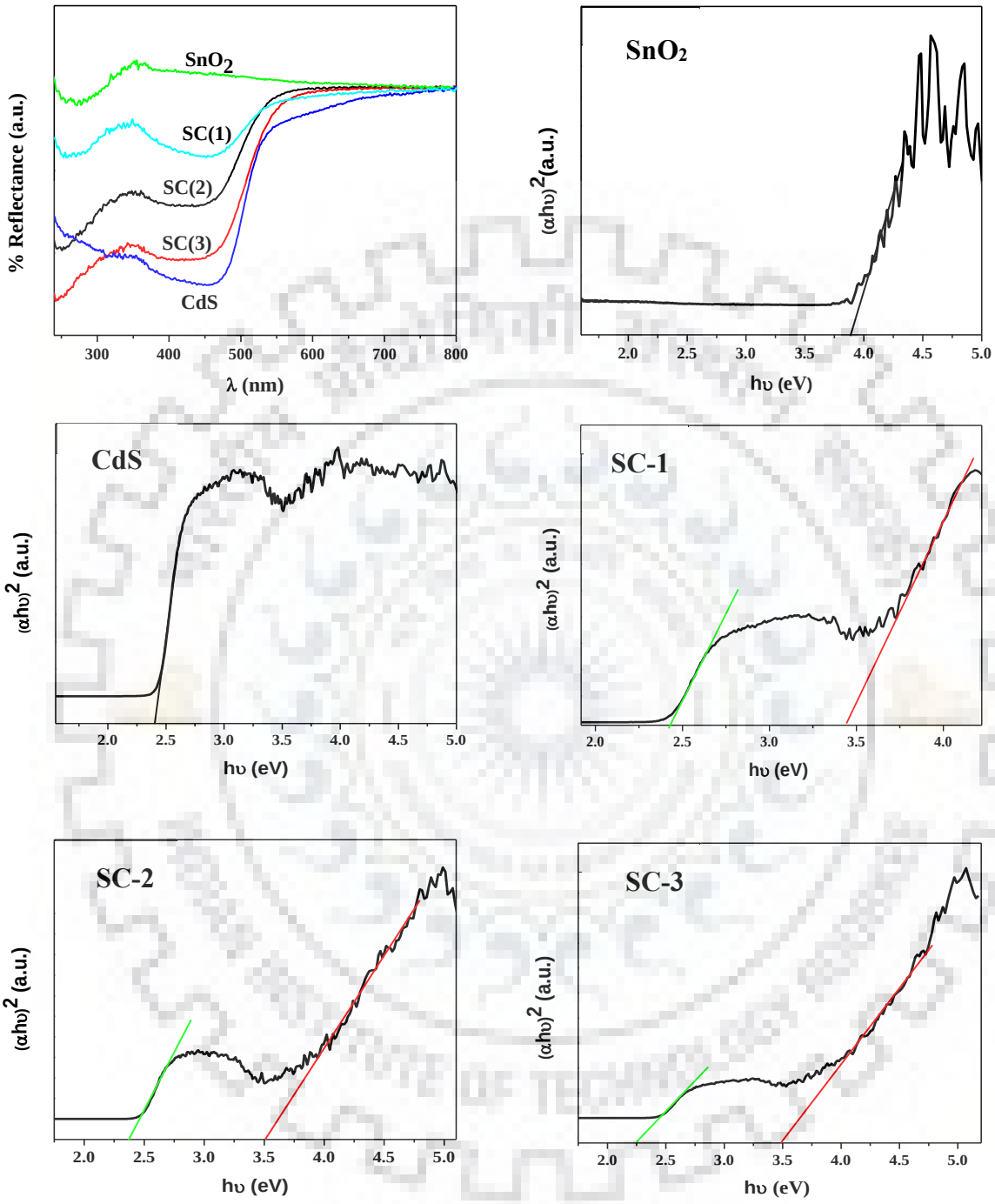


**Fig 5.11: DRS spectra and the Tauc plots of pure $SnO_2$, CdS nanoparticles and the $SnO_2$/CdS nanocomposites (SC-1, SC-2 and SC-3)**

### 5.1.7 Surface Area Analysis

Surface area of $SnO_2$, CdS nanoparticles and $SnO_2$/CdS nanocomposites were measured using Brunauer-Emmett-Teller surface area analyzer. Surface area of pure $SnO_2$, CdS nanoparticles and $SnO_2$/CdS nanocomposites (SC-1, SC-2 and SC-3) are 73.9 $m^2/g$, 72.8 $m^2/g$, 90.8 $m^2/g$, 79.4 $m^2/g$ and 61.5 $m^2/g$, respectively. Nanocomposites SC-1 and SC-2 have higher surface area than the parent nanoparticles.

### 5.2 Nanocomposites synthesized using single molecular precursor

First, the characterization results for the single molecular precursor are presented and this is followed by that for the $SnO_2$/CdS nanocomposites.

### 5.2.1 Characterization of bis(thiourea) cadmium acetate complex

#### 5.2.1.1 XRD

X-ray diffraction pattern of the bis(thiourea) cadmium acetate complex matches with JCPDS File No. 33-0228, which confirms the formation of orthorhombic crystals of bis(thiourea) cadmium acetate complex. The peaks at 2θ values of 12.86°, 13.53°, 15.06°, 22.8°, 26.17° and 34.92° correspond to (101), (012), (111), (122), (104) and (016) planes of the complex.

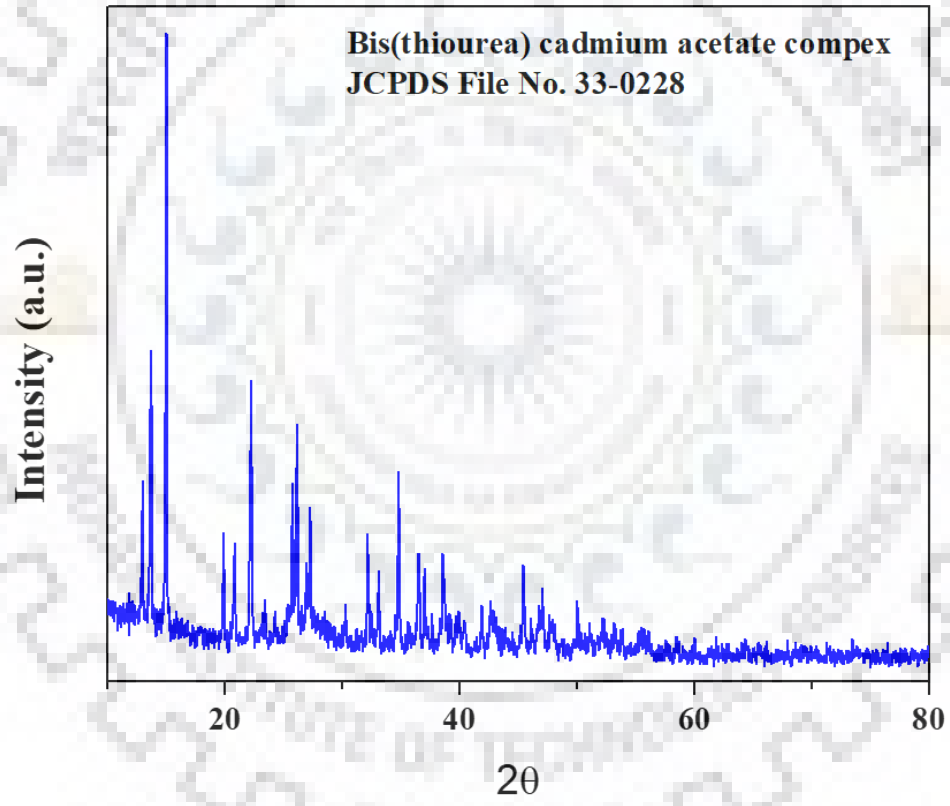


**Fig 5.12: XRD pattern of bis(thiourea) cadmium acetate complex**

#### 5.2.1.2 FT-IR Spectroscopy Results

FT-IR spectrum of the cadmium complex is given in Figure 5.13. In bis(thiourea) cadmium acetate, cadmium is coordinated to thiourea through sulphur and acetate through oxygen in tetrahedral fashion. In the IR spectrum, there is a broad peak at 2766 and 3431 $cm^{-1}$ due to symmetric and asymmetric vibrations of $NH_2$ group. The C=S symmetric stretching is observed

at 713 $cm^{-1}$, while in thiourea it is present at 727 $cm^{-1}$. The reduction in frequency is due to the lowering of double bond character of C=S on coordination with cadmium. The peak at 1111 $cm^{-1}$ in the complex and 1082 $cm^{-1}$ in thiourea is due to N-C-N stretching vibration. The reduction in the stretching frequency is due to the enhancement of double bond character of carbon bonded with nitrogen due to the formation of complex [63, 64]. The IR bands observed at 713 $cm^{-1}$, 623 $cm^{-1}$ and 481 $cm^{-1}$ are attributed to symmetric stretching of -CS, asymmetric bending of –NCS and symmetric bending of –NCS, respectively.

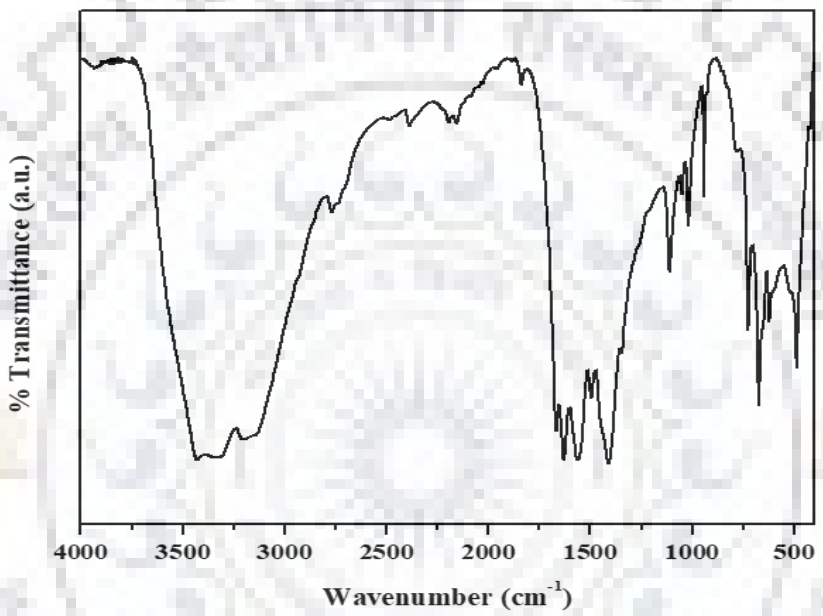


**Fig 5.13: FT-IR spectrum of bis(thiourea) cadmium acetate complex**

**Table 5.7** Assignment of IR bands in pure thiourea and bis(thiourea) cadmium acetate

| **IR band position ($cm^{-1}$)** | | **Assignment** |
|---|---|---|
| **Cadmium complex** | **Thiourea** | |
| 3431,2766 | | Symmetric and asymmetric stretching vibrations of $–NH_2$ group |
| 1669 | 1627 | Bending vibration of $-NH_2$ group |
| 1496 | 1468 | Stretching vibration of N-C-N |
| 1409 | 1408 | Stretching vibration of C=S |
| 1111 | 1082 | Symmetric stretching of -CN |

| | | |
|---|---|---|
| 713 | 727 | Symmetric stretching of -CS |
| 623 | 630 | Asymmetric bending of -NCS |
| 481 | 469 | Symmetric bending of -NCS |

### 5.2.1.3 TGA Results

TGA and DTG results for bis(thiourea) cadmium acetate are shown in Figure 5.14. Up to 285 ºC, there is a weight loss of about 48.8 % due to decomposition of the complex. At 552 ºC, there is a partial oxidation of CdS to CdS.CdO and is inferred by the weight loss of 11.6 %. A weight gain is observed at 610 ºC due to the formation of $CdSO_4$. The decomposition of $CdSO_4$ at 910 ºC, gives CdO. The complete oxidation of CdS takes place at 910 ºC with the formation of CdO [60].

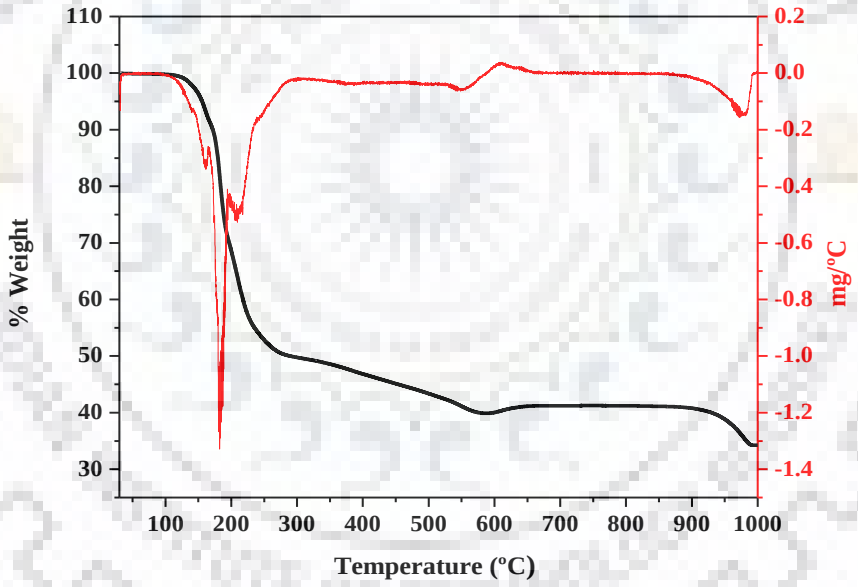


**Fig 5.14: TGA and DTG patterns of bis(thiourea) cadmium acetate complex**

**Table 5.8** Thermogravimetric analysis results of bis(thiourea) cadmium acetate

| Temperature range (°C) | % Wt. gain/loss | DTG peak (°C) | Comment |
|---|---|---|---|
| 180 - 285 | - 48.8 | 184 | Due to decomposition of complex |
| 285 - 570 | - 11.6 | 552 | Due to partial oxidation of CdS to CdS.CdO. |
| 602 - 640 | + 1.3 | 610 | Partial oxidation forming $CdS.CdSO_4$ |
| 875 - 990 | - 6.7 | 980 | Formation of CdO due to the decomposition of $CdSO_4$. |

### 5.2.1.4 Elemental Analysis Results

Elemental analysis was done by CHNS analysis and the results are given in Table 5.9. The results are in good agreement with the theoretical values.

**Table 5.9** CHNS data for bis(thiourea) cadmium acetate

| Element | Theoretical (%) | Observed (%) |
|---|---|---|
| Carbon | 18.8 | 18.4 |
| Hydrogen | 3.7 | 3.5 |
| Nitrogen | 14.6 | 15.2 |
| Sulphur | 16.7 | 17.2 |

### 5.2.2 $SnO_2$/CdS nanocomposites synthesized through single molecular precursor

#### 5.2.2.1 XRD Results

XRD patterns of $SnO_2$, CdS nanoparticles and $SnO_2$/CdS nanocomposites are given in Figure 5.15. XRD patterns of $SnO_2$ and CdS nanoparticles match with the JCPDS File No. 41-1445 and 47-1179, confirming the formation of tetragonal $SnO_2$ and hexagonal CdS nanoparticles, respectively. Formation of nanocomposites are confirmed by the presence of XRD peaks due to both $SnO_2$ and CdS. The nanocomposites show peaks at 26.5°, 33.79°, 37.95°, 51.9° and 54.57° which correspond to (110), (101), (200), (211) and (220) planes of $SnO_2$. Peaks at 43.5° and 47.4° are attributed to planes (110) and (103) are due to the presence of CdS in the composites. With an increase in the concentration of bis(thiourea) cadmium acetate complex, the peaks due to CdS become more prominent as the concentration of CdS in the nanocomposites increases. The crystallite size was calculated using Debye Scherrer's equation. The crystallite size of $SnO_2$ and CdS are 9.9 nm and 10.8 nm, respectively. The crystallite size of nanocomposites (SCC-1, SCC-2 and SCC-3), calculated using (101) plane of $SnO_2$ are 12.0 nm, 11.3 nm and 10.9 nm and the crystallite size of CdS in the nanocomposites (SCC-1, SCC-2 and SCC-3) calculated using (110) plane of CdS are 11.9 nm, 12.2 nm and 12.8 nm, respectively.

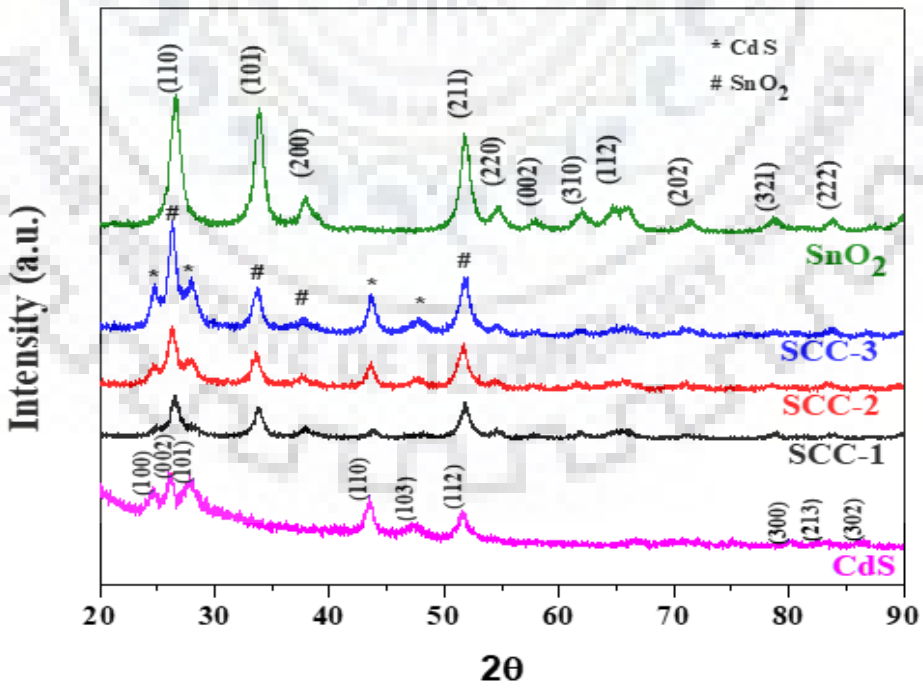


**Fig 5.15: XRD patterns of pure $SnO_2$, CdS nanoparticles and $SnO_2$/CdS nanocomposites (SCC-1, SCC-2 and SCC-3)**

**Table 5.10** Crystallite size of $SnO_2$ and CdS in $SnO_2$/CdS nanocomposites

| Sample ID | Crystallite size of $SnO_2$ (nm) | Crystallite size of CdS (nm) |
|---|---|---|
| SCC-1 | 12.0 | 11.9 |
| SCC-2 | 11.3 | 12.2 |
| SCC-3 | 10.9 | 12.8 |
| CdS | - | 10.8 |
| Calcined $SnO_2$ | 9.9 | - |

### 5.2.2.2 FT-IR Spectroscopy Results

FT-IR spectroscopy is used to confirm the functional groups present in the samples. The IR spectra were recorded for pure $SnO_2$, CdS nanoparticles and the nanocomposites (SCC-1, SCC-2 and SCC-3). Figure 5.16 show the IR spectra and the data are summarized in Table 5.11. Bands at 630 $cm^{-1}$ and 557 $cm^{-1}$ in pure $SnO_2$ and CdS are due to the stretching vibrations of Sn-O and Cd-S bond [57, 58]. There is a reduction in the frequency of Sn-O and Cd-S bond in the nanocomposites, due to molecular interaction. The IR bands in the range of 1400 $cm^{-1}$ and 1100 $cm^{-1}$ are due to the presence of organic moieties.

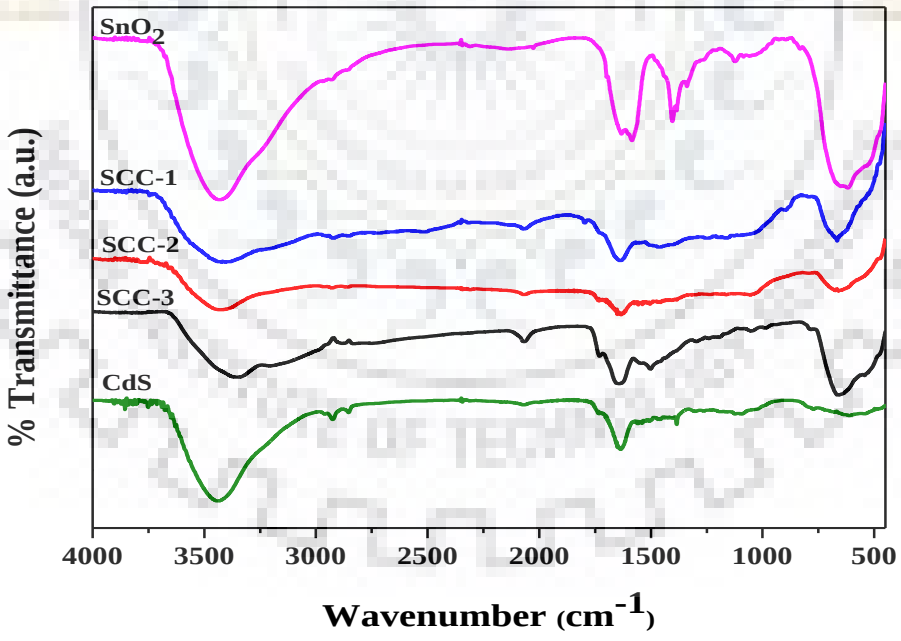


**Fig 5.16: FT-IR spectra of pure $SnO_2$, CdS nanoparticles and $SnO_2$/CdS nanocomposites (SCC-1, SCC-2 and SCC-3)**

**Table 5.11** Summary of IR data for the $SnO_2$/CdS nanocomposites

| IR band position ($cm^{-1}$) of the nanocomposites | | | | | Assignment |
|---|---|---|---|---|---|
| **$SnO_2$** | **CdS** | **SCC-1** | **SCC-2** | **SCC-3** | |
| 3430 | 3440 | 3411 | 3421 | 3360 | Stretching vibration of –OH |
| 2925, 2829 | 2923, 2849 | 2915, 2851 | 2926, 2859 | 2919, 2854 | Stretching vibration of -CH |
| 1630 | 1634 | 1634 | 1634 | 1634 | Bending vibration of -OH |
| 1400 | 1388 | 1455 | - | 1494 | Bending vibration of C-H |
| - | 1105 | - | - | - | Stretching vibration of C-O |
| 630 | - | 664 | 664 | 654 | Stretching vibration of Sn-O |
| - | 557 | 527 | 530 | 528 | Stretching vibration of Cd-S |

### 5.2.2.3 TGA and DTA Results

Figure 5.17 shows the TGA and DTA patterns of pure $SnO_2$, CdS nanoparticles and the $SnO_2$/CdS nanocomposites (SCC-1, SCC-2 and SCC-3). Tin dioxide being very stable, shows weight loss of about 2.1 % due to removal of moisture and organic moieties. CdS nanoparticles show a weight loss of about 15.8 % due to removal of adsorbed moisture and organic moieties [59], followed by a weight gain of 4.1 % due to oxidation of CdS to $CdSO_4$ and a weight loss of 16.7 % due to decomposition of $CdSO_4$ which ultimately gives CdO.

Nanocomposites show TGA patterns due to CdS, since $SnO_2$ nanoparticles are very stable in the temperature regime investigated. The nanocomposites follow the same behavior as that of pure CdS. Initially, they show a weight loss of 5.6 – 7.5 % over the temperature range of up to 480 ºC, due to removal of moisture and organic moieties. In the temperature range of 470 ºC to 575 ºC, they show weight gain due to formation of $CdSO_4$ [60]. Above 700 ºC, complete oxidation of CdS takes place [61], i.e. formation of CdO which leads to the weight loss.

DTA plots of CdS, as prepared $SnO_2$ nanoparticles and $SnO_2$/CdS nanocomposites (SCC-1, SCC-2 and SCC-3) are given in Figure 5.17 (f). Two exothermic peaks are observed in the nanocomposites (SCC-1, SCC-2 and SCC-3). The first exothermic peak is observed at 497 ºC, 506 ºC and 523 ºC in SCC-1, SCC-2 and SCC-3, respectively. The second exothermic peak is

observed in the nanocomposites at 888 ºC, 914 ºC and 923 ºC, respectively. These peaks are due to the oxidation of CdS or formation of $CdSO_4$ and the second peak is due to the decomposition of $CdSO_4$ (complete | oxidation of CdS).

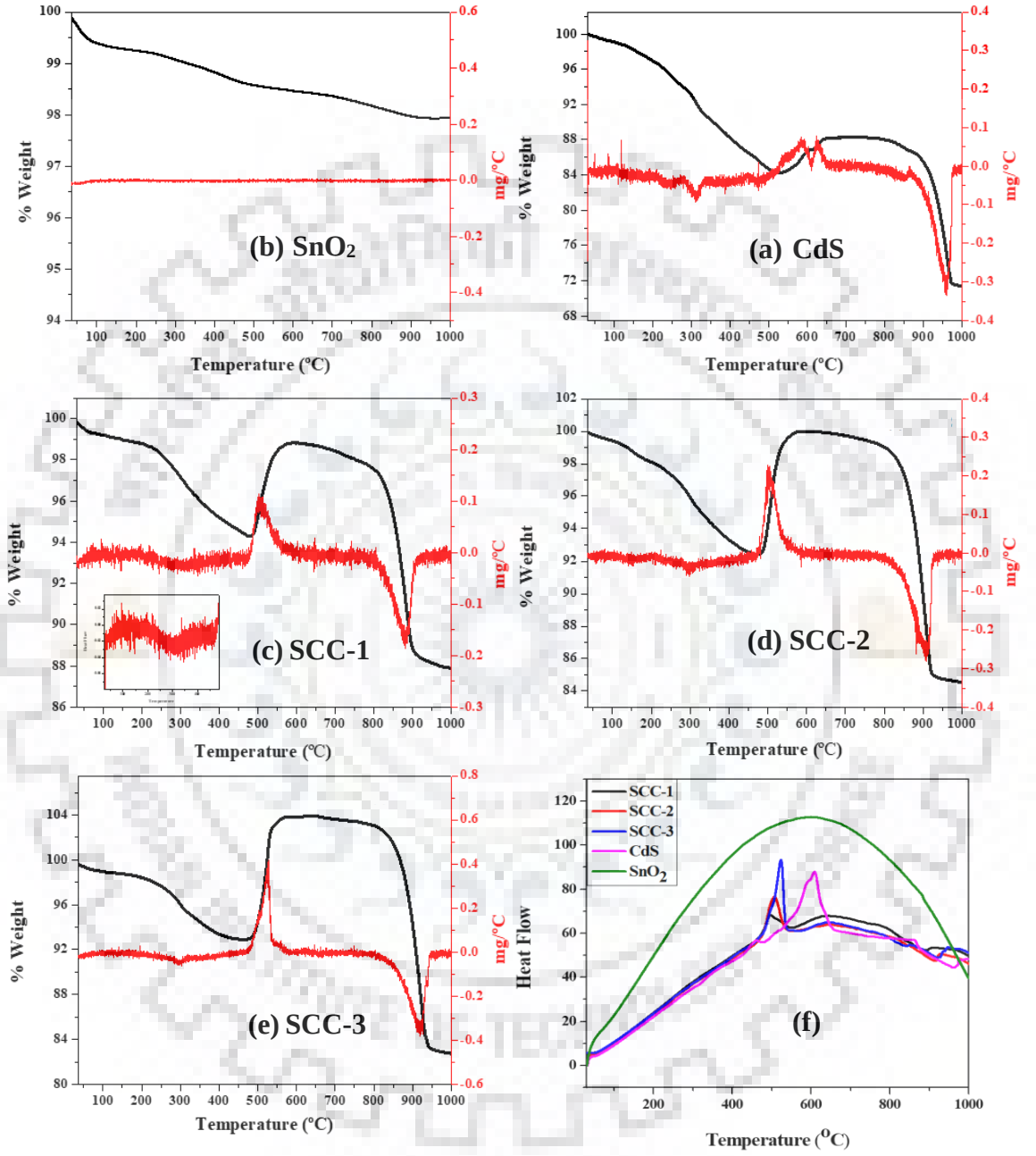


**Fig 5.17: TGA and DTG (a-e), and DTA (f) patterns of pure $SnO_2$, CdS nanoparticles and $SnO_2$/CdS nanocomposites (SCC-1, SCC-2 and SCC-3)**

**Table 5.12** Thermogravimetric analysis results of $SnO_2$/CdS nanocomposites

| Sample ID | Temperature range (°C) | DTA peak position (°C) | %wt. loss/ gain | Overall % wt. loss |
|---|---|---|---|---|
| $SnO_2$ | - | - | -2.1 | 2.1 |
| CdS | Up to 480 | 455 | -15.8 | 28.3 |
| | 550 – 650 | 608 | +5.1 | |
| | 830 –1000 | 959 | -16.7 | |
| SCC-1 | Up to 480 | - | -4.5 | 9.0 |
| | 480 – 575 | 497 | +4.6 | |
| | 795 – 970 | 888 | -9.1 | |
| SCC-2 | Up to 464 | - | -7.4 | 14.9 |
| | 475 – 575 | 506 | +7.5 | |
| | 825 – 950 | 914 | -15.0 | |
| SCC-3 | Up to 435 | - | -7.1 | 22.5 |
| | 480 – 570 | 523 | +11.0 | |
| | 730 – 975 | 923 | -20.7 | |

### 5.2.2.4 FE-SEM and EDX Analyses

This technique uses back scattered and secondary electrons to form surface images of the samples. SEM images of pure $SnO_2$, CdS nanoparticles and the nanocomposites SCC-1, SCC-2 and SCC-3 are given in Figure 5.18. The particles are small in size and have no specific morphology.

EDX analysis gives composition of the nanocomposites. It shows that pure $SnO_2$ nanoparticles consist of tin and oxygen and CdS nanoparticles consist of cadmium and sulphur, confirming purity of the nanoparticles. Similarly, in $SnO_2$/CdS nanocomposites only tin, cadmium, oxygen and sulphur are present.

The EDX data are summarized in Table 5.13. It gives information about uniform composition of the samples. Nanocomposites SCC-2 and SCC-3 are uniform in composition while SCC-1 is non-uniform.

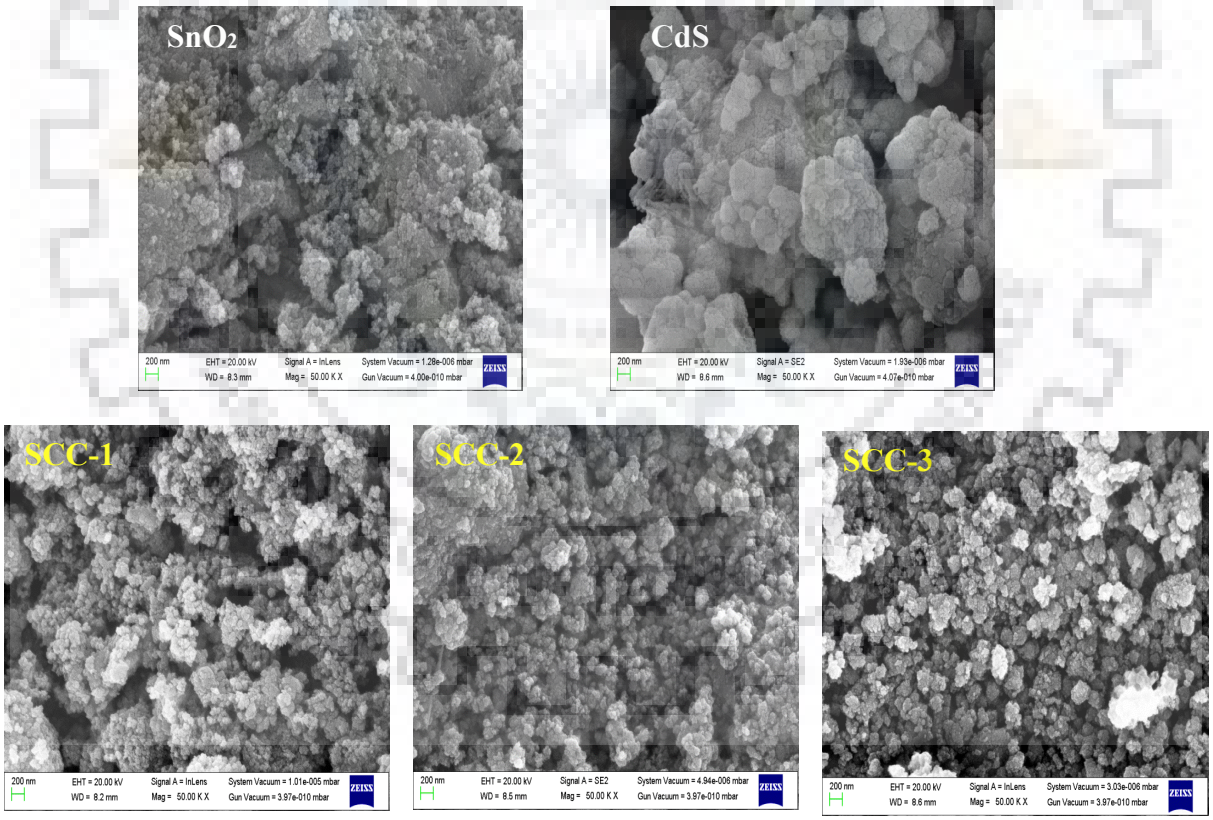


**Fig 5.18: SEM images of pure $SnO_2$, CdS nanoparticles and $SnO_2$/CdS nanocomposites (SCC-1, SCC-2 and SCC-3)**

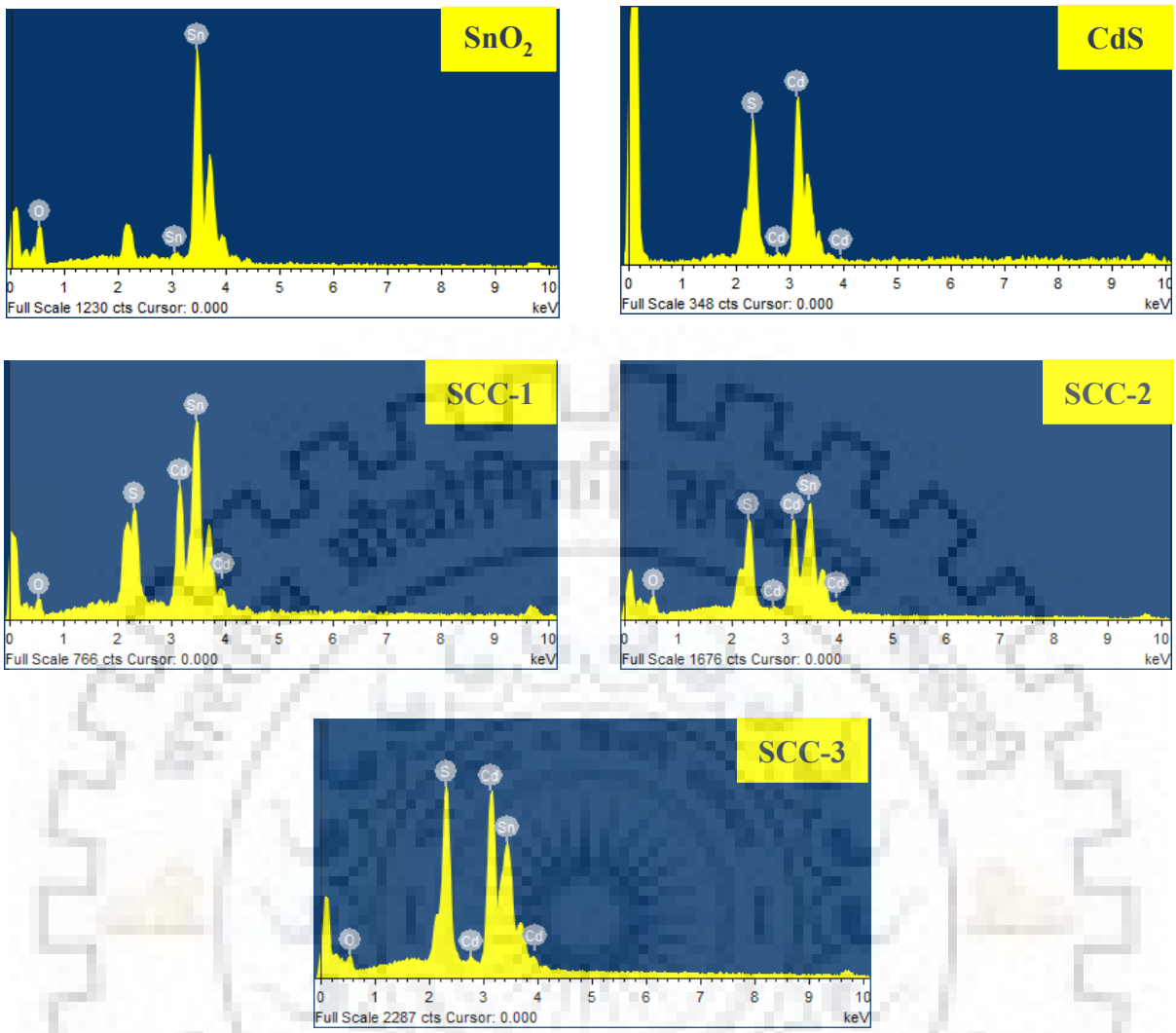


**Fig 5.19 EDX pattern of pure $SnO_2$ (calcined), CdS nanoparticles and $SnO_2$/CdS nanocomposites (SCC-1, SCC-2 and SCC-3)**

**Table 5.13** EDX analysis data of $SnO_2$, CdS nanoparticles and $SnO_2$/CdS nanocomposites. The analysis was carried out at three different spots for each sample.

| Sample ID | Tin | | Cadmium | | Sulphur | | Oxygen | | Comment |
|---|---|---|---|---|---|---|---|---|---|
| | Wt% | At% | Wt% | At% | Wt% | At% | Wt% | At% | |
| $SnO_2$ | 59.5 | 16.5 | - | | - | | 40.5 | 83.5 | Uniform |
| | 62.7 | 18.5 | | | | | 37.3 | 81.5 | |
| | 62.6 | 18.4 | | | | | 37.4 | 81.6 | |
| CdS | - | | 81.8 | 56.1 | 18.2 | 43.9 | - | | Uniform |
| | | | 80.3 | 53.8 | 19.7 | 46.3 | | | |
| | | | 80.0 | 53.2 | 20.0 | 46.8 | | | |
| SCC-1 | 48.5 | 21.4 | 29.5 | 13.8 | 4.7 | 7.6 | 17.4 | 57.2 | Non-uniform |
| | 50.0 | 24.3 | 30.4 | 15.6 | 5.8 | 10.3 | 13.8 | 49.8 | |
| | 51.1 | 23.3 | 27.9 | 13.5 | 4.7 | 7.9 | 16.4 | 55.4 | |

| | | | | | | | | | |
|---|---|---|---|---|---|---|---|---|---|
| SCC-2 | 40.4 | 16.9 | 33.4 | 12.9 | 8.5 | 11.9 | 17.8 | 61.2 | Uniform |
| | 41.5 | 14.3 | 31.3 | 14.7 | 7.9 | 13.2 | 19.3 | 55.2 | |
| | 37.5 | 16.8 | 32.7 | 13.4 | 7.9 | 11.8 | 21.8 | 58 | |
| SCC-3 | 27.8 | 12.13 | 45.4 | 20.9 | 12.3 | 19.8 | 14.5 | 47.1 | Uniform |
| | 27.3 | 11.9 | 45.6 | 20.9 | 12.5 | 20.2 | 14.6 | 47.04 | |
| | 27.9 | 11.8 | 44.2 | 19.7 | 12.0 | 18.8 | 15.9 | 49.7 | |

### 5.2.2.5 TEM Results

Figure 5.20 shows TEM images of pure $SnO_2$, CdS nanoparticles and $SnO_2$/CdS nanocomposites (SCC-1, SCC-2 and SCC-3). TEM analysis gives idea about morphology and particle size of the samples. The mean particle size values of pure $SnO_2$ and CdS nanoparticles are 9.7±1.4 nm and 13.2±2.4 nm, respectively. Size histogram plots are given in Figure 5.21. The mean particle size of nanocomposites SCC-1, SCC-2 and SCC-3 are 10.8±2.5 nm, 11.3±2.1 nm and 10.5±3.1 nm, respectively. SAED patterns show that the $SnO_2$, CdS nanoparticles and $SnO_2$/CdS nanocomposites are polycrystalline in nature.

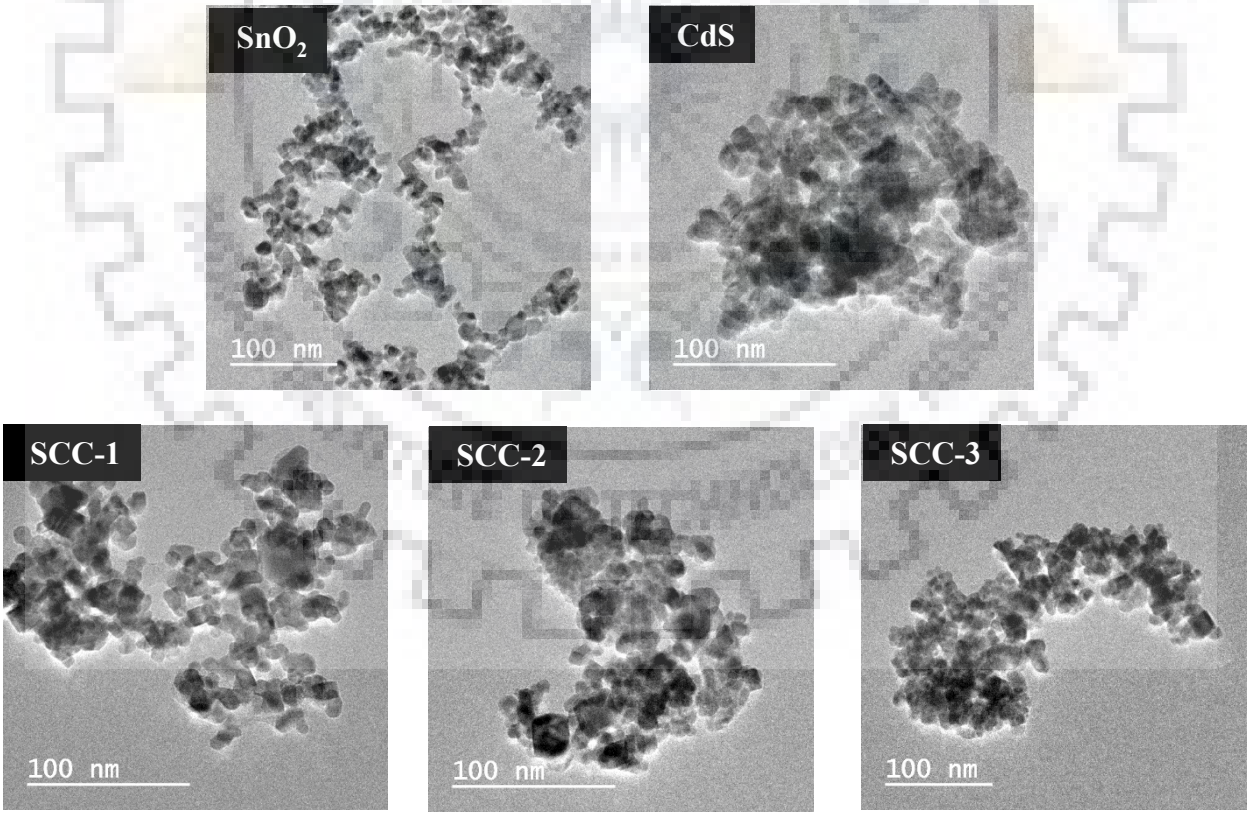


**Fig 5.20 TEM images of pure $SnO_2$, CdS nanoparticles and $SnO_2$/CdS nanocomposites (SCC-1, SCC-2 and SCC-3)**

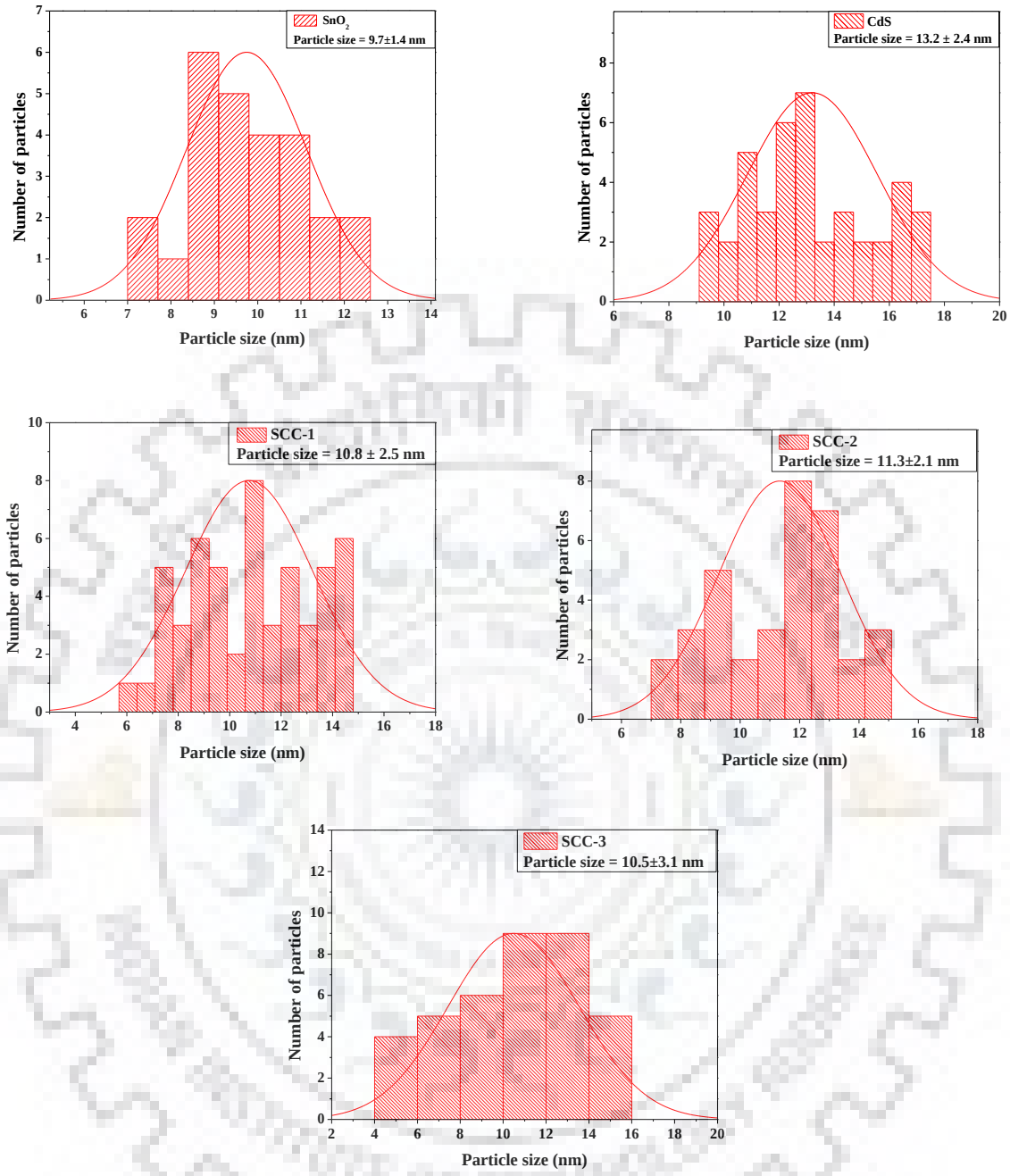


**Fig 5.21: Particle size histogram plots of $SnO_2$, CdS and nanocomposites- SCC-1, SCC-2 and SCC-3**

**Table 5.14** Mean particle size of $SnO_2$/CdS nanocomposites obtained from TEM analysis

| Sample ID | Mean particle size |
|---|---|
| $SnO_2$ | 9.7 ± 1.4 nm |
| CdS | 13.2 ± 2.4 nm |
| SCC-1 | 10.8 ± 2.1 nm |
| SCC-2 | 11.3 ± 2.1 nm |
| SCC-3 | 10.5 ± 3.1 nm |

Figure 5.22 show SAED patterns of pure $SnO_2$, CdS nanoparticles and nanocomposites- SCC-1, SCC-2 and SCC-3. In nanocomposite SCC-1, rings attributed to (220), (330) planes of tetragonal $SnO_2$ and (110) and (403) planes of hexagonal CdS are observed. Also, nanocomposite SCC-2 shows rings corresponding to (220) and (330) planes of tin oxide and a ring corresponding to (210) plane of hexagonal CdS. Similarly, SCC-3 have rings which are attributed to (330) plane of $SnO_2$ and a ring due to (403) plane of CdS. SAED result confirm that both the phases are present in the nanocomposites and they are polycrystalline in nature.

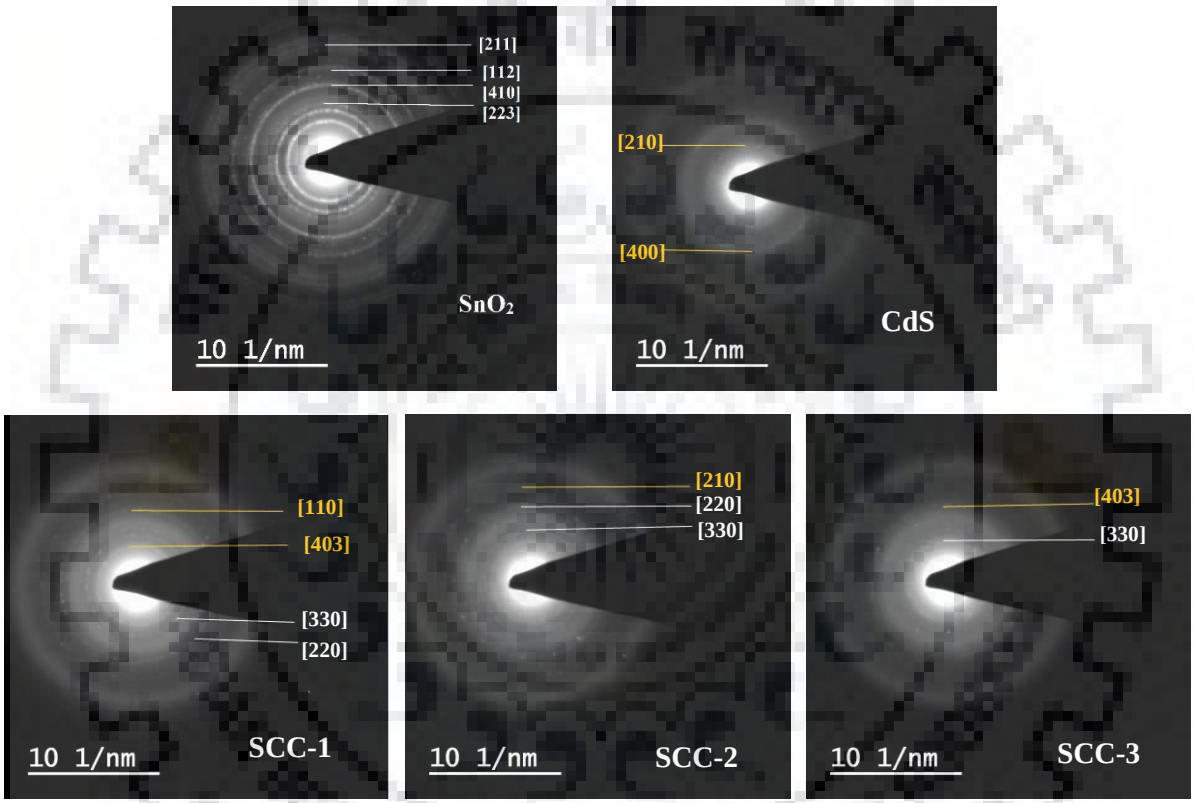


**Fig 5.22: SAED patterns of pure $SnO_2$ (calcined), CdS and $SnO_2$/CdS nanocomposites – SCC-1, SCC-2 and SCC-3**

HR-TEM images of pure $SnO_2$, CdS nanoparticles and the $SnO_2$/CdS nanocomposites are given in Figure 5.23. $SnO_2$ nanoparticles show an interplanar spacing of 0.33 nm which is attributed to (110) plane of $SnO_2$ (JCPDS File No. 41-1445) and CdS nanoparticles show an interplanar spcing of 0.35 nm, due to (100) plane of CdS (JCPDS File No. 47-1179). The nanocomposites (SCC-1, SCC-2 and SCC-3) show interplanar spacing due to both $SnO_2$ and CdS

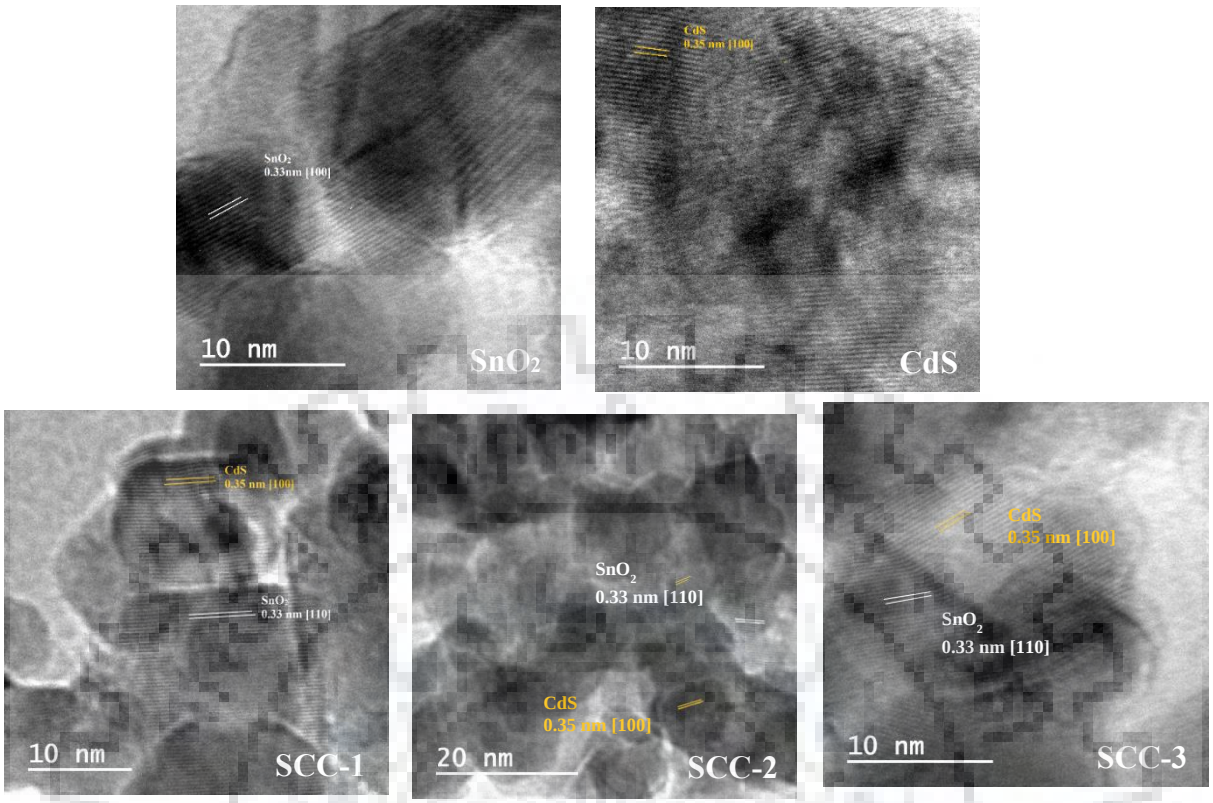


**Fig 5.23: HR-TEM images of pure $SnO_2$ (calcined), CdS nanoparticles and $SnO_2$/CdS nanocomposites- SCC-1, SCC-2 and SCC-3**

### 5.2.2.6 DRS Analysis

DRS spectra and the Tauc plots of pure $SnO_2$, CdS nanoparticles and $SnO_2$/CdS nanocomposites are given in Figure 5.24. The nanocomposites exhibit two absorption bands, one in the UV region due to $SnO_2$ and the other in the visible region due to CdS. The presence of two absorption bands confirms the formation of $SnO_2$/CdS nanocomposites.

The band gap and the crystallite size values are summarised in Table 5.15. Pure $SnO_2$ nanoparticles being active in UV range show a band gap of 3.9 eV [51] while CdS nanoparticles have a band gap of 2.4 eV [65], active in the visible range. Nanocomposites show two band gaps, due to both $SnO_2$ and CdS. The band gap of $SnO_2$ decreases on going from pure phase to the nanocomposites i.e. from 3.9 eV to 3.2 eV, due to change in the crystallite size of $SnO_2$. The band gap of CdS in the nanocomposites (SCC-1, SCC-2 and SCC-3 are 2.39 eV, 2.31 eV and 2.2 eV respectively) is lower as compared to band gap in the pure phase (2.43 eV) due to

increase in the crystallite size of CdS in the $SnO_2$/CdS nanocomposites, showing quantum confinement effect.

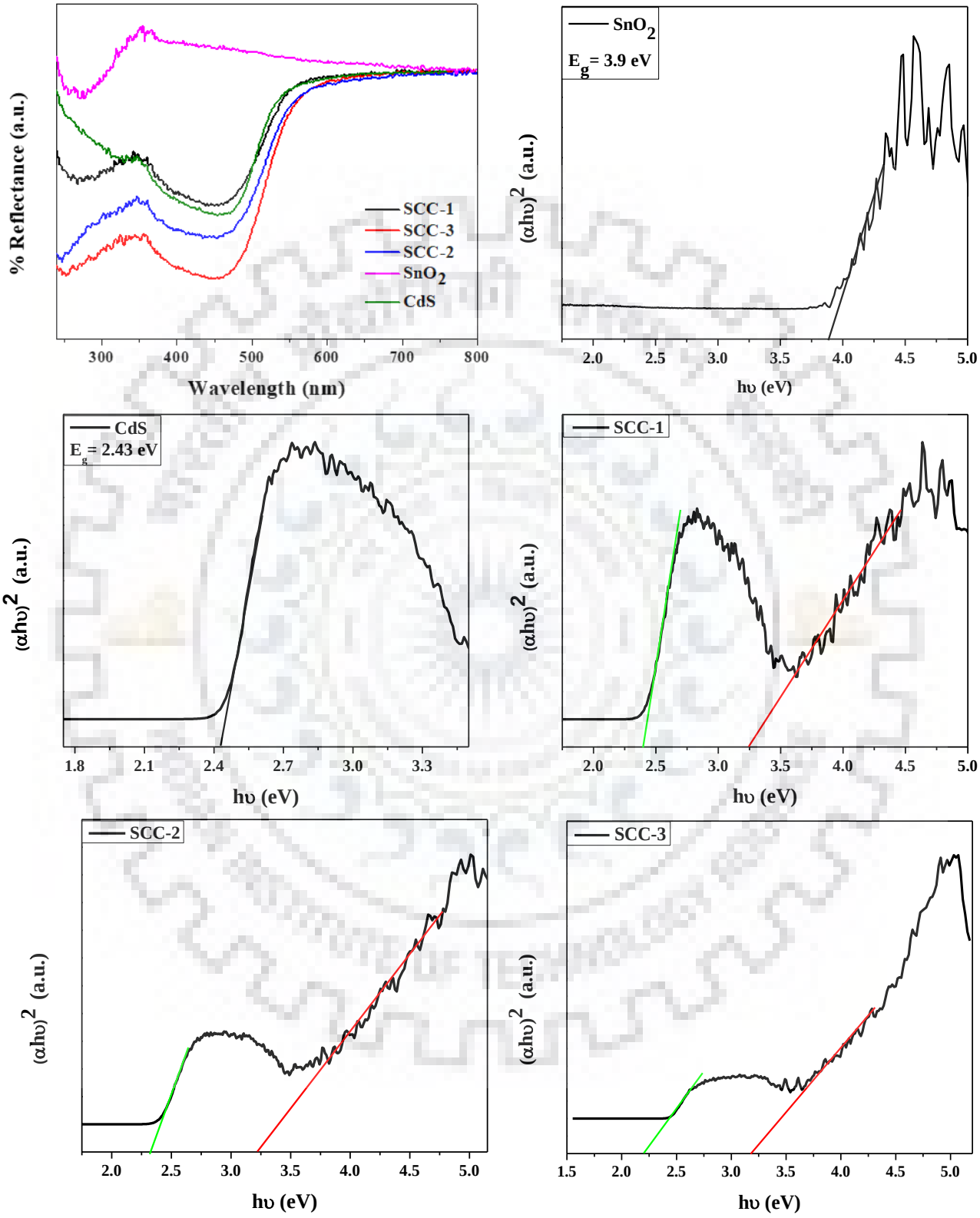


**Fig 5.24: DRS spectra and the Tauc plots of pure $SnO_2$, CdS nanoparticles and $SnO_2$/CdS nanocomposites (SCC-1, SCC-2 and SCC-3)**

**Table 5.15** Band gap and crystallite size of pure $SnO_2$, CdS nanoparticles and $SnO_2$/CdS nanocomposites – SCC-1, SCC-2 and SCC-3.

| Sample ID | Band gap (eV) | | Crystallite size (nm) | |
|---|---|---|---|---|
| | $SnO_2$ | CdS | $SnO_2$ | CdS |
| $SnO_2$ | 3.9 | - | 9.9 | - |
| CdS | - | 2.43 | - | 10.8 |
| SCC-1 | 3.24 | 2.39 | 11.9 | 11.9 |
| SCC-2 | 3.22 | 2.31 | 11.3 | 12.2 |
| SCC-3 | 3.20 | 2.20 | 10.9 | 12.8 |

### 5.2.2.7 Surface Area Analysis

Surface area of $SnO_2$, CdS nanoparticles and $SnO_2$/CdS nanocomposites were measured using Brunauer-Emmett-Teller surface area analyzer. The surface area of pure $SnO_2$, CdS nanoparticles and nanocomposites (SCC-1, SCC-2 and SCC-3) are 73.9 $m^2/g$, 62.1 $m^2/g$, 81.4 $m^2/g$, 58.1 $m^2/g$ and 61.7 $m^2/g$, respectively. Nanocomposite SCC-1 has higher surface area compared to the parent nanoparticles.

## 6. Applications

This section contains two parts – (1) Adsorption of congo red and (2) Photodegradation of Rhodamine-B using $SnO_2$/CdS nanocomposites.

### 6.1 Adsorption of congo red

#### 6.1.1 Introduction

Congo red is an anionic and azo dye. The color of congo red in solid powder form is red-brown and it changes in the solution depending on pH of the solution. Congo red solution having pH up to 3 gives bluish color and above 5, it gives bright red color and is used as an acid-base indicator [65]. It is used in textile industry for dying silk and cotton clothes.

IUPAC name of congo red: 3,3′-([1-1′- biphenyl]-4,4′-diyl)bis(4-aminonanpthalene-1-sulphonic acid)

Molecular formula: $C_{32}H_{22}N_6Na_2O_6S_2$

Molecular mass: 696.66 g/mol

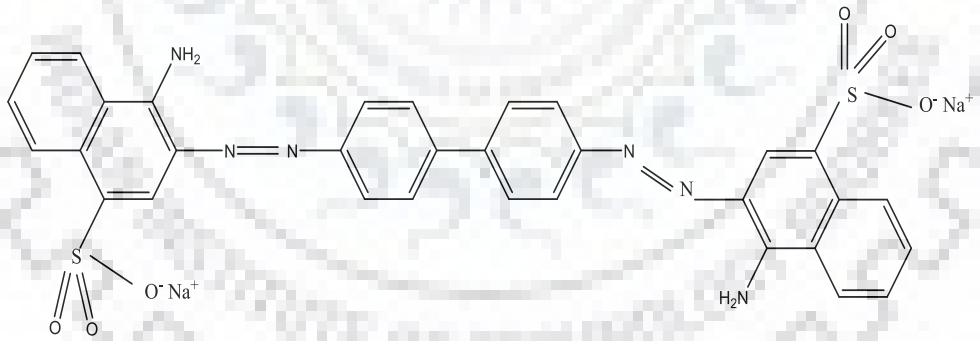


**Fig 6.1 Chemical structure of Congo red dye [66]**

Congo red is very stable and has high resistance to biodegradability. In the human body, it converts into benzidine and it is very hazardous to human health [67]. The UV-Visible spectrum

of congo red is shown in Figure 6.2. It shows absorption bands at 395 nm and 498 nm due to the azo group and naphthalene ring, respectively.

Being very dangerous to the environment and human life, it is really important to remove the dyes. In the present work, the $SnO_2$/CdS nanocomposites synthesized through thermal decomposition method show high adsorption of congo red on their surface.

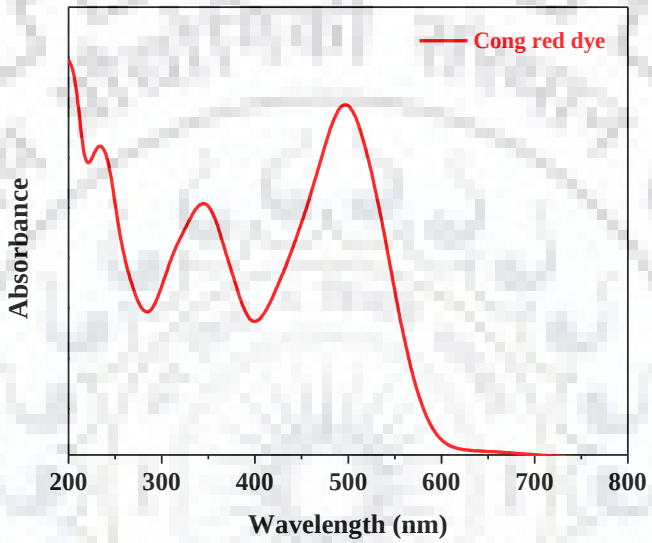


**Fig 6.2: UV-visible spectrum of congo red (concentration = $5\times10^{-5}$ M)**

### 6.1.2 Experimental details

A dye solution of $5\times10^{-5}$ M concentration was prepared by dissolving 3.48 mg of congo red in 100 ml of water. 3.5 mg of pure $SnO_2$, CdS nanoparticles and the nanocomposites were dispersed in 5 ml of dye solution by sonicating them for 3 minutes and then they were kept in dark for 90 minutes. Finally, the solution was centrifuged and the concentration of the supernatant was analyzed by UV-visible spectroscopy.

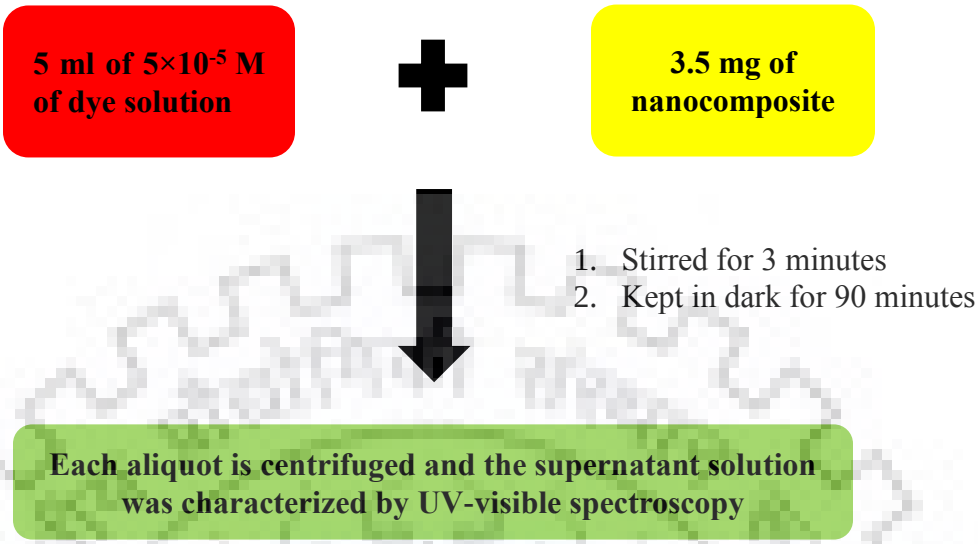


**Fig 6.3: Experimental details for the adsorption of Congo red**

### 6.1.3 Results and discussion

Figure 6.4 shows the adsorption of congo red on pure $SnO_2$, CdS nanoparticles and $SnO_2$/CdS nanocomposites (SC-1, SC-2 and SC-3) and Figure 6.5 shows the adsorption of congo red on the pure $SnO_2$, CdS and $SnO_2$/CdS nanocomposites (SCC-1, SCC-2 and SCC-3). Table 6.1 gives adsorption percentage of congo red on various adsorbents.

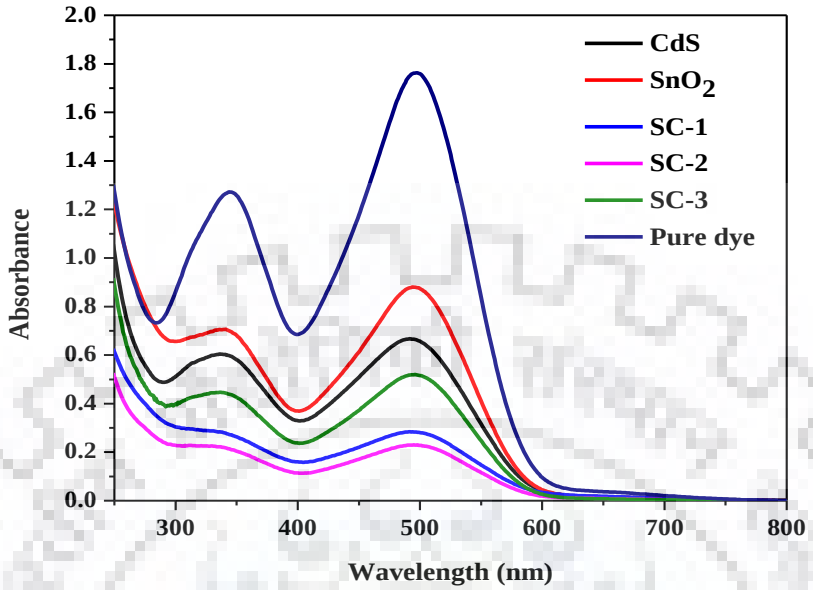


**Fig 6.4: UV-Visible spectra indicating the adsorption of congo red in aqueous solutions using $SnO_2$/CdS nanocomposites synthesized through multiple precursors as adsorbents**

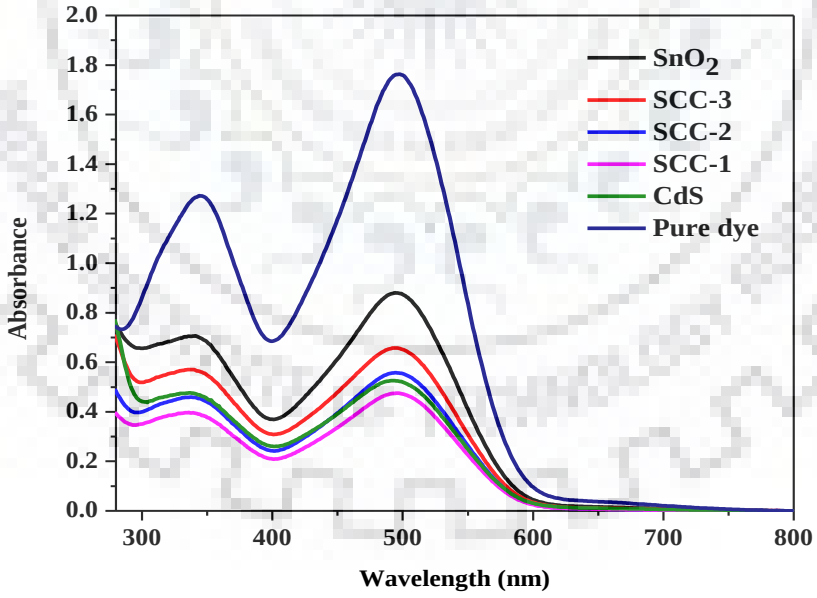


**Fig 6.5: UV-Visible spectra indicating the adsorption of congo red in aqueous solutions using $SnO_2$/CdS nanocomposites synthesized through single molecular precursor as adsorbents**

.**Table 6.1** Results on adsorption of congo red in aqueous solution using various adsorbents

| Sample ID | Absorbance | % Adsorbed | Sample ID | Absorbance | % Adsorbed |
|---|---|---|---|---|---|
| $SnO_2$ | 0.88 | 50.3 | $SnO_2$ | 0.88 | 50.3 |
| CdS | 0.53 | 70.1 | CdS | 0.53 | 70.1 |
| SC-1 | 0.28 | 84.2 | SCC-1 | 0.48 | 72.9 |
| SC-2 | 0.23 | 87.0 | SCC-2 | 0.56 | 68.4 |
| SC-3 | 0.52 | 70.6 | SCC-3 | 0.65 | 63.3 |

In the case of adsorption of congo red, nanocomposites synthesized through multiple precursors (SC-1 and SC-2) are performing better than those synthesized by using single molecular precursor because they have high surface area, besides that their surface has positive charge (zeta potential values of SC-1 and SC-2 are +4.99 mV and +4.05 mV, respectively). Congo red is an anionic dye and it gets easily attracted towards a positively charged surface due to electrostatic force of attraction. Hence, high surface area and positively charged surface are the two major reasons for the better performance of $SnO_2$/CdS nanocomposites synthesized by using multiple precursors (SC-2 and SC-1).

### 6.1.4 Recyclability

Figures 6.6 and 6.7 show recyclability of nanocomposite SC-2 towards the adsorption of congo red. The nanocomposite SC-2 after the first cycle was again used for the adsorption of congo red in the same condition after being washed with water four times and two times with methanol. In the first cycle, it shows an adsorption efficiency of 86 % and in the third cycle it decreases to 60.2 %. It is clearly evident that the nanocomposite SC-2 is good for the adsorption of the dye for up to three cycles.

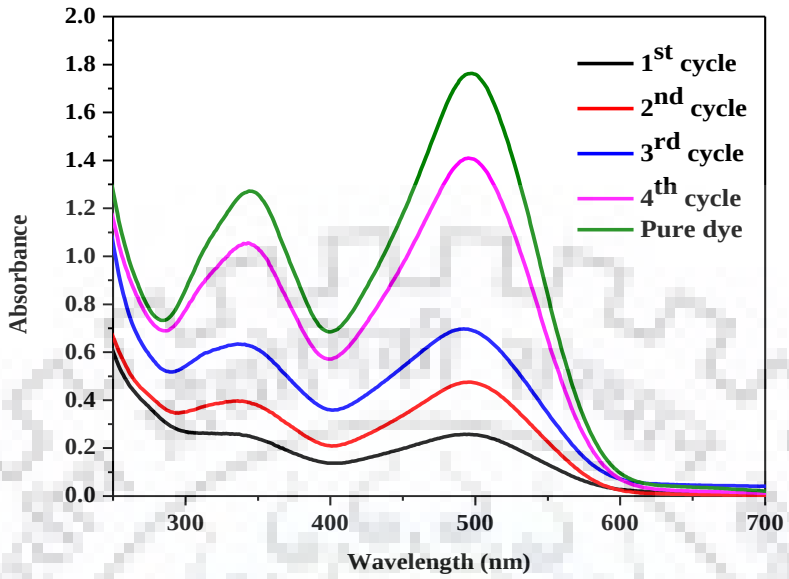


**Fig 6.6: UV-Visible spectra indicating recycling of nanocomposite SC-2 towards the adsorption of congo red in aqueous solution**

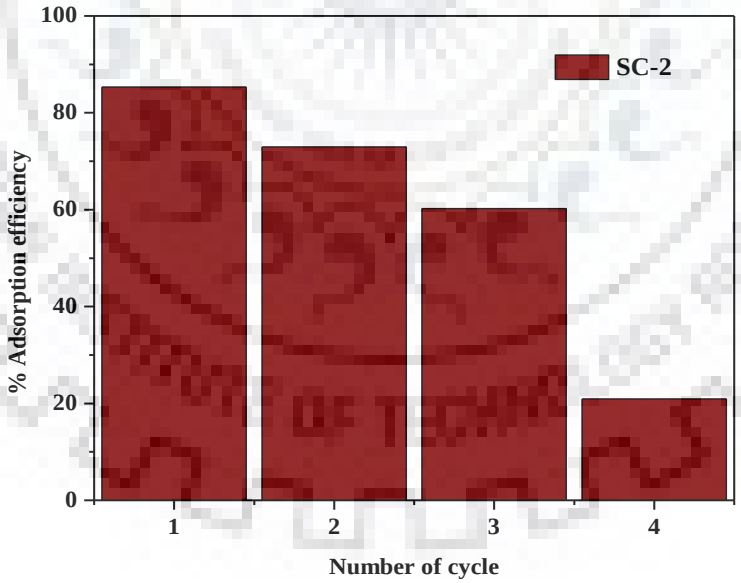


**Fig 6.7: Percentage adsorption efficiency of congo red for up to four cycles**

## 6.2 Photocatalytic degradation of Rhodamine-B

### 6.2.1 Introduction

Rhodamine B is a cationic dye, which is highly soluble in water and alcohol. It is widely used in cosmetics, food and textile industry. Also, it is used as a tracer in hydrology [68]. Chronically it is very toxic to humans and animals in terms of reproduction and development also it causes cancer [69]. It is a very toxic water pollutant and hence it needs to be removed.

IUPAC name of rhodamine B: [9-(2-carboxyphenyl)-6-(diethylamino)xanthen-3-ylidene]-diethylazanium;chloride

Molecular formula: $C_{28}H_{31}ClN_2O_3$

Molecular mass: 479.017 g/mol

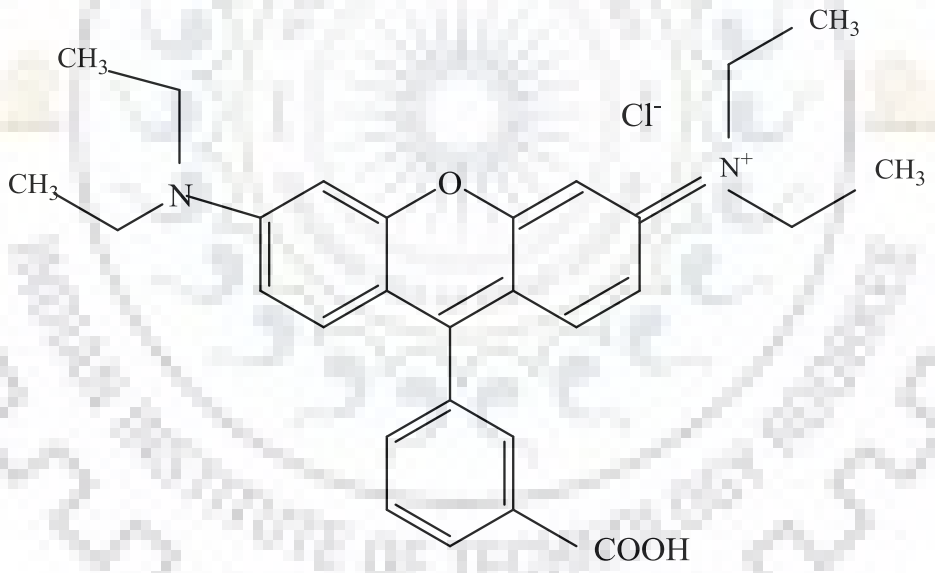


**Fig 6.8: Chemical structure of Rhodamine B [70]**

### 6.2.2 Experimental details

The photocatalytic activity of calcined pure $SnO_2$, CdS nanoparticles and $SnO_2$/CdS nanocomposites was investigated using Rhodamine B dye of $2\times10^{-5}$ M concentration in the

presence of sunlight. First, a $2\times10^{-5}$ M Rh-B aqueous solution was prepared from rhodamine B (98%, Sigma Aldrich) dye using water. 2 mg of each samples was dispersed in 6 mL of rhodamine B solution. The mixture was sonicated for 3 minutes and then kept in dark for 30 minutes in order to reach adsorption-desorption equilibrium. The mixtures were irradiated in sunlight for 50 minutes. After the irradiation, each aliquots was centrifuged at 9000 rpm for 5 min to separate the catalyst. The absorbance of dye was analyzed using UV-Vis spectrometer.

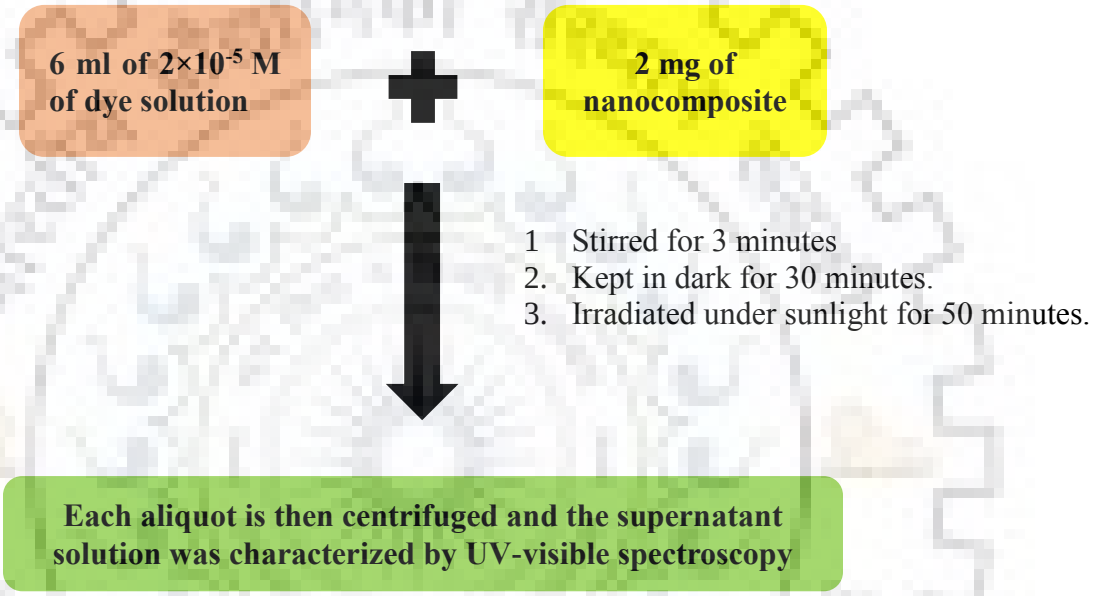


**Fig 6.9: Experimental details for the photocatalytic degradation of Rhodamine B**

### 6.2.3 Results and Discussion

Figure 6.10 shows the photodegradation of rhodamine B dye by the $SnO_2$/CdS nanocomposites, pure $SnO_2$ and CdS nanoparticles. It is clear from the UV-visible spectra that the nanocomposites (SCC-1 and SCC-2) synthesized using single molecular precursors, perform better than the pure CdS and $SnO_2$. Pure $SnO_2$ shows very negligible effect, but on combining with small amount of CdS it works better than pure CdS nanoparticles. CdS nanoparticles with a narrow band gap acts as a sensitizer and hence makes the $SnO_2$/CdS nanocomposites active in

the visible region. The life time of the charge carriers increases as the electrons from the conduction band of the CdS goes to the conduction band of $SnO_2$, having wide band gap [71].

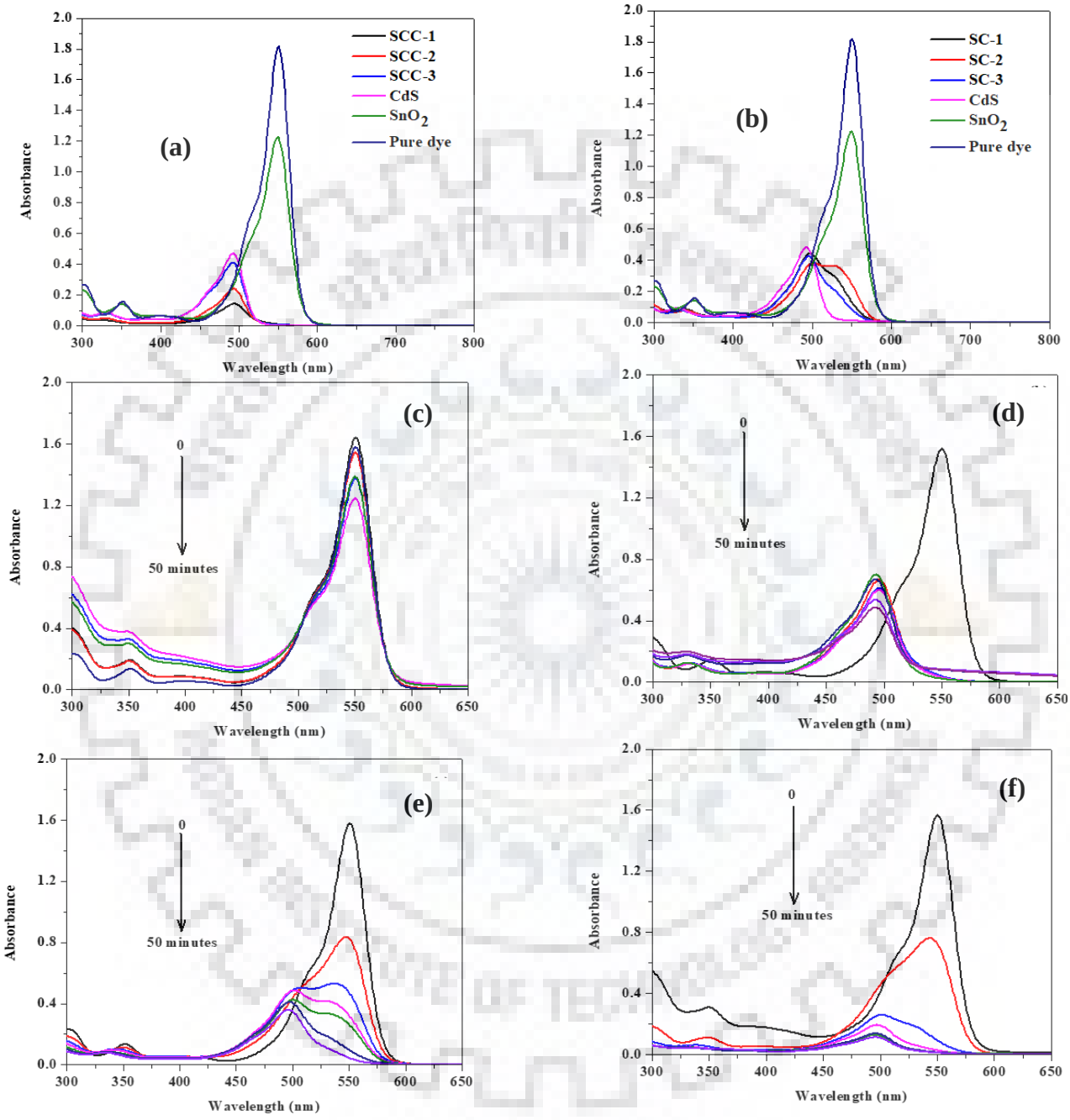


**Fig 6.10: UV- visible spectra indicating (a) & (b) photodegradation of rhodamine B in aqueous solution using pure $SnO_2$, CdS NPs and $SnO_2$/CdS nanocomposites, (c) kinetics data of $SnO_2$ (d) kinetics data of CdS, (e) kinetics data of SC-2, and (f) kinetics data of SCC-2**

**Table 6.2:** Percentage degradation of rhodamine B by pure $SnO_2$, CdS nanoparticles and $SnO_2$/CdS nanocomposites

| Sample ID | Absorbance | % degradation | Sample ID | Absorbance | % degradation |
|---|---|---|---|---|---|
| $SnO_2$ | 1.22 | 32.6 | $SnO_2$ | 1.22 | 32.6 |
| CdS | 0.48 | 73.5 | CdS | 0.47 | 74.0 |
| SC-1 | 0.45 | 75.1 | SCC-1 | 0.15 | 91.7 |
| SC-2 | 0.38 | 79.0 | SCC-2 | 0.24 | 86.7 |
| SC-3 | 0.43 | 76.2 | SCC-3 | 0.41 | 77.3 |

Nanocomposites synthesized using single molecular precursor is performing better than the one synthesized by multiple precursors. Nanocomposites SC-1, SC-2 and SC-3 have positively charged surface while the nanocomposites SCC-1 and SCC-2 have negatively charged surface (zeta potential values are -6.5 mV and -3.2 mV, respectively). Rhodamine B is a cationic dye and more molecules are attracted towards the surface of SCC-1 and SCC-2 due to electrostatic force of attraction and hence the dye is degraded effectively.

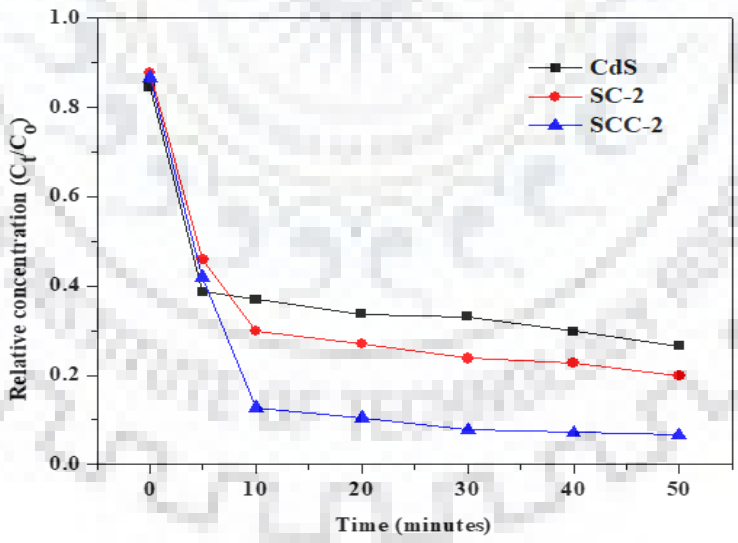


**Fig 6.11: Comparison between the nanocomposites SCC-2, SC-2 and pure CdS nanoparticles towards the photodegradation of rhodamine B in aqueous solution**

**Mechanism**

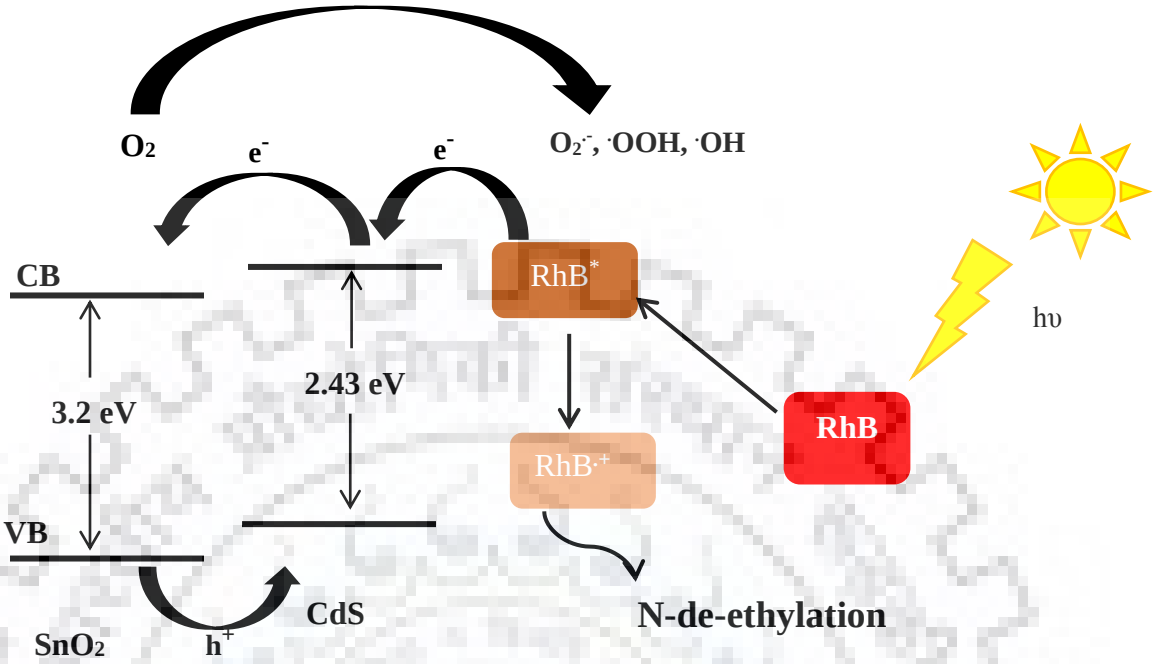


**Fig 6.12: Mechanism of photocatalytic degradation of rhodamine B using $SnO_2$/CdS nanocomposites [45, 74]**

It was observed that Rhodamine B degrades in the presence of $SnO_2$/CdS nanocomposites on irradiation with sunlight. The degradation takes place due to *N*-de-ethylation and dissociation of the azo group present in the dye. Electron present in the valence band of CdS gets excited and reaches its conduction band when irradiated with sunlight. Electrons from excited singlet state of rhodamine B reach conduction band of CdS nanoparticles leading to the formation of radical cation of rhodamine B. The de-ethylation takes place due to formation of the dye radical cation [72]. Active oxygen species like $O_2^{\cdot-}$, $OOH^{\cdot}$ and $OH^{\cdot}$ attack on one of the N-ethyl groups of the dye radical cation formed which leads to successive de-ethylation of the dye [73]. The absorption peak of *N*,*N*,*N*′,*N*′-tetra ethylated rhodamine (RhB) at $\lambda_{max}$=550 nm shifts to the blue region first when it is de-ethylated to form *N*,*N*,*N*′-tri-ethylated rhodamine (Figure 6.10). It gives absorption peak at 538 nm. The peak is further shifted to blue region when *N*,*N*′-di-ethylated rhodamine forms. Finally, rhodamine is formed having peak at 496 nm [72, 74]. Further illumination with visible light of the de-ethylated rhodamine for longer time leads to the destruction of

chromophore present in de-ethylated rhodamine. The destruction of chromophore is characterized by decrease in the intensity of peak at 496 nm.

## 7. CONCLUSIONS

$SnO_2$/CdS nanocomposites were synthesized using multiple precursors and single molecular precursor by thermal decomposition method. The nanocomposites synthesized were used for the adsorption of congo red and photodegradation of rhodamine B.

### 7.1 $SnO_2$/CdS nanocomposites synthesized using multiple precursors

Nanocomposites were synthesized by keeping the amount of $SnO_2$ nanoparticles fixed at 100 mg and changing the concentration of CdS precursors (cadmium acetate and thiourea) at three different concentrations (0.25:0.25 mmol, 0.5:0.5 mmol and 1:1 mmol). The XRD patterns confirm the formation of $SnO_2$/CdS nanocomposites and the crystallite size of $SnO_2$ is in the range of 11.2 nm to 11.6 nm. FT-IR spectra also confirm the presence of $SnO_2$ and CdS in the nanocomposites, giving IR bands due to Sn-O and Cd-S. Thermogravimetric results show that all the weight changes in the nanocomposites are mainly due to CdS present in the nanocomposites as $SnO_2$ is very stable in this temperature regime. SEM images show that the nanocomposites consist of very small particles and have no specific morphology. EDX analysis confirms the presence of tin, cadmium, sulphur and oxygen in the nanocomposites. TEM analysis shows that the particle size varies with concentration of CdS from 12.5 ± 3.1 nm to 10.7 ± 2.9 nm. SAED patterns confirm the formation of polycrystalline nanocomposites. Surface area of the nanocomposites varies from 90.8 $m^2$/g to 61.5 $m_2$/g. Tauc plots obtained from the DRS data show two band gaps in the nanocomposites due to the presence of $SnO_2$ and CdS. The band gap of $SnO_2$ changes from 3.9 eV in pure phase to 3.5 eV in the nanocomposites due to increase in the crystallite size.

### 7.2 $SnO_2$/CdS nanocomposites synthesized using single molecular precursor

Bis(thiourea) cadmium acetate is a single source for both cadmium and sulphur and was used for the synthesis of $SnO_2$/CdS nanocomposites at three different concentrations (0.25 mmol, 0.5 mmol and 1.0 mmol). XRD patterns confirm the formation of nanocomposites and the crystallite size of $SnO_2$ is in the range of 11.0 nm to 12.0 nm and the crystallite size of CdS is in the range of 11.9 nm to 12.8 nm. FT-IR spectra confirm the presence of $SnO_2$ and CdS in the nanocomposites, giving IR bands due to Sn-O and Cd-S. Thermogravimetric analysis shows that all the weight changes in the nanocomposites are due to CdS present in the nanocomposite. SEM images show that the nanocomposites formed are very small and have no specific morphology. EDX analysis

confirms the presence of tin, cadmium, sulphur and oxygen in the nanocomposites. TEM analysis shows that the particles present in the nanocomposites are in the range of 10.5 ± 3.1 nm to 11.3 ± 2.1 nm. SAED patterns confirm the formation of polycrystalline nanocomposites. Surface area values of the nanocomposites are 81.4 $m^2/g$, 58.1 $m^2/g$ and 61.7 $m^2/g$, respectively. Tauc plots show two band gaps in the nanocomposites due to the presence of $SnO_2$ and CdS. $SnO_2$ shows different band gap in the nanocomposites as compared to the pure phase; it changes from 3.9 eV to 3.2 eV in the nanocomposites.

### 7.3 Comparison between the nanocomposites synthesized using multiple precursors and single molecular precursor

Nanocomposites synthesized using multiple precursor (SC) and the other synthesized by using single precursor (SCC) are compared in the table given below.

| Characterization Technique | Comment |
|---|---|
| Powder-XRD | In the nanocomposites (SC-1, SC-2 and SC-3) crystallite size values of $SnO_2$ are 11.3 nm, 11.4 nm and 11.6 nm and that of CdS are 7.1 nm, 8.3 nm and 8.1 nm, respectively.<br>In the nanocomposites (SCC-1, SCC-2 and SCC-3) the crystallite size values of $SnO_2$ are 12.0 nm, 11.3 nm and 11.0 nm and that of CdS are 11.9 nm, 12.2 nm and 12.8 nm, respectively. |
| EDXA | In both the cases, nanocomposites synthesized at lower concentration of precursors (SC-1 and SCC-1) are non-uniform in terms of elemental distribution. The nanocomposites synthesized at higher concentration of precursors (SC-2, SC-3, SCC-2 and SCC-3) are uniform in terms of elemental distribution. |

| | |
|---|---|
| TEM | Size of the particles present in the nanocomposites synthesized through multiple precursors are relatively larger than the nanocomposites synthesized using single molecular precursor. Particle size estimated for SC-1, SC-2 and SC-3 are 12.5 ± 3.1 nm, 12.1 ± 2.9 nm and 10.7 ± 2.9 nm, respectively. Particle size of the nanocomposites SCC-1, SCC-2 and SCC-3 are 10.8 ± 2.5 nm, 11.3 ± 2.1 nm and 10.5 ± 3.1 nm, respectively. |
| SAED | Nanocomposites synthesized using multiple precursors (SC) show high degree of crystallinity as compared to the nanocomposites synthesized through single molecular precursor (SCC). |
| DRS | Band gap of $SnO_2$ in the nanocomposites SC is 3.5 eV while in SCC nanocomposites, the band gap of $SnO_2$ is 3.2 eV. |
| BET-Surface area analysis | Surface area of nanocomposites synthesized through multiple precursors are greater than that of nanocomposites synthesize through single molecular precursor. |

## 7.4 Applications

### 7.4.1 Adsorption of congo red

Nanocomposites synthesized by both the methods were explored as adsorbent for the adsorption of congo red in aqueous solutions. The nanocomposites synthesized through multiple precursors (SC-1, SC-2 and SC-3) have high surface area and positive charge as compared to the nanocomposites synthesized through single precursor (SCC-1, SCC-2 and SCC-3). Nanocomposites (SC-1 and SC-2) perform better than the parent nanoparticles.

### 7.4.2 Photodegradation of Rhodamine B

Nanocomposites synthesized by both the methods were explored as photocatalyst for the degradation of rhodamine B in aqueous solutions. The nanocomposites synthesized through single

molecular precursor (SCC-1 and SCC-2) are perform better than the parent nanoparticles and also the nanocomposites synthesized through multiple precursors.

### 7.5 Future Prospects

$SnO_2$/CdS nanocomposites can be used for other applications such as gas sensors, energy storage devices and as catalyst.

## 8. References


1. www.trynano.org.
2. https://www.theguardian.com/nanotechnology-world/nanotechnology is ancient history
3. Freestone, I.; Meeks, N.; Sax, M.; Higgitt, C. The lycurgus cup-A Roman nanotechnology. *Golden Bulletin* **2007**, 40, 270–277.
4. Reibold, M.; Paufler, P.; Levin, A. A.; Kochmann, W.; Patzke, N.; Meyer, D. C.: Materials - Carbon nanotubes in an ancient Damascus sabre. *Nature* **2006**, 444, 286-286.
5. Feynman, R. P.There's a plenty of room at the bottom, an invitation to enter new field of Physics. *Engineering and Science* **1960**, 23, 22-26.
6. https://nptel.ac.in/courses/103103033/module9/lecture1.pdf
7. Taniguchi N., 'On the basic concept of 'nano-technology'. In *Proceedings of the International Conference on Production Engineering, Tokyo*, Japan Society of Precision Engineering (1974).
8. Schaming, D.; Remita, H.: Nanotechnology: from the ancient time to nowadays. *Foundations of Chemistry* **2015**, 17, 187-205.
9. https://www.understandingnano.com/nanotechnology-definition.html
10. https://en.wikipedia.org/wiki/Nanoparticle
11. Amin, M.T.; Alazba, A.A.; Manzoor, U.: A review of removal of pollutants from water/wastewater using different types of nanomaterials. *Advances in Material Science and Engineering* **2014**, 56, 1-24.
12. https://nptel.ac.in/courses/115106076/Module%2010/Module%2010.pdf
13. Schmid, G.; Corain, B.: Nanoparticulated: gold syntheses, structures, electronics, and reactivities. *Eur. J. Inorg. Chem.* **2003**, 17, 3081–3098.
14. https://en.wikipedia.org/wiki/Colloidal_gold
15. Sanjay, S. S.; Pandey, A. C.: A Brief Manifestation of Nanotechnology. **2017**, *62*, 47–64.
16. Wahajuddin; Arora, S.: Superparamagnetic iron oxide nanoparticles: magnetic nanoplatforms as drug carriers. *Int. J. Nanomedicine* **2012**, *7*, 3445–3471.
17. Hasan, T.: Mechanical properties of nanomaterials. *Nanocomposite Mater.* **2016**, *2*, 1131–1138.

18. Pokropivny, V. V.; Skorokhod, V. V.: Classification of nanostructures by dimensionality and concept of surface forms engineering in nanomaterial science. *Mater. Sci. Eng. C* **2007**, *27*, 990–993.
19. Tiwari, J. N.; Tiwari, R. N.; Kim, K. S.: Zero-dimensional, one-dimensional, two-dimensional and three-dimensional nanostructured materials for advanced electrochemical energy devices. *Prog. Mater. Sci.* **2012**, *57*, 724–803.
20. Khan, I.; Saeed, K.; Khan, I.: Nanoparticles: properties, applications and toxicities. *Arab. J. Chem.* **2017**.
21. Arole, V. M.; Munde, P. S. V.: Fabrication of nanomaterials by top-down and bottom-up approaches – an overview. **2014**, *1*, 89–93.
22. Pareek, V.; Bhargava, A.; Gupta, R.; Jain, N.; Panwar, J.: Synthesis and applications of noble metal nanoparticles : A Review. **2017**, *9*, 527–544.
23. Cury, C. P. H; Gundappa S. K; Fernando W.: Nanocomposites : synthesis, structure, properties and new application opportunities. *Mater. Res.* **2009**, *12*, 1–39.
24. Moghadam, A. D.; Schultz, B. F.; Ferguson, J. B.; Omrani, E.; Rohatgi, P. K.; Gupta, N.: Functional metal matrix composites: self-lubricating, self-healing, and nanocomposites-an outlook. *Jom* **2014**, *66*, 872–881.
25. Rathod, V. T.; Kumar, J. S.; Jain, A.: Polymer and ceramic nanocomposites for aerospace applications. *Appl. Nanosci.* **2017**, *7*, 519–548.
26. Duncan, T. V.; Pillai, K.: Release of engineered nanomaterials from polymer nanocomposites: Diffusion, Dissolution, and Desorption. *ACS Appl. Mater. Interfaces* **2015**, *7*, 2–19.
27. Hernández, T. P.; Flores, G. A. H.; López, O. E. C.; Sánchez, M. E. M.; Arreola, I. V.; Vergara, E. G.; Rojas, M. A M..: Synthesis of Cu and Co metal oxide nanoparticles from thermal decomposition of tartrate complexes. *Inorganica Chim. Acta* **2012**, *392*, 277–282.
28. Nikam, A. V.; Prasad, B. L. V.; Kulkarni, A. A.: Wet chemical synthesis of metal oxide nanoparticles: A review. *CrystEngComm* **2018**, *20*, 5091–5107.
29. Agrawal, D. K.: Microwave processing of ceramics. *Curr. Opin. Solid State Mater. Sci.* **1998**, *3*, 480–485.
30. Cadena, G. J.; Riu, J.; Rius, F. X.: Gas sensors based on nanostructured materials. *RSC Adv.* **2007**, *132*, 1083-1099.

31. Pomogailo, D. A.; Singh, S.; Singh, M.; Yadav, B. C.; Tandon, P.; Pomogailo, S. I.; Dzhardimalieva, G. I.; Kydralieva, K. A.: Polymer-matrix nanocomposite gas-sensing materials. *Inorg. Mater.* **2014**, *50*, 296–305.
32. Mirzaei, A.; Janghorban, K.; Hashemi, B.; Bonavita, A.; Bonyani, M.; Leonardi, S.; Neri, G.: Synthesis, characterization and gas sensing properties of Ag@α-$Fe_2O_3$ core–shell nanocomposites. *Nanomaterials* **2015**, *5*, 737–749.
33. Lin, Q.; Li, Y.; Yang, M.: Tin oxide/Graphene composite fabricated via a hydrothermal method for gas sensors working at room temperature. *Sensors Actuators, B Chem.* **2012**, *173*, 139–147.
34. Zhan, S.; Hou, Q.; Li, Y.; Ma, S.; Wang, P.; Li, Y.; Wang, H.: AgBr/g-$C_3N_4$ nanocomposites for enhanced visible-light-driven photocatalytic inactivation of Escherichia Coli. *RSC Adv.* **2018**, *8*, 34428–34436.
35. Yadav, S. K.; Jeevanandam, P.: Synthesis of γ-$Fe_2O_3$–CdS nanocomposites with enhanced photocatalytic activity by thermal decomposition approach. *J. Nanosci. Nanotechnol.* **2016**, *16*, 9072–9084.
36. Xu, F.; Yuan, Y.; Han, H.; Wu, D.; Gao, Z.; Jiang, K.: Synthesis of ZnO/CdS hierarchical heterostructure with enhanced photocatalytic efficiency under nature sunlight. *CrystEngComm* **2012**, *14*, 3615–3622.
37. Zhao, Z. J.; Hwang, S. H.; Jeon, S.; Hwang, B.; Jung, J. Y.; Lee, J.; Park, S. H.; Jeong, J. H.: Three-dimensional plasmonic Ag/$TiO_2$ nanocomposite architectures on flexible substrates for visible-light photocatalytic activity. *Sci. Rep.* **2017**, *7*, 1–11.
38. Zhang, X.; Wang, X.; Chen, Z.: A novel nanocomposite as an efficient adsorbent for the rapid adsorption of Ni (II) from aqueous solution. *Materials (Basel).* **2017**, *10*, 1–22.
39. Bhaumik, M.; Setshedi, K.; Maity, A.; Onyango, M. S.: Removal from water using fixed bed column of polypyrrole/$Fe_3O_4$ nanocomposite. *Sep. Purif. Technol.* **2013**, *110*, 11–19.
40. Tanzifi, M.; Karimipour, K.; Najafifard, M.; Mirchenari, S.: Removal of congo red anionic dye from aqueous solution using polyaniline/$TiO_2$ and Polypyrrole/$TiO_2$ nanocomposites: Isotherm, Kinetic, and Thermodynamic Studies. *Int. J. Eng.* **2016**, *29*, 1659–1669.
41. Zhou, W.; Cheng, C.; Liu, J.; Tay, Y. Y.; Jiang, J.; Jia, X.; Zhang, J.; Gong, H.; Hng, H. H.; Yu, T.; Fan, H. J.: Epitaxial growth of branched α-$Fe_2O_3$/$SnO_2$ nano-heterostructures

with improved lithium-ion battery performance. *Advanced Functional Materials*. **2011**, 21, 2439–2445.

42. Riggs, B.C.; Adireddy, S.; Rehm, C.H.; Puli, V. S.; Elupula, R.; Chrisey, D. B.: Polymer nanocomposites for energy storage applications. *Materials Today: Proceedings* **2015**, 2, 3853-3863.
43. Hsiang, H. I.; Lin, K. Y.; Yen, F. S.; Hwang, C. Y.: Effects of particle Size of $BaTiO_3$ powder on the dielectric properties of $BaTiO_3$/Polyvinylidene fluoride composites. *J. Mater. Sci.* **2001**, *36*, 3809–3815.
44. Senasu, T.; Hemavibool, K.; Nanan, S.: Hydrothermally grown CdS nanoparticles for photodegradation of anionic azo dyes under UV-Visible light irradiation. *RSC Adv.* **2018**, *8*, 22592–22605.
45. Zhang, L.; Niua, C. G.; Liang, C.; Wen, X. J.; Huang, D. W.; Guo, H.; Zhaoa, X. F.; Zeng, G. M.: One-step in situ synthesis of $CdS/SnO_2$ heterostructure with excellent photocatalytic performance for Cr(VI) reduction and teteracycline degradation. *Chemical Engineering Journal*, **2018**, 352, 863-875.
46. Mohana Priya, S.; Geetha, A.; Ramamurthi, K.: Structural, morphological and optical properties of tin oxide nanoparticles synthesized by Sol–Gel method adding hydrochloric acid. *J. Sol-Gel Sci. Technol.* **2016**, *78*, 365–372.
47. Kar, A.; Kundu, S.; Patra, A.: Photocatalytic properties of semiconductor $SnO_2$/CdS heterostructure nanocrystals. *RSC Adv.* **2012**, *2*, 10222–10230.
48. Yan, S.; Hu, D.; Hu, F.; Wu, J.; Huang, N.; Xiao, Z.: Solution-based synthesis of $SnO_2$ nanoparticle/CdS nanowire heterostructures. *CrystEngComm* **2011**, *13*, 4580–4585.
49. Venkata Reddy, C.; Ravikumar, R. V. S. S. N.; Srinivas, G.; Shim, J.; Cho, M.: Structural, optical, and improved photocatalytic properties of $CdS/SnO_2$ hybrid photocatalyst nanostructure. *Mater. Sci. Eng. B Solid-State Mater. Adv. Technol.* **2017**, *221*, 63–72.
50. Zhao, J.; Yin, J.; Hua, Z.: Synthesis, characterization and optical properties of CdS nanowire/$SnO_2$ nanoparticle nano-heterostructures. *Mater. Lett.* **2014**, *122*, 237–239.
51. Gu, F.; Wang, S. F.; Lü, M. K.; Zhou, G. J.; Xu, D.; Yuan, D. R.: Photoluminescence properties of $SnO_2$ nanoparticles synthesized by Sol-Gel method. *J. Phys. Chem. B* **2004**, *108*, 8119–8123.

52. Rajesh, N. P.; Kannan, V.; Ashok, M.; Sivaji, K.; Santhana Raghavan, P.; Ramasamy, P.: A new nonlinear optical semi-organic material: Cadmium thiourea acetate. *J. Cryst. Growth* **2004**, *262*, 561–566.
53. https://serc.carleton.edu/research_education/geochemsheets/BraggsLaw.html
54. Alexander, L.; Klug, H. P.: Determination of crystallite size with the X-Ray Spectrometer. *J. Appl. Phys.* **1950**, *21*, 137–142.
55. Thommes, M.; Kaneko, K.; Neimark, A. V.; Olivier, J. P.; Reinoso, F. R.; Rouquerol, J.; Sing, K. S. W.: Physisorption of gases, with special reference to the evaluation of surface area and pore size. *Pure Appl. Chem.* **2015**, 87, 1051–1069.
56. Tumuluri, A.; Lakshun Naidu, K.; James Raju, K. C.: Band gap determination using Tauc's plot for $LiNbO_3$ thin films. *Int. J. ChemTech Res.* **2014**, *6*, 3353–3356.
57. Sarabadani, P.; Sadeghi, M.; Ghasemi, M.; Asadollahi, Z.; Afshari, N.: Synthesis and characterization of tin oxide nanoparticles by solid state chemical reaction method. *J. Clust. Sci.* **2011**, *22*, 131–140.
58. Susha, N.; Nandakumar, K.; Nair, S. S.: Enhanced photoconductivity in CdS/Betanin composite nanostructures. *RSC Adv.* **2018**, *8*, 11330–11337.
59. Rao, B. S.; Kumar, R. B.; Reddy, V. R.; Rao, T. S.: Preparation and characterization of CdS nanoparticles by chemical co-precipitation technique. *Chalcogenide Lett.* **2011**, *8*, 177–185.
60. Gaur, R.; Jeevanandam, P.: Synthesis and characterization of $Cd_{1-X}Zn_xS$ (X=0-1) nanoparticles by Thermal decomposition of bis(thiourea)cadmium–zinc acetate complexes. *ChemistrySelect* **2016**, *1*, 2687–2697.
61. Mohanraj, V.; Jayaprakash, R.; Robert, R.; Balavijayalakshmi, J.; Gopi, S.: Effect of particle size on optical and electrical properties in mixed CdS and NiS nanoparticles synthesis by Ultrasonic wave irradiation method. *Mater. Sci. Semicond. Process.* **2016**, *56*, 394–402.
62. Cruz, A. L.; Marquina, A. V.; Mendoza, D. B.; Mendoza, C. V.; Huerta, I. E. Z.; Delgado, L. A. G.; Juárez, A. G.; Fuentes, R. G.; Hernández, A. G. R.: Microstructural and optical characterizations of highly stable nanospheres of crystalline CdS via selective approach. *Opt. Mater. Express* **2013**, *4*, 129–141.

63. Prasana, J. C.; Anuradha, A.; Madhavan, J.; Sagayaraj, P.: Growth and characterization of Bis(thiourea) cadmium acetate single crystal: An efficient semiorganic non-linear optical single crystal. *Asian J. Chem.* **2013**, *25*, 969–971.
64. Rajesh, N. P.; Kannan, V.; Ashok, M.; Sivaji, K.; Raghavan, P. S.; Ramasamy, P.: A new nonlinear optical semi-organic material: Cadmium thiourea acetate. *J. Cryst. Growth* **2004**, *262*, 561–566.
65. Mondal, S. P.; Dhar, A.; Ray, S. K.: Optical properties of CdS nanowires prepared by Dc Electrochemical Deposition in porous alumina template. *Mater. Sci. Semicond. Process.* **2007**, *10*, 185–193.
66. https://en.m.wikipedia.org/wiki/Congo_red
67. https://pubchem.ncbi.nlm.nih.gov/compound/Congo_red
68. Paulraj, A.; Elizabeth, A. T.: Removal of rhodamine B and congo red from aqueous solutions by adsorption onto activated carbons. *Chem. Sci. Trans.* **2016**, *5*, 87–96.
69. Rochat, J.; Demenge, P.; Rerat, J. C.: Toxicologic study of a fluorescent tracer: rhodamine B. *Toxicological European Research* **1978**, 1, 23-26.
70. Richardson, S. D.; Willson, C. S.; Kelly A. R.: Use of rhodamine water tracer in the Marshland Upwelling System. *Ground Water* **2001**, *42*, 678–688.
71. Yahia, I. S.; Rammah, Y. S.; Khaled, K. F.: Fabrication of electrochemical cell based on rhodamine dye for low power applications. *Journal of Materials and Environmental Science* **2013**, 4, 442-447.
72. Liu, G.; Wang, L.; Yang, H. G.; Cheng, H. M.; Lu, G. Q.: Titania-based photocatalysts - crystal growth, doping and heterostructuring. *J. Mater. Chem.* **2010**, *20*, 831–843.
73. Watanabe, T.; Takizawa, T.; Honda, K.: Photocatalysis through excitation of adsorbates highly efficient N-deethylation of rhodamine B adsorbed to CdS. *J. Phys. Chem.* **2005**, *81*, 1845–1851.
74. Yadav, S. K.; Jeevanandam, P.: Thermal decomposition approach for the synthesis of CdS-$TiO_2$ nanocomposites and their catalytic activity towards degradation of rhodamine B and reduction of Cr (VI). *Ceram. Int.* **2015**, *41*, 2160–2179.
75. Li, W.; Li, D.; Meng, S.; Chen, W.; Fu, X.; Shao, Y.: Novel approach to enhance photosensitized degradation of rhodamine B under visible light irradiation by the $ZnxCd_{1-X}S/TiO_2$ nanocomposites. *Environ. Sci. Technol.* **2011**, *45*, 2987–2993.